6-2018

Integration of Remote Sensing and Proximal Sensing for Improvement of Field Scale Water Management

Foad Foolad
University of Nebraska-Lincoln, foadfoolad@huskers.unl.edu

INTEGRATION OF REMOTE SENSING AND PROXIMAL SENSING FOR IMPROVEMENT OF FIELD SCALE WATER MANAGEMENT

by

Foad Foolad

A DISSERTATION

Presented to the Faculty of

The Graduate College at the University of Nebraska

In Partial Fulfillment of Requirements

For the Degree of Doctor of Philosophy

Major: Civil Engineering

(Water Resources)

Under the Supervision of Professor Trenton E. Franz and Professor Ayse Kilic

Lincoln, Nebraska

June, 2018

INTEGRATION OF REMOTE SENSING AND PROXIMAL SENSING FOR IMPROVEMENT OF FIELD SCALE WATER MANAGEMENT

Foad Foolad, Ph.D.

University of Nebraska, 2018

Advisor: Trenton E. Franz

Water is one of the most precious natural resources, and sustainable water resources development is a significant challenge facing water managers over the coming decades. Accurate estimation of the different components of the hydrologic cycle is key for water managers and planners in order to achieve sustainable water resources development. The primary goal of this dissertation was to investigate techniques to combine datasets acquired by remote and proximal sensing and in-situ sensors for the improvement of monitoring near surface water fluxes. This dissertation is separated into three site-specific case studies. First study, investigated the feasibility of using inverse vadose zone modeling for field actual evapotranspiration (ET_a) estimation. Results show reasonable estimates of ET_a, both daily and annually, from soil water content (SWC) sensors and Cosmic-Ray Neutron Probes (CRNPs). Second study, combined remote and proximal sensing methods to explore the spatial correlation between hydrological state variables and ET flux. Comparison of the datasets reveal that SWC and ET_a were linearly correlated but the correlation between depth to the water table and ET_a was weak. A simple multivariate linear regression model was used to estimate ET_a. The estimated ET_a values were then compared to the time ET_a integration spline method. The comparison indicates similar

seasonal ET_a between the two methods in 2015 (wet) but a 20% reduction in 2016 (dry). The study highlights the challenge of connecting hydrologic state variables with hydrologic flux estimates. Third study, evaluated the functionality of automatically calibrated Earth Engine Evapotranspiration Flux (EEFlux) to the existing mapping evapotranspiration at high resolution with internalized calibration (METRIC) images in different locations. The comparison results showed that EEFlux is able to calculate Reference evapotranspiration Fraction (ET_rF) and ET_a in agricultural areas comparable (RMSE=0.13) to the ones from trained expert METRIC users. However, the EEFlux algorithm needs to be improved to calculate ET_rF and ET_a in non-agricultural areas (RMSE=0.21). Given the paucity of in-situ data across much of the globe the field of remote sensing offers an alternative but requires users to be cautious and realistic about associated errors and uncertainty on using such information to help construct a hydrologic budget.

DEDICATION

To

my father, Captain Hojatollah Foolad, my forever-hero

who was a wonderful father, a great husband, and a genuinely kind person, who sacrificed his life

for his people and his country in an airplane crash in February 18th, 2018

and,

my mother, Susan Akbari, my angel on earth

who has been always there to support me through difficulties

ACKNOWLEDGEMENTS

I wish I could write this when my dad was here with us but unfortunately, sometimes life does not go as planned. However, my dear dad always knew how grateful I was and my dear mom knows I am always thankful for their numerous sacrifices throughout my life, especially as I completed my Ph.D. as I would have never made it here without their supports.

Despite the stressful situation, I decided to finish my Ph.D., as I knew, that makes my parents happy and proud. I sincerely appreciate their unconditional and never-ending love, their emotional and financial support and everything they have done for me. I hope finishing my Ph.D. atones for some of the suffering they had to go through. In addition, I appreciate my sibling's supports. I am aware of the pain Samira and Hosein had to go through in my absence as I was not able to be with them in times of hardship and they had to carry all the responsibilities on their shoulders. I hope one day I can return their kindness.

I also would like to express my sincere thanks and gratitude to my advisors: Prof. Trenton E. Franz and Prof. Ayse Kilic for their patient guidance, invaluable discussions, endless feedback, time and constant support during my time at the University of Nebraska-Lincoln (UNL). Furthermore, it was my honor to meet Prof. Richard Allen and have the chance to have his precious advices during my studies at UNL. In addition, I truly appreciate the valuable input and comments made by my committee members: Prof. Shannon Bartelt-Hunt, Prof. Yusong Li and Prof. Dr. Andrew E. Suyker, without whom my efforts would not have been complete and fruitful.

My deep appreciation to Prof. Daniel Linzell, Prof. John Stansbury, Prof. Bruce Dvorak, Prof. John Carroll, and Prof. Junke Guo for their supports throughout my study at UNL, without their help and supports I would not have been able to finish my degree.

Special thanks go to my wonderful friends, Prof. Majid Nabavi and Parisima Sarlak, who have always been there to support the Iranian students and have supported me in the past 6 years, specifically after the tragedy that I had to deal with. My gratitude to my wonderful friends, my chosen siblings: Mohsen, Azar, Babak, Saeedeh, Ehsan, Delaram, and many other friends who have supported me consistently, have had my back and did not let me fall down, who helped me to stand up again after the tragedy, who proved to me that we do not need to be from the same parents to be siblings; as long as we are connected mentally and have each other's back, we are like brothers and sisters, even sometimes closer.

Moreover, I would like to express my deepest appreciation to my office-mates for their help, their comments and for the data they provided me.

Studying at UNL was a life-changing opportunity. I met wonderful people here at UNL who showed me how I can be a better human being and who taught me that the color of our skin, our nationality, our background, our religion, and our beliefs do not matter at all. I deeply appreciate what they have taught me and I hope I can be a good student and become a better person.

TABLE OF CONTENTS

LIST OF TABLES

LIST OF FIGURES

LIST OF SYMBOLS

Latin Symbols

AGDD	= Accumulated Growing Degree Days (^{0}C),
CDF	= Cumulative Distribution Function
D	= Plant Root Depth (cm)
DTWT	= Depth to the Water Table
EF	= Evaporative Fraction (-)
E_p	= Potential Evaporation (mm/day)
ET	= Evapotranspiration (mm/day)
ET_a	= Actual Evapotranspiration (mm/day)
ET_{inst}	= Instantaneous ET (mm/hr)
ET_p	= Potential Evapotranspiration (-)
ET_r	= Reference Evapotranspiration (mm/day)
ET_rF	= Reference ET Fraction (-)
G	= Ground Heat Flux (W/m^2)
GDD	= Growing Degree Days (^{0}C),
H	= Pressure Head (m)
H	= Sensible Heat Flux (W/m^2)
k	= Extinction Coefficient (-)
K	= Unsaturated Hydraulic Conductivity (cm/day)
Kc	= Crop-Specific Coefficient (-)

K_s	= Saturated Hydraulic Conductivity (cm/day)
LAI	= Leaf Area Index (cm^2/cm^2)
LE	= Latent Heat Energy (W/m^2)
n	= Pore Size Distribution of a Soil (-)
O_i	= Observed Value
$\overline{O}_i$	= Observed Mean Value
P	= Precipitation (mm)
P_i	= Simulated Value
R_n	= Net Radiation (W/m^2)
S_e	= Saturation Degree (-)
S(h)	= Root Water Uptake (mm/day)
S_p	= Potential Water Uptake Rate (mm/day)
SWC	= Soil Water Content (cm^3/cm^3)
T	= Time (Day)
T_{base}	= Base Temperature (^oC)
T_{min}	= Minimum Daily Temperature (^oC)
T_{max}	= Maximum Daily Temperature (^oC)
T_p	= Potential Transpiration (mm/day)
T_s	= Surface Temperature (K)

Greek Symbols

α	= Inversely Related to Air Entry Pressure (1/cm)
$\alpha(h)$	= Root-Water Uptake Water Stress Response Function (-)
λ	= Latent Heat of Vaporization (J/kg)
θ	= Volumetric Soil Water Content (cm^3/cm^3)
θ_r	= Residual Soil Water Content (cm^3/cm^3)
θ_s	= Saturated Soil Water Content (cm^3/cm^3)

LIST OF ACRONYMS

CFSR = Climate Forecast System Reanalysis

CRNP = Cosmic-Ray Neutron Probes

EC = Eddy-Covariance

EEFlux = Earth Engine Evapotranspiration Flux

GRACE = Gravity Recovery and Climate Experiment

HPRCC = High Plains Regional Climate Center

Landsat = Land Remote Sensing Satellite

LSM = Land Surface Models

MAE = Mean Average Error

METRIC = Mapping Evapotranspiration at High Resolution with Internalized Calibration

MODIS = Moderate Resolution Imaging Spectroradiometer

NDVI = Normalized Difference Vegetation Index

NLDAS = North American Land Data Assimilation System

NSE = Nash-Sutcliffe Efficiency

R^2 = Coefficient of Determination

RMSE = Root Mean Square Error

SEBAL = Surface Energy Balance Algorithms for Land

SK = Simple Kriging

SMOS = Soil Moisture and Ocean Salinity

TP = Theta Probes

VZM	= Vadose Zone Model

CHAPTER 1: INTRODUCTION

1.1 Motivation and Research Objectives

With global population increase, the global food demand will increase for at least another 40 years (Godfray et al. 2010). Much of that global population growth is expected to be in regions which are already struggling to feed their population (Porkka et al. 2016). Many of these regions are located in arid and semi-arid areas of the world and considering the limited available water resources in these areas water scarcity will be a growing and challenging problem to solve. As a consequence of increasing water scarcity and drought, further exacerbated by climate change, intense competition between the agricultural sector and other economical sectors is expected (Mancosu et al. 2015). However, rapid technological developments in proximal sensing, remote sensing, and in-situ sensors provide scientists and water planners hope by providing more resolved datasets in time and space. While remote sensing collects the data from a platform operating on satellites or aircraft, proximal sensing collects the information from a ground-based platform which is usually located near the object of interest (Price 1986). These improved observations will be helpful for more precise water resource planning in order to meet agricultural needs and avoid excessive water consumption. It is well recognized that: “one cannot effectively manage that which one does not monitor”.

During past few years, proximal sensing has widely been used for collecting detailed information about water flux and soil state near the surface (Binley et al. 2015). A few examples of proximal sensing key to this dissertation are Bowen ratio tower (Tanner

1960; Blad and Rosenberg 1974; Massman 1992; Zhang et al. 2008; Irmak 2010), eddy-covariance tower (Swinbank 1951; Tanner 1960; Kizer and Elliott 1991; Anthoni, Law, and Unsworth 1999; Wilson et al. 2001; Sun et al. 2008) and Cosmic-Ray Neutron Probes (CRNP) (Zreda et al. 2008, 2012; Franz et al. 2012; Dong et al. 2014; Desilets and Zreda 2013) which measure different fluxes and hydrological state variables from the land surfaces and its surrounding areas. In addition, many governmental and federal agencies use remotely sensed data (e.g., MODIS, Landsat, Sentinel, GRACE, and SMOS etc.) for their studies and analysis. Satellites orbit the earth and provide independent datasets which cover the range of hydrological cycle components (McCabe et al. 2017). Finally, in-situ sensors like water level, temperature, flow velocity, soil moisture etc. are often used to collect observations at a point in a field in order to more efficiently manage water consumption. A fundamental and remaining challenge is how to combine remote, proximal and in-situ sensors to better understand water flux and soil state at the same spatial and temporal scale.

From land surfaces, evapotranspiration (ET) constitutes about 2/3 of the total annual partitioning of available precipitation, making it the largest flux of water. Understanding ET is vital for regional and global estimates of water balance. Uncertainty in ET estimation can cause imprecise water balance prediction (Anayah and Kaluarachchi 2014). Real-time field scale ET measurement is important as it has huge consequences on water management in agriculture. For instance, in the state of Nebraska over 90% of water is used for agriculture but field scale ET measurement is challenging and costly; therefore, the measurements are limited to scientific studies. As the measurements of the hydrological state variables are much easier and less expensive than field scale ET measurement, this research aimed to explore statistical and physically based models driven by these state variables to estimate actual ET (ET_a) flux. In this study, different techniques were used to estimate ET_a at the field scale. In addition, key hydrological state variables (e.g., soil water content and groundwater) were used to explore the relationship between ET_a and the state variable(s). Here we combined a novel set of data from proximal and remote sensing data with in-situ sensors to investigate spatiotemporal changes in ET_a and what factors controlled it.

For example, by using Landsat images and applying mapping evapotranspiration at high resolution with internalized calibration (METRIC) model ET_a was estimated in different part of the Nebraska. METRIC is a satellite-based image-processing model consisting of multiple sub models. The method generates an accurate and highly resolved ET_a estimation map in space (~30 m) as the residual of the surface energy balance equation by using satellite imagery (Allen et al., 2007b, 2007a). In another part of this research, the automated calibrated Earth Engine Evapotranspiration Flux (EEFlux) ET_a was compared to manually calibrated METRIC ET_a in different parts of the U.S. While EEFlux is designed based on the METRIC model, it applies the automated calibration algorithms for the computations (Allen et al. 2015) and uses the imagery archives of Google Earth Engine, (see Gorelick et al. 2017). Where METRIC takes more effort and expertise to process the imagery, EEFLUX is freely available across the globe.

In addition, point scale and the area-average soil water content (SWC) data were used to estimate ET_a at a field in eastern Nebraska using a physically based model

(HYDRUS). The ET_a was then compared to the independently measured ET_a by an eddy-covariance tower of the same field. The point scale SWC data were measured by in-situ sensors, theta probes (TP), and the area-average SWC data were recorded by newly-developed CRNPs (Zreda et al. 2008) and later (Zreda et al. 2012). CRNPs provide highly resolved temporal data sets of area-average soil moisture measurement over a large horizontal footprint (tens of hectometers) and a depth of tens of centimeters. The CRNPs spatial and temporal resolution makes it desirable for combining with remotely sensed products. CRNPs do not need to be inserted into the soil, while point sensors need to be in a direct soil contact which is often logistically challenging due to factors such as routine management practices. This challenge makes point sensor network installation and maintenance costly and time consuming to upkeep in agriculturally systems (Franz et al. 2016).

1.2 Dissertation Outline

The previous section presented an overview of the general objectives of this dissertation. This section outlines the specific research questions and findings of the remaining chapters.

In Chapter 2, the feasibility of using inverse vadose zone modeling was investigated for field ET_a estimation at a long-term agricultural monitoring site in eastern Nebraska. Data from both point based SWC sensors and CRNPs were used to estimate ET_a at the study site and then the estimated ET_a values compared to the ET_a measured by Eddy-Covariance tower located at the site. The key results indicated:

- Reasonable estimates of ET_a, both daily and annually, from point sensors and CRNP.
- Due to soil texture variability at the study site, soil hydraulic function parameterizations were highly variable. This leads to equally good ET_a modelled estimates which is consistent with the hydrological principle of equifinality.
- While the focus of this study was on a particular study site in Nebraska, the tested framework can be easily applied to other SWC monitoring networks across the globe for ET_a estimation.

In Chapter 3, remote and proximal sensing measurements were combined with monitoring wells at a study site in central Nebraska to explore the spatial relationship between ET_a and near surface SWC and depth to the water table (DTWT). A series of statistical models were explored between the state variables and flux estimates at the same spatial scale. This as a novel use of CRNP data, point scale data, and satellite imagery since it is challenging to combine data across spatial scales and sensor types. METRIC was applied on Landsat-8 images to estimate ET_a. Data from stationary and roving CRNPs were used to estimate SWC. DTWT was estimated from a network of 16 observation groundwater wells. Results showed that:

- While SWC and ET_a were linearly correlated for shallow-rooted vegetation, the correlation between DTWT and ET_a was weak.
- A simple multivariate linear regression model between daily SWC, weather station reference evapotranspiration (ET_r), and Landsat Normalized

Difference Vegetation Index (NDVI) was used to estimate daily growing season ET_a for 2015 and 2016 averaged over the study area. The estimated ET_a values were then compared to the time ET_a integration spline method. The comparison indicates similar seasonal ET_a between two methods in 2015 (wet) but a 20% reduction in 2016 (dry).

In Chapter 4, different EEFlux products were compared to the METRIC ones in agricultural and non-agricultural areas. Although EEFlux is designed based on METRIC algorithms, there are still some minor differences between them. The full functionality and reliability of the automated EEFlux platform needed to be tested. In this research, 58 processed METRIC images in different parts of the U.S. were used to evaluate EEFlux. Based on the comparisons:

- Three intermediate products, surface temperature (T_s) Albedo, and NDVI were nearly identical in both land cover types across the U.S.
- Calculated net radiation (R_n) values, one of the energy balance components, were nearly identical in all locations across the U.S.
- Due to the different algorithms which are used in the models for computation of ground heat flux (G), there were considerable differences between G and sensible heat flux (H), two other key energy balance components.
- The main products of the models are reference ET fraction (ET_rF), and ET_a. Comparisons revelled that EEFlux automated calibrated algorithms are capable of estimating reliable ET_rF and ET_a values in agricultural areas.

- However, as the EEFlux is still in the progress the functionality of the EEFlux needs to be improved in non-agricultural areas.

In the final Chapter 5, the summarized major findings from this dissertation are presented as well as some potential future directions in ET_a estimation are discussed.

1.3 Contribution to Co-authored Publications

The core chapters of this dissertation (Chapters 2 through 4) have already been published or are submitted to journals and conferences. The full references follow:

- Chapter 2: Foolad, F., Franz, T. E., Wang, T., Gibson, J., Kilic, A., Allen, R. G., and Suyker, A. (March 2017) "Feasibility analysis of using inverse modeling for estimating field-scale evapotranspiration in maize and soybean fields from soil water content monitoring networks", Hydrol. Earth Syst. Sci., 21, 1263-1277, doi:10.5194/hess-21-1263-2017.
- Chapter 3: Foolad, F., Franz, T. E., Wang, T., Kilic, A., Allen, R. G., Abadi, A. M., and Ratcliffe, I. (June 2018) "Combining remote and proximal sensing to estimate evapotranspiration in a riparian ecosystem in central Nebraska", (9th International Congress on Environmental Modelling and Software 2018, Fort Collins, Colorado, USA).
- Chapter 4: Foolad, F., Blankenau, P., Kilic, A., Allen, R. G., Huntington, J., Erickson, T. A., Ozturk, D., Morton, C. G., Ortega-Salazar, S., Ratcliffe, I., Franz, T. E., Thau, D., Moore, R., Gorelick, N., Kamble, B., Revelle, P., Trezza, R., Zhao

W., and Robison, C. W. (June 2018) "Comparison of the Automatically Calibrated Google Evapotranspiration Application - EEFlux and the Manually Calibrated METRIC Application", (Submitted to Remote Sensing Journal).

1.4 References

Allen, R. G., C Morton, B Kamble, A Kilic, J Huntington, D Thau, N Gorelick, et al. 2015. "EEFlux: A Landsat-Based Evapotranspiration Mapping Tool on the Google Earth Engine." In , 1–11. American Society of Agricultural and Biological Engineers. https://doi.org/10.13031/irrig.20152143511.

Allen, R. G., M Tasumi, A. T. Morse, R Trezza, J. L. Wright, W. G. M. Bastiaanssen, W Kramber, I Lorite, and C. W. Robison. 2007. "Satellite-Based Energy Balance for Mapping Evapotranspiration with Internalized Calibration (METRIC)—Applications." *Journal of Irrigation and Drainage Engineering* 133 (4): 395–406. https://doi.org/10.1061/(ASCE)0733-9437(2007)133:4(395).

Allen, R. G., M Tasumi, and R Trezza. 2007. "Satellite-Based Energy Balance for Mapping Evapotranspiration with Internalized Calibration (METRIC)—Model." *Journal of Irrigation and Drainage Engineering* 133 (4): 380–94. https://doi.org/10.1061/(ASCE)0733-9437(2007)133:4(380).

Anayah, F. M., and J. J. Kaluarachchi. 2014. "Improving the Complementary Methods to Estimate Evapotranspiration under Diverse Climatic and Physical Conditions." *Hydrology and Earth System Sciences; Katlenburg-Lindau* 18 (6): 2049. http://dx.doi.org/10.5194/hess-18-2049-2014.

Anthoni, Peter M., Beverly E. Law, and Michael H. Unsworth. 1999. "Carbon and Water Vapor Exchange of an Open-Canopied Ponderosa Pine Ecosystem." *Agricultural and Forest Meteorology* 95 (3): 151–68. https://doi.org/10.1016/S0168-1923(99)00029-5.

Binley, Andrew, Susan S. Hubbard, Johan A. Huisman, André Revil, David A. Robinson, Kamini Singha, and Lee D. Slater. 2015. “The Emergence of Hydrogeophysics for Improved Understanding of Subsurface Processes over Multiple Scales.” *Water Resources Research* 51 (6): 3837–66. https://doi.org/10.1002/2015WR017016.

Blad, Blaine L., and Norman J. Rosenberg. 1974. “Lysimetric Calibration of the Bowen Ratio-Energy Balance Method for Evapotranspiration Estimation in the Central Great Plains.” *Journal of Applied Meteorology* 13 (2): 227–36. https://doi.org/10.1175/1520-0450(1974)013<0227:LCOTBR>2.0.CO;2.

Desilets, Darin, and Marek Zreda. 2013. “Footprint Diameter for a Cosmic-Ray Soil Moisture Probe: Theory and Monte Carlo Simulations.” *Water Resources Research* 49 (6): 3566–75. https://doi.org/10.1002/wrcr.20187.

Dong, Jingnuo, Tyson E. Ochsner, Marek Zreda, Michael H. Cosh, and Chris B. Zou. 2014. “Calibration and Validation of the COSMOS Rover for Surface Soil Moisture Measurement.” *Vadose Zone Journal* 13 (4). https://doi.org/10.2136/vzj2013.08.0148.

Franz, Trenton E., Ammar Wahbi, Mariette Vreugdenhil, Georg Weltin, Lee Heng, Markus Oismueller, Peter Strauss, Gerd Dercon, and Darin Desilets. 2016. “Using Cosmic-Ray Neutron Probes to Monitor Landscape Scale Soil Water Content in Mixed Land Use Agricultural Systems.” *Applied and Environmental Soil Science*. https://doi.org/10.1155/2016/4323742.

Franz, Trenton E., M. Zreda, T. P. A. Ferre, R. Rosolem, C. Zweck, S. Stillman, X. Zeng, and W. J. Shuttleworth. 2012. “Measurement Depth of the Cosmic Ray Soil Moisture Probe Affected by Hydrogen from Various Sources.” *Water Resources Research* 48 (8): W08515. https://doi.org/10.1029/2012WR011871.

Godfray, H. Charles J., John R. Beddington, Ian R. Crute, Lawrence Haddad, David Lawrence, James F. Muir, Jules Pretty, Sherman Robinson, Sandy M. Thomas, and Camilla

Toulmin. 2010. "Food Security: The Challenge of Feeding 9 Billion People." *Science* 327 (5967): 812–18. https://doi.org/10.1126/science.1185383.

Gorelick, N, M Hancher, M Dixon, S Ilyushchenko, D Thau, and R Moore. 2017. "Google Earth Engine: Planetary-Scale Geospatial Analysis for Everyone." *Remote Sensing of Environment*, Big Remotely Sensed Data: tools, applications and experiences, 202 (December): 18–27. https://doi.org/10.1016/j.rse.2017.06.031.

Irmak, S. 2010. "Nebraska Water and Energy Flux Measurement, Modeling, and Research Network (NEBFLUX)." *Transactions of the ASABE* 53 (4): 1097–1115. https://doi.org/10.13031/2013.32600.

Kizer, M. A., and R. L. Elliott. 1991. "Eddy Correlation Systems for Measuring EVAPOTRANSPIRATION." *Transactions of the ASAE* 34 (2): 0387–92. https://doi.org/10.13031/2013.31673.

Mancosu, Noemi, Richard L. Snyder, Gavriil Kyriakakis, and Donatella Spano. 2015. "Water Scarcity and Future Challenges for Food Production." *Water* 7 (3): 975–92. https://doi.org/10.3390/w7030975.

Massman, W. J. 1992. "A Surface Energy Balance Method for Partitioning Evapotranspiration Data into Plant and Soil Components for a Surface with Partial Canopy Cover." *Water Resources Research* 28 (6): 1723–32. https://doi.org/10.1029/92WR00217.

McCabe, Matthew F., Matthew Rodell, Douglas E. Alsdorf, Diego G. Miralles, Remko Uijlenhoet, Wolfgang Wagner, Arko Lucieer, et al. 2017. "The Future of Earth Observation in Hydrology." *Hydrology and Earth System Sciences; Katlenburg-Lindau* 21 (7): 3879–3914. http://dx.doi.org/10.5194/hess-21-3879-2017.

Porkka, Miina, Dieter Gerten, Sibyll Schaphoff, Stefan Siebert, and Matti Kummu. 2016. "Causes and Trends of Water Scarcity in Food Production." *Environmental Research Letters* 11 (1): 015001. https://doi.org/10.1088/1748-9326/11/1/015001.

Price, Martin. 1986. "The Analysis of Vegetation Change by Remote Sensing." *Progress in Physical Geography: Earth and Environment* 10 (4): 473–91. https://doi.org/10.1177/030913338601000401.

Sun, G., A. Noormets, J. Chen, and S. G. McNulty. 2008. "Evapotranspiration Estimates from Eddy Covariance Towers and Hydrologic Modeling in Managed Forests in Northern Wisconsin, USA." *Agricultural and Forest Meteorology*, Chequamegon Ecosystem-Atmosphere Study Special Issue: Ecosystem-Atmosphere Carbon and Water Cycling in the Temperate Northern Forests of the Great Lakes Region, 148 (2): 257–67. https://doi.org/10.1016/j.agrformet.2007.08.010.

Swinbank, W. C. 1951. "The Measurement of Vertical Transfer of Heat and Water Vapor by Eddies in the Lower Atmosphere." *Journal of Meteorology* 8 (3): 135–45. https://doi.org/10.1175/1520-0469(1951)008<0135:TMOVTO>2.0.CO;2.

Tanner, C. B. 1960. "Energy Balance Approach to Evapotranspiration from Crops." *Soil Science Society of America Journal* 24 (1): 1–9. https://doi.org/10.2136/sssaj1960.03615995002400010012x.

Wilson, Kell B, Paul J Hanson, Patrick J Mulholland, Dennis D Baldocchi, and Stan D Wullschleger. 2001. "A Comparison of Methods for Determining Forest Evapotranspiration and Its Components: Sap-Flow, Soil Water Budget, Eddy Covariance and Catchment Water Balance." *Agricultural and Forest Meteorology* 106 (2): 153–68. https://doi.org/10.1016/S0168-1923(00)00199-4.

Zhang, Baozhong, Shaozhong Kang, Fusheng Li, and Lu Zhang. 2008. "Comparison of Three Evapotranspiration Models to Bowen Ratio-Energy Balance Method for a Vineyard in an Arid Desert Region of Northwest China." *Agricultural and Forest Meteorology* 148 (10): 1629–40. https://doi.org/10.1016/j.agrformet.2008.05.016.

Zreda, M., D. Desilets, T. P. A. Ferré, and R. L. Scott. 2008. “Measuring Soil Moisture Content Non-Invasively at Intermediate Spatial Scale Using Cosmic-Ray Neutrons.” *Geophysical Research Letters* 35 (21): L21402. https://doi.org/10.1029/2008GL035655.

Zreda, M., W. J. Shuttleworth, X. Zeng, C. Zweck, D. Desilets, T. E. Franz, and R. Rosolem. 2012. “COSMOS: The COsmic-Ray Soil Moisture Observing System.” *Hydrol. Earth Syst. Sci.* 16 (11): 4079–99. https://doi.org/10.5194/hess-16-4079-2012.

CHAPTER 2: FEASIBILITY ANALYSIS OF USING INVERSE MODELING FOR ESTIMATING FIELD-SCALE EVAPOTRANSPIRATION IN MAIZE AND SOYBEAN FIELDS FROM SOIL WATER CONTENT MONITORING NETWORKS

2.1 Abstract

In this study the feasibility of using inverse vadose zone modeling for estimating field scale actual evapotranspiration (ET_a) was explored at a long-term agricultural monitoring site in eastern Nebraska. Data from both point scale soil water content (SWC) sensors and the area-average technique of Cosmic-Ray Neutron Probes were evaluated against independent ET_a estimates from a co-located Eddy-Covariance tower. While this methodology has been successfully used for estimates of groundwater recharge, it was essential to assess the performance of other components of the water balance such as ET_a. In light of recent evaluations of Land Surface Models (LSM) independent estimates of hydrologic state variables and fluxes are critically needed benchmarks. The results here indicate reasonable estimates of daily and annual ET_a from the point sensors, but with highly varied soil hydraulic function parameterizations due to local soil texture variability. The results of multiple soil hydraulic parameterizations leading to equally good ET_a estimates is consistent with the hydrological principle of equifinality. While this study focused on one particular site, the framework can be easily applied to other SWC monitoring networks across the globe. The value added products of groundwater recharge and ET_a flux from the SWC monitoring networks will provide additional and more robust benchmarks for the validation of LSM that continues to improve their forecast skill. In

addition, the value added products of groundwater recharge and ET_a often have more direct impacts on societal decision making than SWC alone. Water flux impacts human decision making from policies on the long-term management of groundwater resources (recharge), to yield forecasts (ET_a), and to optimal irrigation scheduling (ET_a). Illustrating the societal benefits of SWC monitoring is critical to insure the continued operation and expansion of these public datasets.

2.2 Introduction

Evapotranspiration (ET) is an important component in terrestrial water and surface energy balance. In the United States, ET comprises about 75% of annual precipitation, while in arid and semiarid regions ET comprises more than 90% of annual precipitation (Zhang et al., 2001; Glenn et al., 2007; Wang et al., 2009a). As such, an accurate estimation of ET is critical in order to predict changes in hydrological cycles and improve water resource management (Suyker et al., 2008; Anayah and Kaluarachchi, 2014). Given the importance of ET, an array of measurement techniques at different temporal and spatial scales have been developed (c.f., Maidment, 1992; Zhang et al., 2014), including lysimeter, Bowen ratio, Eddy-Covariance (EC), and satellite-based surface energy balance approaches. However, simple, low-cost, and accurate field-scale measurements of actual ET (ET_a) still remain a challenge due to the uncertainties of available estimation techniques (Wolf et al., 2008; Li et al., 2009; Senay et al., 2011; Stoy, 2012). For instance, field techniques, such as EC and Bowen ratio, can provide relatively accurate estimation of local ET_a, but are often cost prohibitive for wide-spread use beyond research applications

(Baldocchi et al., 2001; Irmak, 2010). By comparison, satellite-based remote sensing techniques are far less costly for widespread spatial coverage (Allen et al., 2007), but are limited by their accuracy, temporal sampling frequency (e.g., Landsat 8 has a 16-day overpass), and technical issues that further limit temporal sampling periods (e.g., cloud coverage during overpass) (Chemin and Alexandridis, 2001; Xie et al., 2008; Li et al., 2009; Kjaersgaard et al., 2012).

As a complement to the above-mentioned techniques, recent studies have used process-based vadose zone models (VZMs) for estimating field-scale ET_a with reasonable success, particularly in arid and semi-arid areas (Twarakavi et al., 2008; Izadifar and Elshorbagy, 2010; Galleguillos et al., 2011; Wang et al., 2016). Although VZMs are time and cost effective for estimating field-scale ET_a, they generally require complex model parameterizations and inputs, some of which are not readily available (e.g., soil hydraulic parameters and plant physiological parameters; c.f. Wang et al., 2016). In order to address the issue of missing soil hydraulic parameters, a common approach is to use pedotransfer functions to convert readily available soil information (e.g., texture, bulk density, etc.) to soil hydraulic parameters (Wösten et al., 2001); however, significant uncertainties are usually associated with this method for estimating local scale water fluxes (Wang et al., 2015). In fact, Nearing et al. (2016) identified soil hydraulic property estimation as the largest source of information lost when evaluating different land surface modeling schemes versus a soil moisture benchmark. Poor and uncertain parameterization of soil hydraulic properties is a clear weakness of land surface models (LSMs) predictive skill in sensible and latent heat fluxes (Best et al., 2015). This problem will continue to compound with the continuing spatial refinement of hyper-resolution LSM grid cells to less than 1 km (Wood et al., 2011).

In order to address the challenge of field scale estimation of soil hydraulic properties, here we utilize inverse modeling for estimating soil hydraulic parameters based on field measurements of soil water content (SWC) (c.f. Hopmans and Šimunek, 1999; Ritter et al., 2003). While VZM-based inverse approaches have already been examined for estimating groundwater recharge (e.g., Jiménez-Martínez et al., 2009; Andreasen et al., 2013; Min et al., 2015; Ries et al., 2015; Turkeltaub et al., 2015; Wang et al., 2016), its application for ET_a estimation has not been adequately tested. Moreover, we note that simultaneous estimation of SWC states and surface energy fluxes within LSMs is complicated by boundary conditions, model parameterization, and model structure (Nearing et al., 2016). With the incorporation of regional soil datasets in LSMs like Polaris (Chaney et al., 2016), effective strategies for estimating ground truth soil hydraulic properties from existing SWC monitoring networks (e.g., SCAN, CRN, COSMOS, State/National Mesonets, c.f. Xia et al. (2015)) will become critical for continuing to improve the predictive skill of LSMs.

The aim of this study is to examine the feasibility of using inverse VZM for estimating field scale ET_a based on long-term local meteorological and SWC observations for an Ameriflux (Baldocchi et al., 2001) EC site in eastern Nebraska, USA. We note that while this study focused on one particular study site in eastern Nebraska, the methodology can be easily adapted to a variety of SWC monitoring networks across the globe (Xia et al., 2015), thus providing an extensive set of benchmark data for use in LSMs. The remainder of the paper is organized as follows. In the methods section we will describe the widely used VZM, Hydrus-1D (Šimunek et al., 2013), used to obtain soil hydraulic parameters. We will assess the feasibility of using both profiles of in-situ SWC probes as well as the area-average SWC technique from Cosmic-Ray Neutron Probes (CRNP). In the results section we will compare simulated ET_a resulted from calibrated VZM with independent ET_a estimates provided by EC observations. Finally, a sensitivity analysis of key soil and plant parameters will be presented.

2.3 Materials and Methodology

2.3.1 Study Site

The study site is located in eastern Nebraska, USA at the University of Nebraska Agricultural and Development Center near Mead. The field site (US-Ne3, Figure 2.1a, 41.1797° N, 96.4397° W) is part of the Ameriflux Network (Baldocchi et al., 2001) and has been operating continually since 2001. The regional climate is of a continental semiarid type with a mean annual precipitation of 784 mm/year (according to the Ameriflux US-Ne3 website). According to the Web Soil Survey Data (Soil Survey Staff, 2016, http://websoilsurvey.nrcs.usda.gov/), the soils at the site are comprised mostly of silt loam and silty clay loam (Figure 2.1b and Table 2.1). Soybean and maize are rotationally grown at the site under rainfed conditions, with the growing season beginning in early May and ending in October (Kalfas et al., 2011). Since 2001, crop management practices (i.e., planting density, cultivars, irrigation, and herbicide and pesticide applications) have been applied in accordance with standard best management practices prescribed for production-scale maize systems (Suyker et al., 2008). More detailed information about site conditions can be found in Suyker et al. (2004) and Verma et al. (2005).

Table 2.1. Variability of soil texture in the study field based on Web Soil Survey data (http://websoilsurvey.sc.egov.usda.gov/App/HomePage.htm).

Map Unit Symbol	Map Unit Name	Clay (%)	Silt (%)	Sand (%)	Hectares in Field	Percent of Field
3948	Fillmore silt loam, terrace, occasionally ponded	41.7	51.0	7.3	3.24	4.9%
7105	Yutan silty clay loam, terrace, 2 to 6 percent slopes, eroded	25.8	59.4	14.8	6.88	10.3%
7280	Tomek silt loam, 0 to 2 percent slopes	32.3	61.6	6.1	47.23	70.8%
7340	Filbert silt loam, 0 to 1 percent slopes	41.4	51.7	6.9	9.34	14.0%
Total Area of Field					66.69	100.0%

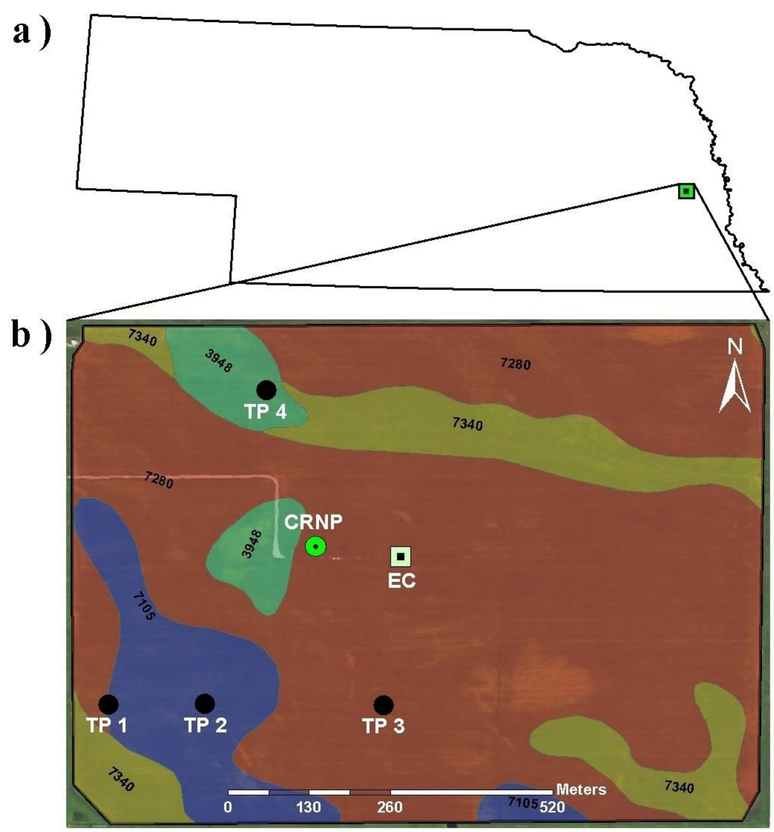

Figure 2.1. Study site (Mead Rainfed/US-Ne3) location in Nebraska (a) and locations of Eddy-Covariance Tower (EC), Cosmic-Ray Neutron Probe (CRNP), Theta Probes (TPs), and variability of soil texture based on Web Soil Survey data at the study site, 2014 (b). See table 2.1 for soil descriptions.

An EC tower was constructed at the center of the field (Figure 2.1 and Figure 2.2a), which continuously measures water, energy, and CO_2 fluxes (e.g., Baldocchi et al., 1988). At this field, sensors are mounted at 3.0 m above the ground when the canopy is shorter than 1.0 m. At canopy heights greater than 1.0 m, the sensors are then moved to a height of 6.2 m until harvest in order to have sufficient upwind fetch (in all directions) representative of the cropping system being studied (Suyker et al., 2004). In this study, hourly latent heat flux measurements were integrated to daily values and then used for calculating daily EC ET_a integrated over the field scale. Detailed information on the EC measurements and calculation procedures for ET_a are given in Suyker and Verma (2009). Hourly air temperature, relative humidity, horizontal wind speed, net radiation, and precipitation were also measured at the site. Destructive measurements of leaf area index (LAI) were made every 10 to 14 days during the growing season at the study site (Suyker et al., 2005). We note that the LAI data were linearly interpolated to provide daily estimates. Theta probes (TP) (Delta-T Devices, Cambridge, UK) (https://www.delta-t.co.uk/product/ml3/) were installed at 4 locations in the study field with measurement depths of 10, 25, 50, and 100 cm at each location to monitor hourly SWC in the root zone (Suyker et al., 2008). Here, we denote these four locations as TP 1 (41.1775° N, 96.4442° W), TP 2 (41.1775° N, 96.4428° W), TP 3 (41.1775° N, 96.4402° W), and TP 4 (41.1821° N, 96.4419° W) (Figure 2.1b). Daily precipitation (P) and reference evapotranspiration (ET_r) computed for the tall (alfalfa) reference crop using the ASCE standardized Penman-Monteith equation (ASCE-EWRI 2005) are shown in Figure 2.3 for the study period (2007–2012) at the study site.

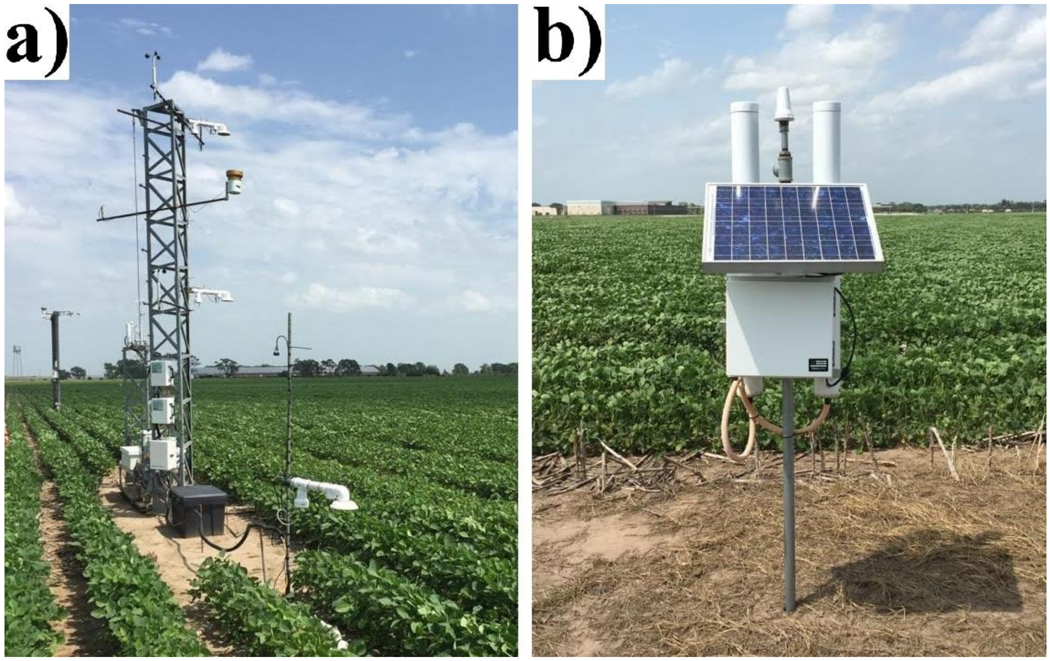

Figure 2.2. Eddy-Covariance Tower (a) and Cosmic-Ray Neutron Probe (b) Located at the Mead Rainfed (US-Ne3) Site.

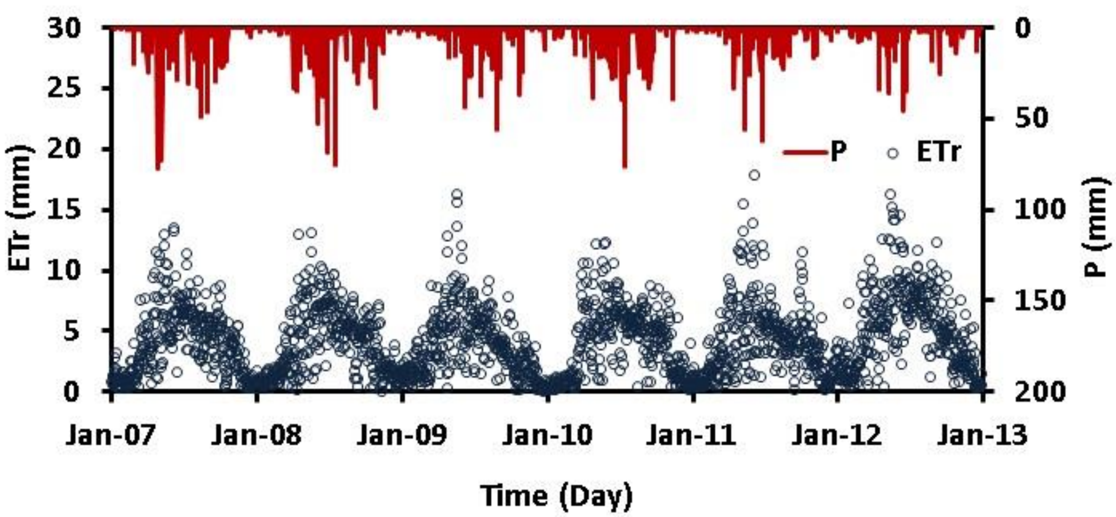

Figure 2.3. Daily precipitation (P) and reference evapotranspiration (ET_r) during the calibration (2008–2010) and validation (2011–2012) periods at the Mead Rainfed (US-Ne3) Site.

In addition, a CRNP (model CRS 2000/B, HydroInnova LLC, Albuquerque, NM, USA, 41.1798 N°, 96.4412° W) (http://hydroinnova.com/ps_soil.html#overview) was installed near the EC tower (Figure 2.1b and 2.2b) on 20 April 2011. The CRNP measures hourly moderated neutron counts (Zreda et al., 2008, 2012), which are converted into SWC following standard correction procedures and calibration methods (c.f., Zreda et al., 2012). In addition, the changes in above-ground biomass were removed from the CRNP estimates of SWC following Franz et al. (2015). The CRNP measurement depth (Franz et al., 2012) at the site varies between 15-40 cm, depending on SWC. Note for simplicity in this analysis we assume the CRNP has an effective depth of 20 cm (mean depth of 10 cm) for all observational periods. The areal footprint of the CRNP is ~250+/-50 m radius circle (see Desilets and Zreda 2013 and Köhli et al., 2015 for details). Here we assume for simplicity the EC and CRNP footprints are both representative of the areal-average field conditions.

2.3.2 Model setup

2.3.2.1 Vadose Zone Model

The Hydrus-1D model (Šimunek et al., 2013), which is based on the Richards equation, was used to calculate ET_a. The setup of the Hydrus-1D model is explained in detail by Jiménez-Martínez et al. (2009), Min et al. (2015), and Wang et al. (2016), and only a brief description of the model setup is provided here. Given the measurement depths of the Theta Probes, the simulated soil profile length was chosen to be 175 cm with 176 nodes at 1 cm intervals. An atmospheric boundary condition with surface runoff was selected as the upper boundary. This allowed the occurrence of surface runoff when precipitation rates were higher than soil infiltration capacity or if the soil became saturated. According to a nearby USGS monitoring well (Saunders County, NE, USGS

411005096281502, ~2.7 km away), the depth to water tables was greater than 12 m during the study period. Therefore, free drainage was used as the lower boundary condition.

Based on ASCE Penman-Monteith equation, ET_r values can be computed for either grass or alfalfa and then using crop-specific coefficients daily potential evapotranspiration (ET_p) can be calculated. Here daily ET_r values were calculated for the tall (0.5 m) ASCE reference (ASCE-EWRI, 2005), and daily potential evapotranspiration (ET_p) was calculated according to FAO 56 (Allen et al., 1998):

$$ET_p(t) = K_C(t) \times ET_r(t) \tag{1}$$

where Kc is a crop-specific coefficient at time t. The estimates of growth stage lengths and Kc values for maize and soybean suggested by Allen et al. (1998) and Min et al. (2015) were adopted in this study. In order to partition daily ET_p into potential transpiration (T_p) and potential evaporation (E_p) as model inputs, Beer's law (Šimunek et al., 2013) was used as follows:

$$E_p(t) = ET_p(t) \times e^{-k \times LAI(t)} \tag{2}$$

$$T_p(t) = ET_p(t) - E_p(t) \tag{3}$$

where k [-] is an extinction coefficient with a value set to 0.5 (Wang et al., 2009b) and LAI [L^2/L^2] is leaf area index described in the previous section. The root water uptake, S(h), was simulated according to the model of Feddes et al. (1978):

$$S(h) = \alpha(h) \times S_p \tag{4}$$

where α(h) [-] is the root-water uptake water stress response function and varies between 0 and 1 depending on soil matric potentials, and S_p is the potential water uptake rate and assumed to be equal to T_p. The summation of actual soil evaporation and actual transpiration is ET_a.

Since the study site has annual cultivation rotations between soybean and maize, the root growth model from the Hybrid-Maize Model (Yang et al., 2004) was used to model the root growth during the growing season:

$$\begin{cases} if\ D < MRD,\ D = \frac{AGDD}{GDD_{Silking}} MRD \\ \qquad or\ D = MRD \end{cases} \tag{5}$$

where D (cm) is plant root depth for each growing season day, MRD is the maximum root depth (assumed equal to 150 cm for maize and 120 cm for soybean in this study following Yang et al., 2004), AGDD is the accumulated growing degree days, and $GDD_{Silking}$ is the accumulated GDD at the silking point (e.g., accumulated plant GDD approximately 60-70 days after crop emergence). GDD for each growing season day was calculated as:

$$GDD = \frac{T_{max} - T_{min}}{2} - T_{base} \tag{6}$$

where T_{max} and T_{min} are the maximum and minimum daily temperature (^{0}C), respectively, and T_{base} is the base temperature set to be 10^0 C following McMaster and Wilhelm (1997) and Yang et al. (1997). Finally, the Hoffman and van Genuchten (1983) model was used to calculate root distribution. Further details about the model can be found in Šimunek et al. (2013).

2.3.2.2 Inverse modeling to estimate soil hydraulic parameters

Inverse modeling was used to estimate soil hydraulic parameters for the van Genuchten-Mualem model (Mualem, 1976; van Genuchten, 1980):

$$\theta(h) = \begin{cases} \theta_r + \frac{\theta_s - \theta_r}{(1+|\alpha h|^n)^m}, h < 0 \\ \theta_s,\ h \geq 0 \end{cases} \tag{7}$$

$$K(S_e) = K_s \times S_e^{l} \times [1-(1-S_e^{1/m})^m]^2 \tag{8}$$

where θ [L^3/L^3] is volumetric SWC; θ_r [L^3/L^3] and θ_s [L^3/L^3] are residual and saturated water content, respectively; h [L] is pressure head; K [L/T] and K_s [L/T] are unsaturated and saturated hydraulic conductivity, respectively; and $S_e = (\theta-\theta_r)/(\theta_s-\theta_r)$ [-] is saturation degree. With respect to the fitting factors, α [1/L] is inversely related to air entry pressure, n [-] measures the pore size distribution of a soil with $m=1-1/n$, and l [-] is a parameter accounting for pore space tortuosity and connectivity.

Daily SWC data from the four TP locations and CRNP location were used for the inverse modeling. Based on the measurement depths of the TPs, the simulated soil columns were divided into four layers for TP locations (i.e., 0-15 cm, 15-35 cm, 35-75 cm, and 75-175 cm), which led to a total of 24 hydraulic parameters (θ_r, θ_s, α, n, K_s, and l) to be optimized based on observed SWC values. In order to efficiently optimize the parameters, we used the method outlined in Turkeltaub et al. (2015). Since Hydrus-1D is limited to optimizing a maximum of 15 parameters at once and that the SWC of the lower layers changes more slowly and over a smaller range than the upper layers, the van Genuchten parameters of the upper two layers were first optimized, while the parameters of the lower two layers were fixed. Then, the optimized van Genuchten parameters of the upper two layers were kept constant, while the parameters of the lower two layers were optimized. The process was continued until there were no further improvements in the optimized hydraulic parameters or until the changes in the lowest sum of squares were less than 0.1%. Given the sensitivity of the optimization results to the initial guesses of soil hydraulic parameters in the Hydrus model, soil hydraulic parameters from six soil textures were used as initial inputs for the optimizations at each location (Carsel and Parish, 1988), including sandy clay loam, silty clay loam, loam, silt loam, silt, and clay loam. Based on the length of available SWC data from the TP measurements, the periods of 2007, 2008-2010, and 2011-2012 were used as the spin-up, calibration, and validation periods, respectively. Moreover, to minimize the impacts of freezing conditions on the quality of SWC measurements, data from January to March of each calendar year were removed (based on available soil temperature data) from the optimizations.

In addition to the TP profile observations, we used the CRNP area-average SWC in the inverse procedure to develop an independent set of soil parameters. The CRNP was assumed to provide SWC data with an average effective measurement depth of 20 cm at this study site. The observation point was therefore set at 10 cm. As a first guess and in the absence of other information, soil properties were assumed to be homogeneous throughout the simulated soil column with a length of 175 cm. Because the CRNP was installed in 2011 at the study site, the periods of 2011, 2012-2013, and 2014 were used as spin-up, calibration, and validation periods, respectively, for the optimization procedure.

Table 2.2. Bounds of the van Genuchten parameters used for inverse modeling.

Soil Parameter	θ_r (-)	θ_s (-)	α (1/cm)	n (-)	K_s (cm/day)	l (-)
Range	0.03–0.30	0.3–0.6	0.001–0.200	1.01–6.00	1–200	-1–1

The lower and upper bounds of each van Genuchten parameter are provided in Table 2.2. With respect to the goodness-of-fit assessment, Root Mean Square Error (RMSE) between simulated and observed SWC was chosen as the objective function to minimize in order to estimate the soil hydraulic parameters. The built in optimization procedure in Hydrus-1D was used to perform parameter estimation. A sensitivity analysis of the six soil model parameters was performed. In addition, three additional performance criteria, including Coefficient of Determination (R^2), Mean Average Error (MAE), and the Nash-Sutcliffe Efficiency (NSE) were used to further evaluate and validate the selected model behavior:

$$RMSE = \sqrt{\frac{1}{n}\sum_{i=1}^{n}(P_i - O_i)^2} \tag{9}$$

$$R^2 = \left(\frac{n(\sum_{i=1}^{n} P_i O_i) - (\sum_{i=1}^{n} P_i)(\sum_{i=1}^{n} O_i)}{\sqrt{[n\sum_{i=1}^{n} P_i{}^2 - (\sum_{i=1}^{n} P_i)^2][n\sum_{i=1}^{n} O_i{}^2 - (\sum_{i=1}^{n} O_i)^2]}}\right)^2 \tag{10}$$

$$MAE = \frac{1}{\mathrm{n}}\sum_{\mathrm{i=1}}^{\mathrm{n}}|\mathrm{P_i} - \mathrm{O_i}| \tag{11}$$

$$\mathrm{NSE} = 1 - \frac{\sum_{\mathrm{i=1}}^{\mathrm{n}}(\mathrm{P_i} - \mathrm{O_i})^2}{\sum_{\mathrm{i=1}}^{\mathrm{n}}(\mathrm{O_i} - \bar{\mathrm{O}}_\mathrm{i})^2} \tag{12}$$

where n is the total number of SWC data points, O_i, and P_i, are respectively the observed and simulated daily SWC on day i, and $\bar{O}_i$ is the observed mean value. Based on the best scores (i.e., lowest RMSE values), the best optimized set of soil hydraulic parameters at each location were selected. Using the selected parameters, the Hydrus model was then run in a forward mode in order to estimate ET_a between 2007 and 2012. Finally, we note that the years 2004-2006 were used as a model spin-up period for the forward model and evaluation of ET_a because of the longer climate record length.

2.4 Results and Discussions

2.4.1 Vadose Zone Inverse Modeling Results

The time series of the average SWC from the four TP locations along with one standard deviation at each depth are plotted in Figure 2.4. Based on the large spatial standard deviation values (Figure 2.4), despite the relatively small spatial scale (~65 ha) and uniform cropping at the study site, SWC varies considerably across the site, particularly during the growing season. The comparison between SWC data from the CRNP and spatial average of SWC data at the four TP locations in the study field (i.e. average of 10 and 25 cm depths at TP locations) is presented in Figure 2.5. The daily RMSE between the spatial average of the TPs and CRNP data is 0.037 cm^3/cm^3, which is consistent with other studies that reported similar values in semiarid shrublands (Franz et al., 2012), German Forests (Bogena et al., 2013, Baatz et al., 2014), montane forests in Utah (Lv et al., 2014), sites across Australia (Hawdon et al., 2014), and a mixed land use agricultural site in Austria (Franz et al. 2016). We note that we would expect lower RMSE (~<0.02 cm^3/cm^3) with additional point sensors located at shallower depths and in more locations distributed across the study site. Nevertheless, the consistent behavior between the spatial mean SWC of TPs and the CRNP allows us to explore spatial variability of soil hydraulic properties within footprint using inverse modeling. This will be described in the next sections. The study period (2007-2012, Figure 2.6) contained significant inter-annual variability in precipitation. During the spin-up period in 2007, the annual precipitation (942 mm) was higher than the mean annual precipitation (784 mm), 2008 was a wet year (997 mm), 2009-2011 were near average years (715 mm), and 2012 was a record dry year (427 mm) with widespread drought across the region. Therefore, both wet and dry years were considered in the inverse modeling simulation period.

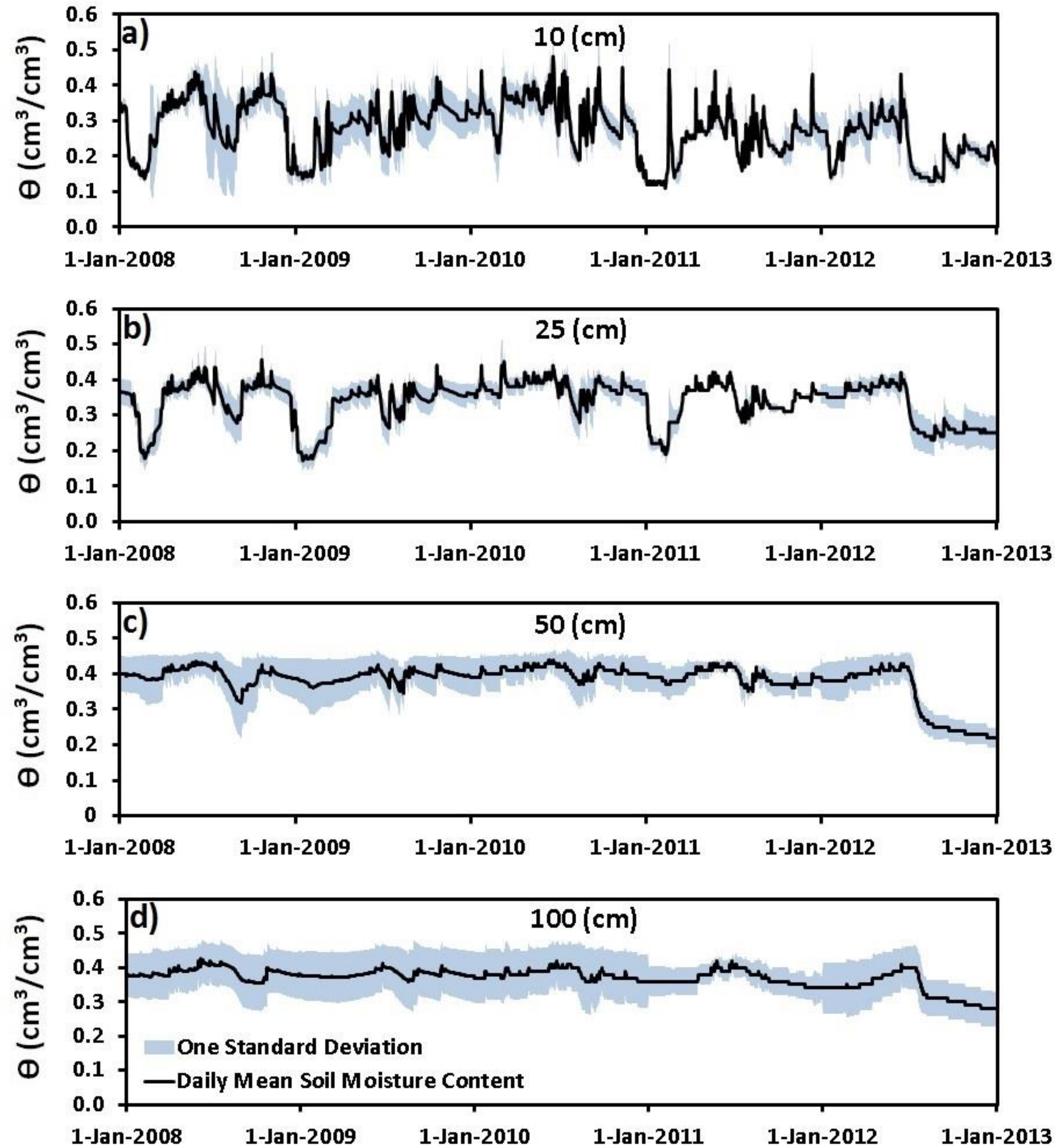

Figure 2.4. Temporal evolution of daily SWC (θ) at different soil depths. The black lines represent daily mean SWC (θ) calculated from TPs in 4 different locations at study site and the blue areas indicate one standard deviation.

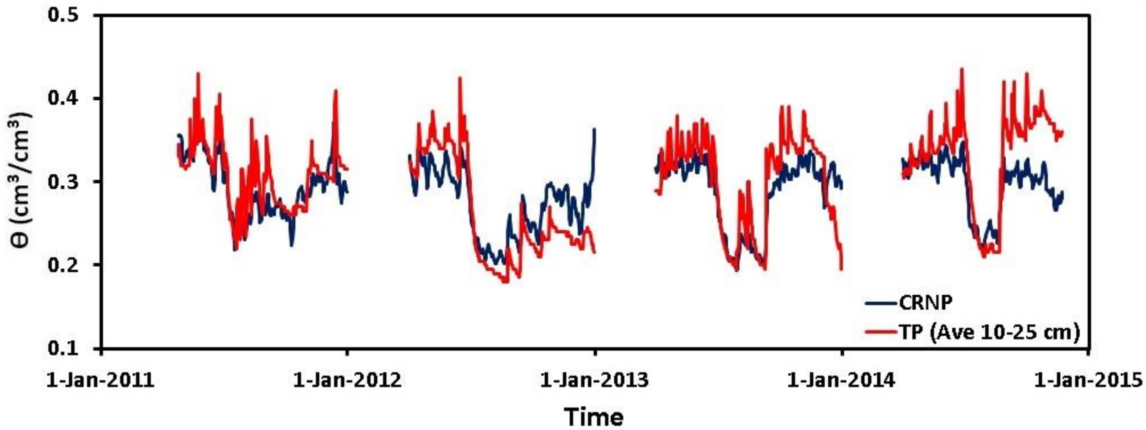

Figure 2.5. Time series of daily CRNP and spatial average TP SWC (θ) data.

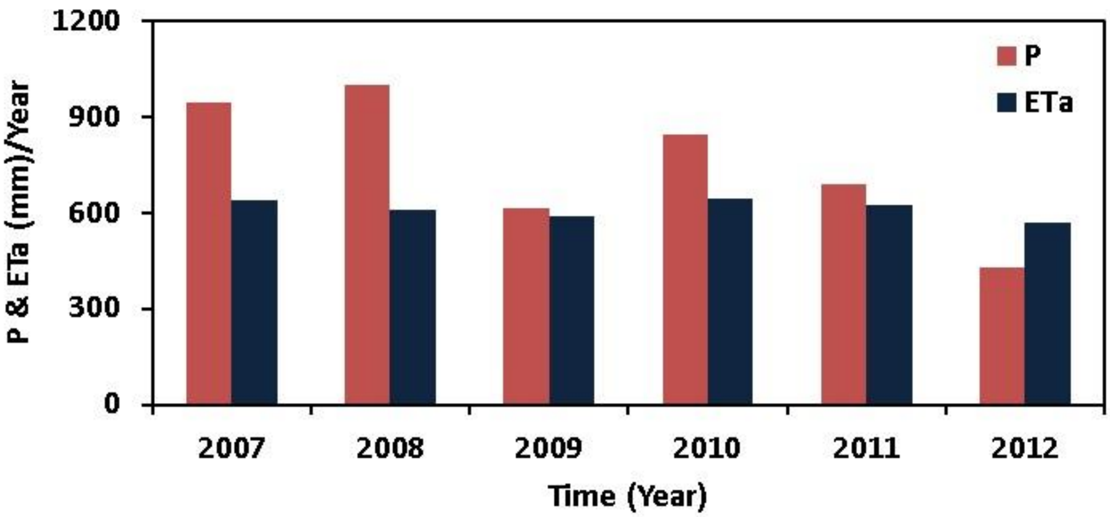

Figure 2.6. Annual precipitation (P) and annual actual evapotranspiration (ET_a) at the Mead Rainfed (US-Ne3) Site.

As an illustration, Figure 2.7 shows the daily observed and simulated SWC during the calibration (2008–2010) and validation (2011–2012) periods at the TP 1 location (the simulation results of the other three sites can be found in the supplemental Figures 2.1, 2.2, and 2.3). The results of objective function criterion (RMSE) and the other three performance criteria (e.g., R^2, MAE, and NSE) between simulated and observed SWC values at TPs locations are presented in Table 2.3.

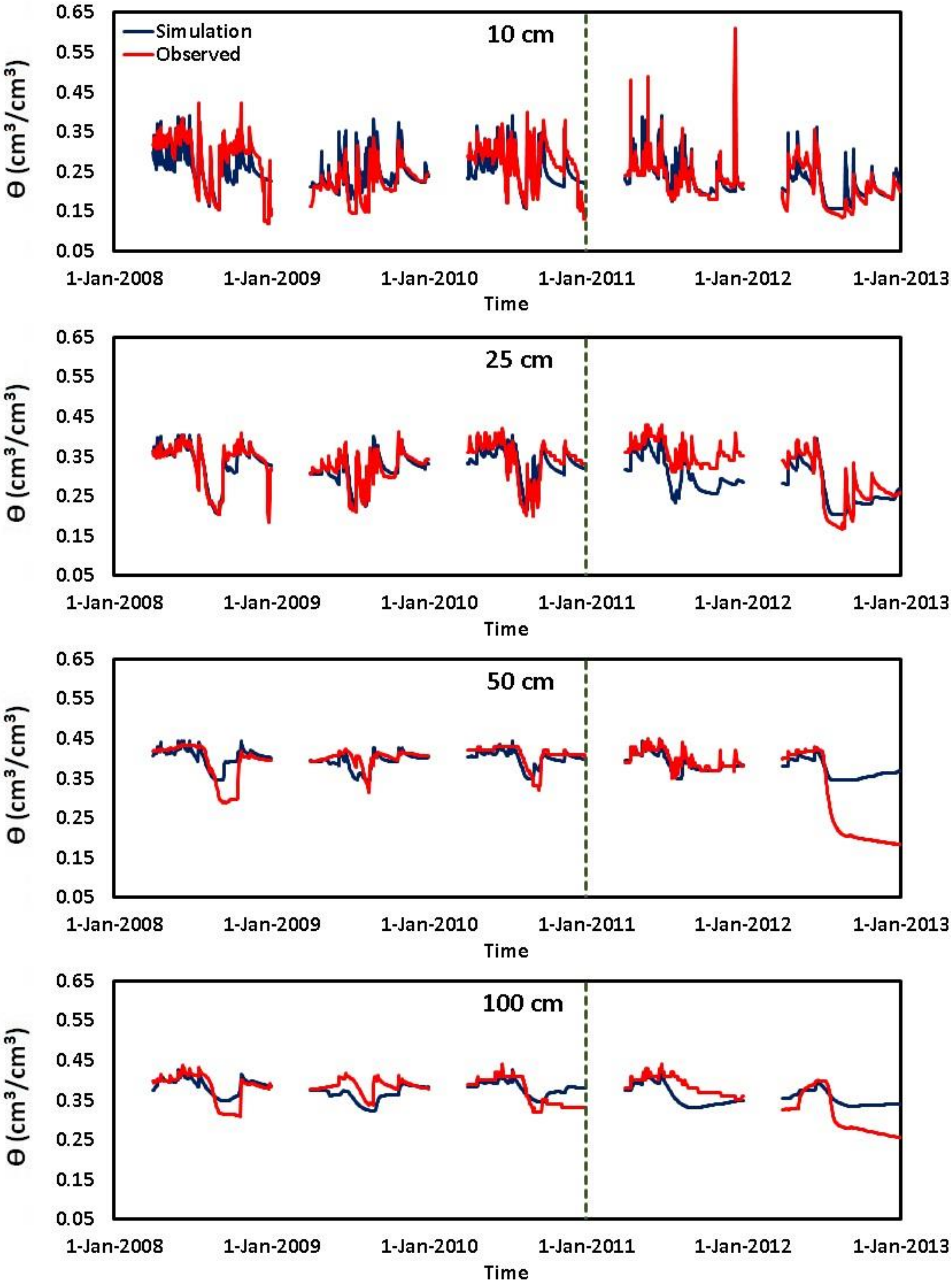

Figure 2.7. Daily observed and simulated SWC (θ) during the calibration (2008–2010) and validation (2011–2012) periods at TP 1 location. See supplemental figures for other comparisons.

Table 2.3. Goodness-of-fit measures for simulated and observed SWC data at different depths during the calibration period (2008 to 2010) and validation period (2011-2012) at TPs locations. Note we assume a good fit as an RMSE between 0-0.03 cm^3/cm^3 and fair as between 0.03-0.06 cm^3/cm^3.

Location	Depth (cm)	Calibration Period (2008-2010)				Validation Period (2011-2012)			
		R^2	MAE (cm^3/cm^3)	RMSE (cm^3/cm^3)	NSE	R^2	MAE (cm^3/cm^3)	RMSE (cm^3/cm^3)	NSE
TP 1	10	0.542	0.024	0.036	0.533	0.532	0.016	0.033	0.503
	25	0.742	0.014	0.022	0.739	0.716	0.029	0.040	0.486
	50	0.409	0.013	0.023	0.407	0.603	0.041	0.074	0.157
	100	0.352	0.015	0.022	0.343	0.419	0.027	0.038	0.358
TP 2	10	0.330	0.044	0.066	0.305	0.287	0.047	0.061	0.052
	25	0.623	0.010	0.020	0.604	0.718	0.038	0.055	0.135
	50	0.551	0.015	0.026	0.074	0.683	0.040	0.055	0.202
	100	0.424	0.019	0.027	-2.055	0.344	0.048	0.073	-0.473
TP 3	10	0.269	0.034	0.051	0.256	0.534	0.086	0.102	-4.265
	25	0.512	0.011	0.017	0.509	0.852	0.010	0.015	0.793
	50	0.549	0.015	0.023	-0.214	0.658	0.022	0.033	0.652
	100	0.238	0.018	0.029	-3.156	0.669	0.018	0.025	0.178
TP 4	10	0.412	0.029	0.044	0.406	0.580	0.051	0.071	-0.116
	25	0.434	0.016	0.025	0.350	0.594	0.029	0.042	0.490
	50	0.151	0.009	0.015	-13.400	0.443	0.041	0.073	0.036
	100	0.001	0.013	0.021	-12.058	0.292	0.026	0.039	0.238

In this research we define RMSE values less than 0.03 cm^3/cm^3 between observed and simulated SWC values as well-matched and RMSE between 0.03 and 0.06 cm^3/cm^3 as fairly well-matched. We note the target error range of satellite SWC products (e.g. SMOS and SMAP) is less than 0.04 cm^3/cm^3 (Entekhabi et al., 2010). Similar to previous studies (e.g., Jiménez-Martínez et al., 2009; Andreasen et al., 2013; Min et al., 2015; Wang et al., 2016), the results of all the performance criteria at TP locations show the capability of inverse modeling in estimation of soil hydraulic parameters. The results of the calibration period (2008-2010) indicate that the simulated and observed SWC values are in good agreement (i.e. well matched as defined above) throughout the entire period at most locations and depths (Figure 2.7 and Table 2.3). In addition, the simulated and observed SWC data are fairly well-matched at most locations and depths during the validation period (2011-2012), with notable differences during the second half of 2012 during the extreme drought conditions (Figure 2.7 and Table 2.3). Reasons for this disagreement in the observed and simulated SWC data will be discussed in the following sections.

The results of inverse modeling using the CRNP data also indicate the feasibility of using these data to estimate effective soil hydraulic parameters (Figure 2.8 and Table 2.4). Based on the performance criteria (Table 2.4), the simulated data are fairly well-matched with the observed SWC data during both the calibration and validation periods. Additional information from deeper soil probes or more complex modeling approaches such as data assimilation techniques (Rosolem et al., 2014, Renzullo et al., 2014) may be needed to fully utilize the CRNP data for the entire growing season. However, this was beyond the scope of the current study and merits further investigation given the global network of CRNP (Zreda et al., 2012) dating back to ~2011.

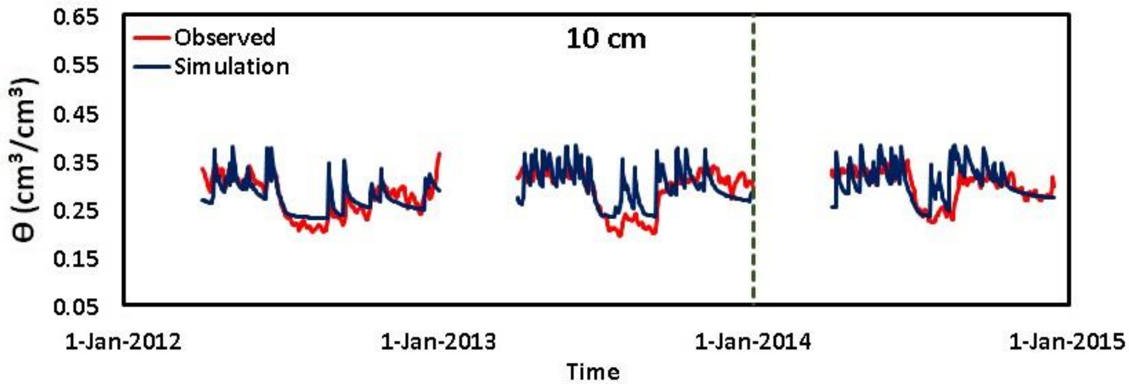

Figure 2.8. Daily observed and simulated SWC (θ) during the calibration (2012–2013) and validation (2014) periods at the location of Cosmic-Ray Neutron probe.

Table 2.4. Goodness-of-fit measures for simulated and observed SWC data during the calibration period (2012 to 2013) and validation period (2014) at CRNP location.

Location	Depth (cm)	Calibration Period (2012-2013)				Validation Period (2014)			
		R^2	MAE (cm^3/cm^3)	RMSE (cm^3/cm^3)	NSE	R^2	MAE (cm^3/cm^3)	RMSE (cm^3/cm^3)	NSE
CRNP	10	0.497	0.018	0.027	0.456	0.192	0.020	0.032	-0.310

Table 2.5 summarizes the optimized van Genuchten parameters for the four different depths of the four TP locations and the single layer for the CRNP location. The optimized parameters were then used to estimate ET_a for the entire study period as an independent comparison to the EC ET_a data. The results of the ET_a evaluation will be discussed in the next section. According to the simulation results (Table 2.5), in most of the soil layers, the TP 4 location results in lower n, K_s, and higher θ_r values than the other 3 locations (TPs 1-3), suggesting either underlying soil texture variability in the field or texture dependent sensor sensitivity/calibration. As a validation for the simulation results, the publicly available Web Soil Survey Data (http://websoilsurvey.nrcs.usda.gov/) was used to explore whether the optimized van Genuchten parameters from the inverse

modeling (Figure 2.1b and Table 2.2) agreed qualitatively with the survey data. Based on the Web Soil Survey Data, the soil at the TP 4 location contains higher clay percentage than the other locations. Meanwhile, the optimized parameters reflect the spatial pattern of soil texture in the field as shown by the Web Soil Survey Data (e.g., lower n and K_s values and higher θ_r values at the TP 4 location with finer soil texture). Physically, finer-textured soils generally have lower K_s and higher θ_r values (Carsel and Parrish, 1988). Moreover, the shape factor n is indicative of pore size distributions of soils. In general, finer soils with smaller pore sizes tend to have lower n values (Carsel and Parrish, 1988). The observed SWC at the TP 4 location is consistently higher than the average SWC of the other three locations (Figure 2.4 in supplemental materials), which can be partly attributed to the higher θ_r values at the TP 4 location (Wang and Franz, 2015). Overall, the obtained van Genuchten parameters from the inverse modeling are in qualitatively good agreement with the available spatial distribution of soil texture in the study field, indicating the capability of using inverse VZM to infer soil hydraulic properties. Further work on validating the Web Soil Survey Data soil hydraulic property estimates is of general interest to the LSM community.

Table 2.5. Optimized van Genuchten parameters in different locations at the study site.

Location	Depth (cm)	θ_r (-)	θ_s (-)	α (1/cm)	n (-)	K_s (cm/day)	l (-)
TP 1	0-15	0.134	0.423	0.027	1.475	8.119	0.546
	15-35	0.136	0.408	0.007	1.345	11.540	0.480
	35-75	0.191	0.448	0.024	1.097	8.057	0.285
	75-175	0.071	0.430	0.025	1.069	9.807	0.364
TP 2	0-15	0.211	0.446	0.027	1.567	8.120	1.000
	15-35	0.197	0.434	0.006	1.191	8.655	0.022
	35-75	0.110	0.424	0.015	1.239	4.605	0.723
	75-175	0.109	0.408	0.020	1.302	6.780	0.000
TP 3	0-15	0.281	0.464	0.035	1.487	7.096	0.400
	15-35	0.072	0.402	0.012	1.085	29.960	0.353
	35-75	0.081	0.498	0.037	1.128	24.440	0.527
	75-175	0.085	0.500	0.039	1.147	17.540	0.496
TP 4	0-15	0.082	0.481	0.034	1.172	7.773	0.953
	15-35	0.200	0.426	0.013	1.217	14.060	0.044
	35-75	0.250	0.477	0.009	1.079	1.045	0.353
	75-175	0.200	0.487	0.012	1.070	1.454	0.985
CRNP	0-15	0.100	0.392	0.019	1.154	6.931	0.547

2.4.2 Comparison of modeled ET_a with observed ET_a

Because a longer set of climatic data was available at the study site (as compared to SWC data), we used 2004-2006 as a spin-up period. Using the best fit soil hydraulic parameters for the four TP locations and the single CRNP location, the Hydrus-1D model was then run in a forward mode to calculate ET_a over the entire study period (2007-2012).

The simulated daily ET_a was then compared with the independent EC ET_a measurements using RMSE (Eq. (9)) as the evaluation criterion. In order to upscale TP ET_a estimation to the field/EC scale, we used the soil textural boundaries and areas defined by the Web Soil Survey Data map to compute a weighted average ET_a. In this research we consider RMSE values less than 1 mm/day between observed and simulated ET_a values as well-matched and RMSE values between 1 and 1.2 as fairly well-matched (Figure 2.9 and Table 2.6). The performance criterion results indicate that the simulated daily ET_a is in a better agreement with EC ET_a measurements at the TP 1-3 locations than at the TP 4 and CRNP locations (Table 2.6). However, based on the performance criteria from inverse modeling results and on the Web Soil Survey Data, we conclude that spatial heterogeneity of soil texture in the study field results in significant spatial variation in ET_a rates across the field (e.g., less ET_a occurs at the TP 4 location than from the other parts of the field). Here smaller ET_a rates at the TP 4 location are likely due to finer soil texture at this location, which makes it more difficult for the plant/roots to overcome potentials to extract water from the soil, thus leading to a lower ET_a rate and greater plant stress. In addition, higher surface runoff can be expected at the TP 4 location due to finer-textured soils (as we observed during our field campaigns). According to the simulation results the average surface runoff at the TP 4 location was about 44.8 mm/year from 2007 to 2012, while the average surface runoff at the other three locations (TPs 1-3) was around 10.6 mm/year, which partially accounts for the lower ET_a rates. We note that future work using historic yield maps may also be used to further elucidate the soil hydraulic property differences given the direct correlation between transpiration and yield.

Table 2.6. Goodness-of-fit measures for simulated and observed daily ET_a during the simulation period (2007-2012) at study site.

Location	R^2	MAE (mm/day)	RMSE (mm/day)	NSE
ET_p	0.510	1.359	1.992	0.340
TP 1	0.644	0.696	1.062	0.618
TP 2	0.754	0.610	0.907	0.746
TP 3	0.751	0.601	0.904	0.728
TP 4	0.365	0.878	1.387	0.168
TPs Weighted Average	0.742	0.599	0.911	0.714
CRNP	0.573	0.742	1.143	0.562

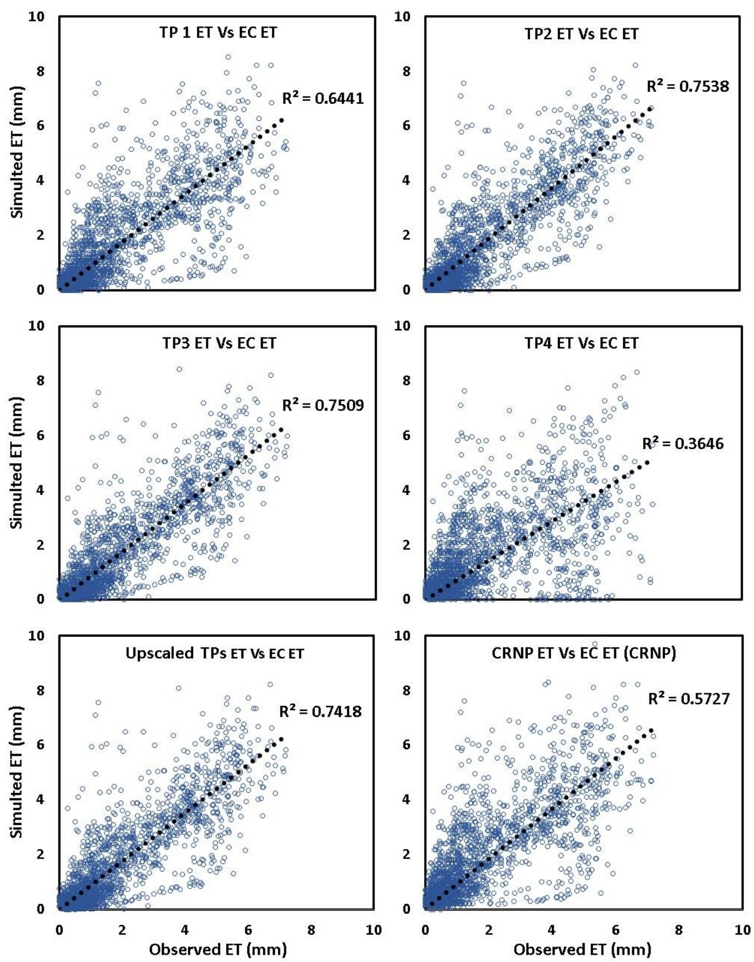

Figure 2.9. Simulated daily ET_a versus observed daily ET_a at different locations in the study site (2007-2012).

Given that CRNPs have a limited observational depth and that only one single soil layer was optimized in the inverse model for the CRNP, one could expect the simulated daily ET_a from the CRNP to have larger uncertainty. Here we found an RMSE of 1.14 mm/day using the CRNP versus 0.91 mm/day for the upscaled TP locations. However, when the optimized soil parameters obtained from the CRNP data were used to estimate ET_a, the model did simulate daily ET_a fairly well during both non-growing and growing seasons in comparison to the EC ET_a measurements.

Table 2.7. Summary of simulated yearly and average actual evapotranspiration (ET_a) (mm) and observed yearly and average actual evapotranspiration (ET_a) (mm) from Eddy-Covariance tower during 2007 to 2012.

Location	Year						
	2007	2008	2009	2010	2011	2012	Average
ET_p	1048.5	987.9	989.4	1011.5	1025.7	1326.7	1064.9
EC	656.8	608.4	589.7	646.1	622.2	570.1	612.5
TP 1	646.1	629.0	559.8	642.1	573.9	415.5	579.5
TP 2	614.3	598.4	576.7	620.5	576.9	429.5	574.7
TP 3	529.0	556.1	556.4	590.4	549.8	405.2	545.4
TP 4	652.2	576.1	529.9	677.3	458.2	381.2	525.3
Upscaled TPs	613.9	564.1	556.3	600.3	547.7	405.9	548.0
CRNP	745.3	707.1	603.0	721.8	642.2	439.3	643.1

On the annual scale, ET_a measured by the EC tower accounted for 87% of annual P recorded at the site during the study period (Figure 2.6). Overall, the simulated annual ET_a at all the TP and CRNP locations is comparable to the annual ET_a measured by the EC tower, except during 2012 (Table 2.7), in which a severe drought occurred in the region. One explanation is that the plants extract more water from deeper layers under extreme drought conditions than what we defined as a maximum rooting depth (150 cm for maize and 120 cm for soybean) for the model, thus limiting the VZM ability to estimate ET_a accurately during the drought year (2012). In fact, based on the EC ET_a measurements at the study site, there was just 8.18% reduction in annual ET_a in 2012 than the average of the other years (2007-2011), while there were 29.58% and 35.75% reduction in annual simulated ET_a values respectively in upscaled TP and CRNP. This shows that although 2012 was a very dry year, the plants probably found most of the needed water by extracting water from deeper soil reservoirs. As previously mentioned we defined a maximum rooting depth for the model that could greatly impact the results. To further illustrate this point, a sensitivity analysis was performed on the maximum rooting depth and presented in the following section. However, we note that given the fact that EC ET_a estimation can have up to 20% uncertainty (Massman and Lee, 2002, and Hollineger and Richardson, 2005), and accounting for the natural spatial variability of ET_a due to soil texture and root depth growth uncertainties, the various ET_a estimation techniques performed fairly well. In fact, it is difficult to identify which ET_a estimation method is the most accurate method. These results are consistent with the concept of equifinality in hydrologic modeling given the complexity of natural systems (Beven and Freer, 2001). Moreover, the findings here are consistent with Nearing et al. (2016) that show information lost in model parameters greatly affects the soil moisture comparisons against a benchmark. However, soil parameterization was less important in the loss of information for the comparisons of ET/latent energy against a benchmark. Fully resolving these issues remains a key challenge to the land surface modeling community and the model's ability to make accurate predictions (Best 2015). The following section provides a detailed sensitivity analysis of the soil hydraulic parameters and root depth growth functions in order to begin to understand the sources of error in estimating ET_a from SWC monitoring networks.

2.4.3 Sensitivity analysis of soil hydraulic parameters and rooting depth

In this research we compared simulated ET_a with the measured EC ET_a. As expected some discrepancies between simulated and measured ET_a values existed. In order to begin to understand the key sources of error we performed a set of sensitivity analysis experiments on the estimated soil hydraulic parameters. Building on Wang et al. (2009b), a sensitivity analysis for a single homogeneous soil layer (6 parameters) and a 4-layer soil profile (24 parameters) was performed over the study period (2007–2012). Here we performed a preliminary sensitivity analysis by changing a single soil hydraulic parameter one at a time while keeping the other parameters constant (i.e. at the average value). Figure 2.10 illustrates the sensitivity results on simulated ET_a, indicating the soil hydraulic parameters have a range of sensitivities with tortuosity (l) being the least. We found that n and α were the most sensitive, particularly in the shallowest soil layer. This sensitivity to the shallowest soil layer provides an opportunity to use the CRNP observations, particularly in the early growing season (i.e. when evaporation dominates latent energy flux), to help constrain estimates of n and α. As the crop continues to develop (and transpiration contributes a relatively larger component of latent energy) additional information about deeper soil layers should be used to estimate soil hydraulic parameters or perform data assimilation. Moreover, the CRNP may be useful in helping constrain and parameterize soil hydraulic functions in simpler evaporation models widely used in remote sensing (c.f. Allen et al. 2007) and crop modeling (c.f. Allen et al. 1998).

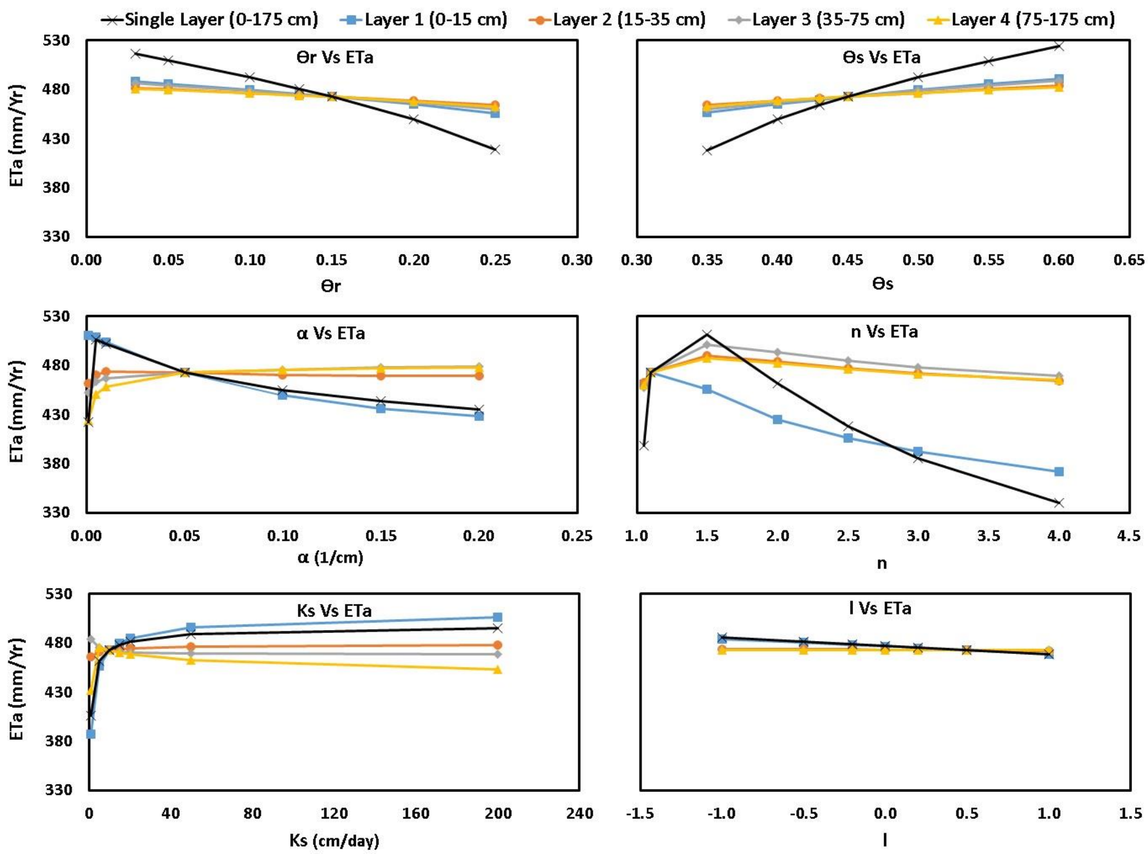

Figure 2.10. Sensitivity analysis of the effect of soil hydraulic parameters on average annual ET_a values (2007-2012) for a single homogeneous soil layer (6 parameters) and for a 4-layer soil profile (24 parameters).

Following the sensitivity analysis, we repeated the optimization experiment using only α, n, K_s, and used model default estimates for the other parameters in each layer. We found that the RMSE values were significantly higher (1.511 vs. 0.911 mm/day) than when considering all 24 parameters. We suspect that given the high correlation between soil hydraulic parameters (Carsel and Parrish 1988), that fixing certain parameters leads to a degradation in overall performance. We suggest further sensitivity analyses, in particular changing multiple parameters simultaneously or using multiple objective functions, be used to fully understand model behavior (c.f. Bastidas et al. 1999 and Rosolem et al. 2012).

A sensitivity analysis of ET_a by varying rooting depth is summarized in Figure 2.11. As would be expected with increasing rooting depth, higher ET_a occurred. In addition, Figure 2.11 illustrates a decreasing RMSE against EC observations for up to 200% increases. Again it is unclear if the EC observations are biased high or in fact rooting depths are much greater than typically considered in these models. The high observed EC values in the drought year of 2012 indicate that roots likely uptake water from below the 1 m observations. Certainly the results shown here further indicate the importance of root water uptake parameters in VZMs and LSMs, even in homogeneous annual cropping systems. While beyond the scope of this paper we refer the reader to the growing literature on the importance of root water uptake parameters on hydrologic fluxes (c.f. Schymanski et al. 2008 and Guswa 2012).

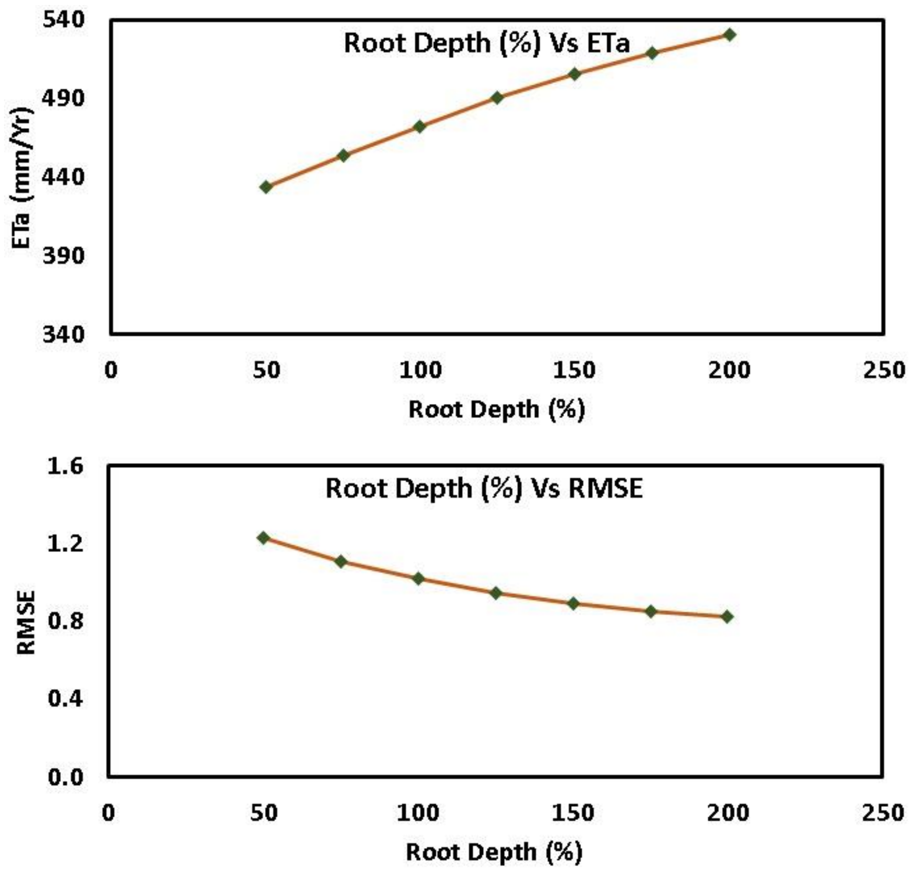

Figure 2.11. Sensitivity analysis of root depth on ET_a estimation for a single homogeneous soil layer profile. Note that root depth is in terms of percent depth as it is dynamic over the growing period.

2.4.4 Applications and limitations of the vadose zone modeling framework

Given its simplicity and widespread availability of ground data, ET_r and Kc values are often used in a wide variety of applications to estimate ET_p and thus approximate ET_a. It is well known that SWC is a limiting factor affecting the assumption that $ET_p \sim ET_a$. On the other hand, we know that SWC observations are local in nature and not necessarily representative of ET_a footprint estimates. The key questions are: what is the value of SWC observations, how many profiles do we need to install in a footprint, and at which depths to constrain estimates of fluxes? The well instrumented and long-term study presented here allows us to start to answer these key questions. First we find that ET_p has an average annual value of 1064.9 mm as compared to EC at 612.5 mm (Table 2.7). By including individual SWC profiles (TP 1 to 4) and the CRNP in the VZM framework we are able to constrain our estimate of ET_a to between 525.3 and 643.1 mm and reduce ET_a RMSE from 1.992 mm/day to around 1 mm/day (Table 2.6). In addition, a range of soil hydraulic parameters for each depth and spatially averaged top layer can be estimated to help better constrain recharge fluxes simultaneously. Given the principle of equifinality in hydrologic systems, the VZM framework may lead to equally reasonable estimates of parameters which is a limitation of the method and LSMs in general. Based on our sensitivity analysis (Figure 2.10) the key parameters of α, n may greatly affect ET_a.

Although sparsely distributed, widespread state, national, and global meteorological observations paired with SWC profiles (Xia et al. 2015) and the VZM framework provide an opportunity to better constrain ET_a and local soil hydraulic functions. Moreover, where multiple SWC profile information is available a range of ET_a and soil hydraulic parameters can be estimated and thus considered in LSM data assimilation frameworks. The combination of basic metrological observations with a CRNP in the VZM framework further allows for estimates of upscaled soil hydraulic parameters with similar estimates of ET_a as found with individual SWC profiles. Moving forward, combining CRNP with deeper SWC observations from point sensors seems to be a reasonable strategy in order to average the inherent SWC variability in the near surface yet provide SWC constraints at depth, particularly as annual crops develop over the growing season.

2.5 Conclusions

In this study the feasibility of using inverse vadose zone modeling for field scale ET_a estimation was explored at an agricultural site in eastern Nebraska. Both point SWC sensors (TP) and area-average techniques (CRNP) were explored. This methodology has been successfully used for estimates of groundwater recharge, but it was critical to assess the performance of other components of the water balance such as ET_a. The results indicate reasonable estimates of daily and annual ET_a but with varied soil hydraulic function parameterizations. The varied soil hydraulic parameters were expected given the heterogeneity of soil texture at the site and consistent with the principle of equifinality in hydrologic systems. We note that while this study focused on one particular site, the framework can be easily applied to other networks of SWC monitoring across the globe (Xia et al., 2015). The value-added products of groundwater recharge and ET_a flux from the SWC monitoring networks will provide additional and more robust benchmarks for the validation of LSM that continue to improve their forecast skill.

2.6 Data availability

The climatic and EC data used in this research can be found at http://ameriflux.lbl.gov/. The TP SWC and LAI data in the study site are provided by Dr. Andrew Suyker and CRNP SWC are provided by Dr. Trenton E. Franz and both sets of data can be requested directly from the authors. The US soil taxonomy information is provided by Soil Survey Staff and is available online at http://websoilsurvey.nrcs.usda.gov/

(accessed in July, 2016). The remaining datasets are provided in the supplemental material associated with this paper.

2.7 Acknowledgments

This research is supported financially by the Daugherty Water for Food Global Institute at the University of Nebraska, NSF EPSCoR FIRST Award, the Cold Regions Research Engineering Laboratory through the Great Plains CESU, and an USGS104b grant. We sincerely appreciate the support and the use of facilities and equipment provided by the Center for Advanced Land Management Information Technologies, School of Natural Resources and data from Carbon Sequestration Program, the University of Nebraska-Lincoln. TEF would like to thank Eric Wood for his inspiring research and teaching career. No doubt the skills TEF learned while at Princeton in formal course work, seminars, and discussions with Eric will serve him well in his own career.

2.8 References

Allen, R. G., Pereira, L. S., Raes, D., & Smith, M. (1998). Crop evapotranspiration guidelines for computing crop water requirements-FAO irrigation and drainage paper 56. FAO, Rome, 300(9), D05109.

Allen, R. G., Tasumi, M., & Trezza, R. (2007). Satellite-based energy balance for mapping evapotranspiration with internalized calibration (METRIC)—Model. Journal of Irrigation and Drainage Engineering, 133(4), 380-394.

Anayah, F. M., & Kaluarachchi, J. J. (2014). Improving the complementary methods to estimate evapotranspiration under diverse climatic and physical conditions. Hydrology and Earth System Sciences, 18(6), 2049-2064.

Andreasen, M., Andreasen, L. A., Jensen, K. H., Sonnenborg, T. O., & Bircher, S. (2013). Estimation of regional groundwater recharge using data from a distributed soil moisture network. Vadose Zone Journal, 12(3)

ASCE – EWRI. (2005). The ASCE Standardized reference evapotranspiration equation. ASCE-EWRI Standardization of Reference Evapotranspiration Task Comm. Report, ASCE Bookstore, ISBN 078440805, Stock Number 40805, 216 pages.

Baatz, R., Bogena, H., Franssen, H. H., Huisman, J., Qu, W., Montzka, C., et al. (2014). Calibration of a catchment scale cosmic-ray probe network: A comparison of three parameterization methods. Journal of Hydrology, 516, 231-244.

Baldocchi, D. D., Hincks, B. B., & Meyers, T. P. (1988). Measuring biosphere-atmosphere exchanges of biologically related gases with micrometeorological methods. Ecology, 1331-1340.

Baldocchi, D., Falge, E., Gu, L., & Olson, R. (2001). FLUXNET: A new tool to study the temporal and spatial variability of ecosystem-scale carbon dioxide, water vapor, and energy flux densities. Bulletin of the American Meteorological Society, 82(11), 2415.

Bastidas, L. A., H. V. Gupta, S. Sorooshian, W. J. Shuttleworth, and Z. L. Yang (1999), Sensitivity analysis of a land surface scheme using multicriteria methods, J. Geophys. Res.-Atmos., 104(D16), 19481-19490. doi:10.1029/1999jd900155.

Best, M., Abramowitz, G., Johnson, H., Pitman, A., Balsamo, G., Boone, A., et al. (2015). The plumbing of land surface models: Benchmarking model performance. Journal of Hydrometeorology, 16(3), 1425-1442.

Beven, K., & Freer, J. (2001). Equifinality, data assimilation, and uncertainty estimation in mechanistic modelling of complex environmental systems using the GLUE methodology. Journal of Hydrology, 249(1), 11-29.

Bogena, H., Huisman, J., Baatz, R., Hendricks Franssen, H., & Vereecken, H. (2013). Accuracy of the cosmic-ray soil water content probe in humid forest ecosystems: The worst case scenario. Water Resources Research, 49(9), 5778-5791.

Carsel, R. F., & Parrish, R. S. (1988). Developing joint probability distributions of soil water retention characteristics. Water Resources Research, 24(5), 755-769.

Chaney, N. W., Wood, E. F., McBratney, A. B., Hempel, J. W., Nauman, T. W., Brungard, C. W., et al. (2016). POLARIS: A 30-meter probabilistic soil series map of the contiguous United States. Geoderma, 274, 54-67.

Chemin, Y., & Alexandridis, T. (2001). Improving spatial resolution of ET seasonal for irrigated rice in Zhanghe, china. Paper Presented at the 22nd Asian Conference on Remote Sensing, 5. pp. 9.

Desilets, D., & Zreda, M. (2013). Footprint diameter for a cosmic-ray soil moisture probe: Theory and monte carlo simulations. Water Resources Research, 49(6), 3566-3575.

Entekhabi, D., E. G. Njoku, P. E. O'Neill, K. H. Kellogg, W. T. Crow, W. N. Edelstein, J. K. Entin, S. D. Goodman, T. J. Jackson, J. Johnson, J. Kimball, J. R. Piepmeier, R. D. Koster, N. Martin, K. C. McDonald, M. Moghaddam, S. Moran, R. Reichle, J. C. Shi, M. W. Spencer, S. W. Thurman, L. Tsang, and J. Van Zyl (2010), The Soil Moisture Active Passive (SMAP) Mission, Proc. IEEE, 98(5), 704-716. doi:10.1109/jproc.2010.2043918.

Feddes, R. A., Kowalik, P. J., & Zaradny, H. (1978). Simulation of field water use and crop yield. Centre for Agricultural Publishing and Documentation.

Franz, T. E., Wahbi, A., Vreugdenhil, M., Weltin, G., Heng, L., Oismueller, M., et al. (2016). Using cosmic-ray neutron probes to monitor landscape scale soil water content in mixed land use agricultural systems. Applied and Environmental Soil Science, 2016.

Franz, T. E., Wang, T., Avery, W., Finkenbiner, C., & Brocca, L. (2015). Combined analysis of soil moisture measurements from roving and fixed cosmic ray neutron probes for multiscale real-time monitoring. Geophysical Research Letters, 42(9), 3389-3396.

Franz, T. E., Zreda, M., Ferre, T., Rosolem, R., Zweck, C., Stillman, S., et al. (2012). Measurement depth of the cosmic ray soil moisture probe affected by hydrogen from various sources. Water Resources Research, 48(8).

Galleguillos, M., Jacob, F., Prévot, L., Lagacherie, P., & Liang, S. (2011). Mapping daily evapotranspiration over a Mediterranean vineyard watershed. Geoscience and Remote Sensing Letters, IEEE, 8(1), 168-172.

Glenn, E. P., Huete, A. R., Nagler, P. L., Hirschboeck, K. K., & Brown, P. (2007). Integrating remote sensing and ground methods to estimate evapotranspiration. Critical Reviews in Plant Sciences, 26(3), 139-168.

Guswa, A. J. (2012), Canopy vs. Roots: Production and Destruction of Variability in Soil Moisture and Hydrologic Fluxes, Vadose Zone Journal, 11(3). doi:10.2136/vzj2011.0159.

Hawdon, A., McJannet, D., & Wallace, J. (2014). Calibration and correction procedures for cosmic-ray neutron soil moisture probes located across Australia. Water Resources Research, 50(6), 5029-5043.

Hollinger, D. Y., & Richardson, A. D. (2005). Uncertainty in eddy covariance measurements and its application to physiological models. Tree Physiology, 25(7), 873-885.

Hopmans, J.W., Šimunek, J., 1999. Review of inverse estimation of soil hydraulic properties. In: van Genuchten, M.Th. Leij, F.J., Wu, L. (Eds.), Proceedings of the International Workshop Characterization and Measurement of Hydraulic Properties of Unsaturated Porous Media. University of California, Riverside, 643–659.

Irmak, S. (2010). Nebraska water and energy flux measurement, modeling, and research network (NEBFLUX). Transactions of the ASABE, 53(4), 1097-1115.

Izadifar, Z., & Elshorbagy, A. (2010). Prediction of hourly actual evapotranspiration using neural networks, genetic programming, and statistical models. Hydrological Processes, 24(23), 3413-3425.

Jiménez-Martínez, J., Skaggs, T., Van Genuchten, M. T., & Candela, L. (2009). A root zone modelling approach to estimating groundwater recharge from irrigated areas. Journal of Hydrology, 367(1), 138-149.

Kalfas, J. L., Xiao, X., Vanegas, D. X., Verma, S. B., & Suyker, A. E. (2011). Modeling gross primary production of irrigated and rain-fed maize using MODIS imagery and CO 2 flux tower data. Agricultural and Forest Meteorology, 151(12), 1514-1528.

Kjaersgaard, J., Allen, R., Trezza, R., Robinson, C., Oliveira, A., Dhungel, R., et al. (2012). Filling satellite image cloud gaps to create complete images of evapotranspiration. IAHS-AISH Publication, 102-105.

Köhli, M., Schrön, M., Zreda, M., Schmidt, U., Dietrich, P., & Zacharias, S. (2015). Footprint characteristics revised for field-scale soil moisture monitoring with cosmic-ray neutrons. Water Resources Research, 51(7), 5772-5790.

Li, Z., Tang, R., Wan, Z., Bi, Y., Zhou, C., Tang, B., et al. (2009). A review of current methodologies for regional evapotranspiration estimation from remotely sensed data. Sensors, 9(5), 3801-3853.

Lv, L., Franz, T. E., Robinson, D. A., & Jones, S. B. (2014). Measured and modeled soil moisture compared with cosmic-ray neutron probe estimates in a mixed forest. Vadose Zone Journal, 13(12)

Maidment, D. R. (1992). Handbook of hydrology. McGraw-Hill Inc.

Massman, W., & Lee, X. (2002). Eddy covariance flux corrections and uncertainties in long-term studies of carbon and energy exchanges. Agricultural and Forest Meteorology, 113(1), 121-144.

McMaster, G. S., & Wilhelm, W. (1997). Growing degree-days: One equation, two interpretations. Agricultural and Forest Meteorology, 87(4), 291-300.

Min, L., Shen, Y., & Pei, H. (2015). Estimating groundwater recharge using deep vadose zone data under typical irrigated cropland in the piedmont region of the north china plain. Journal of Hydrology, 527, 305-315.

Mualem, Y. (1976). A new model for predicting the hydraulic conductivity of unsaturated porous media. Water Resources Research, 12(3), 513-522.

Nearing, G. S., Mocko, D. M., Peters-Lidard, C. D., Kumar, S. V., & Xia, Y. (2016). Benchmarking NLDAS-2 soil moisture and evapotranspiration to separate uncertainty contributions. Journal of Hydrometeorology, 17(3), 745-759.

Renzullo, L. J., Van Dijk, A., Perraud, J., Collins, D., Henderson, B., Jin, H., et al. (2014). Continental satellite soil moisture data assimilation improves root-zone moisture analysis for water resources assessment. Journal of Hydrology, 519, 2747-2762.

Ries, F., Lange, J., Schmidt, S., Puhlmann, H., & Sauter, M. (2015). Recharge estimation and soil moisture dynamics in a Mediterranean, semi-arid karst region. Hydrology and Earth System Sciences, 19(3), 1439-1456.

Ritter, A., Hupet, F., Muñoz-Carpena, R., Lambot, S., & Vanclooster, M. (2003). Using inverse methods for estimating soil hydraulic properties from field data as an alternative to direct methods. Agricultural Water Management, 59(2), 77-96.

Rosolem, R., H. V. Gupta, W. J. Shuttleworth, X. B. Zeng, and L. G. G. de Goncalves (2012), A fully multiple-criteria implementation of the Sobol' method for parameter sensitivity analysis, J. Geophys. Res.-Atmos., 117. doi:10.1029/2011jd016355.

Schaap, M. G., Leij, F. J., & Van Genuchten, M. T. (2001). Rosetta: A computer program for estimating soil hydraulic parameters with hierarchical pedotransfer functions. Journal of Hydrology, 251(3), 163-176.

Schymanski, S. J., M. Sivapalan, M. L. Roderick, J. Beringer, and L. B. Hutley (2008), An optimality-based model of the coupled soil moisture and root dynamics, Hydrology and Earth System Sciences, 12(3), 913-932.

Senay, G. B., Budde, M. E., & Verdin, J. P. (2011). Enhancing the simplified surface energy balance (SSEB) approach for estimating landscape ET: Validation with the METRIC model. Agricultural Water Management, 98(4), 606-618.

Šimunek, J., Šejna, M., Saito, H., Sakai, M., van Genuchten, M.T. (2013). The HYDRUS-1D Software Package for Simulating the One-Dimensional Movement of Water,Heat, and Multiple Solutes in Variably-Saturated Media, Version 4.17.Department of Environmental Sciences, University of California Riverside, Riverside, California, USA, 307 pp.

Soil Survey Staff, Natural Resources Conservation Service, United States Department of Agriculture. Web Soil Survey. Available online at http://websoilsurvey.nrcs.usda.gov/. Accessed in July, 2016.

Stoy, P. (2012). Evapotranspiration and energy flux observations from a global tower network with a critical analysis of uncertainties. AGU Fall Meeting Abstracts, 1. pp. 06.

Suyker, A., Verma, S., Burba, G., Arkebauer, T., Walters, D., & Hubbard, K. (2004). Growing season carbon dioxide exchange in irrigated and rainfed maize. Agricultural and Forest Meteorology, 124(1), 1-13.

Suyker, A. E., & Verma, S. B. (2008). Interannual water vapor and energy exchange in an irrigated maize-based agroecosystem. Agricultural and Forest Meteorology, 148(3), 417-427.

Suyker, A. E., & Verma, S. B. (2009). Evapotranspiration of irrigated and rainfed maize–soybean cropping systems. Agricultural and Forest Meteorology, 149(3), 443-452.

Suyker, A. E., Verma, S. B., Burba, G. G., & Arkebauer, T. J. (2005). Gross primary production and ecosystem respiration of irrigated maize and irrigated soybean during a growing season. Agricultural and Forest Meteorology, 131(3), 180-190.

Suyker, A. E., Verma, S. B., Burba, G. G., & Arkebauer, T. J. (2005). Gross primary production and ecosystem respiration of irrigated maize and irrigated soybean during a growing season. Agricultural and Forest Meteorology, 131(3), 180-190.

Turkeltaub, T., Kurtzman, D., Bel, G., & Dahan, O. (2015). Examination of groundwater recharge with a calibrated/validated flow model of the deep vadose zone. Journal of Hydrology, 522, 618-627.

Twarakavi, N. K. C., Šimůnek, J., & Seo, S. (2008). Evaluating interactions between groundwater and vadose zone using the HYDRUS-based flow package for MODFLOW. Vadose Zone Journal, 7(2), 757-768.

van Genuchten, M. T. (1980). A closed-form equation for predicting the hydraulic conductivity of unsaturated soils. Soil Science Society of America Journal, 44(5), 892-898.

Verma, S. B., Dobermann, A., Cassman, K. G., Walters, D. T., Knops, J. M., Arkebauer, T. J., et al. (2005). Annual carbon dioxide exchange in irrigated and rainfed maize-based agroecosystems. Agricultural and Forest Meteorology, 131(1), 77-96.

Wang, T., & Franz, T. E. (2015). Field observations of regional controls of soil hydraulic properties on soil moisture spatial variability in different climate zones. Vadose Zone Journal, 14(8)

Wang, T., Franz, T. E., Yue, W., Szilagyi, J., Zlotnik, V. A., You, J., et al. (2016). Feasibility analysis of using inverse modeling for estimating natural groundwater recharge from a large-scale soil moisture monitoring network. Journal of Hydrology, 533, 250-265.

Wang, T., Franz, T. E., & Zlotnik, V. A. (2015). Controls of soil hydraulic characteristics on modeling groundwater recharge under different climatic conditions. Journal of Hydrology, 521, 470-481.

Wang, T., Istanbulluoglu, E., Lenters, J., & Scott, D. (2009a). On the role of groundwater and soil texture in the regional water balance: An investigation of the Nebraska sand hills, USA. Water Resources Research, 45(10)

Wang, T., Zlotnik, V. A., Šimunek, J., & Schaap, M. G. (2009b). Using pedotransfer functions in vadose zone models for estimating groundwater recharge in semiarid regions. Water Resources Research, 45(4)

Wolf, A., Saliendra, N., Akshalov, K., Johnson, D. A., & Laca, E. (2008). Effects of different eddy covariance correction schemes on energy balance closure and comparisons with the modified bowen ratio system. Agricultural and Forest Meteorology, 148(6), 942-952.

Wood, E. F., Roundy, J. K., Troy, T. J., Van Beek, L., Bierkens, M. F., Blyth, E., et al. (2011). Hyperresolution global land surface modeling: Meeting a grand challenge for monitoring earth's terrestrial water. Water Resources Research, 47(5)

Wösten, J., Pachepsky, Y. A., & Rawls, W. (2001). Pedotransfer functions: Bridging the gap between available basic soil data and missing soil hydraulic characteristics. Journal of Hydrology, 251(3), 123-150.

Xia, Y., Ek, M. B., Wu, Y., Ford, T., & Quiring, S. M. (2015). Comparison of NLDAS-2 simulated and NASMD observed daily soil moisture. part I: Comparison and analysis. Journal of Hydrometeorology, 16(5), 1962-1980.

Xie, Y., Sha, Z., & Yu, M. (2008). Remote sensing imagery in vegetation mapping: A review. Journal of Plant Ecology, 1(1), 9-23.

Yang, H., Dobermann, A., Cassman, K. G., & Walters, D. T. (2004). Hybrid-maize. A Simulation Model for Corn Growth and Yield. Nebraska Cooperative Extension CD, 9.

Yang, W., Yang, L., & Merchant, J. (1997). An assessment of AVHRR/NDVI-ecoclimatological relations in Nebraska, USA. International Journal of Remote Sensing, 18(10), 2161-2180.

Zhang, L., Dawes, W., & Walker, G. (2001). Response of mean annual evapotranspiration to vegetation changes at catchment scale. Water Resources Research, 37(3), 701-708.

Zhang, Z., Tian, F., Hu, H., & Yang, P. (2014). A comparison of methods for determining field evapotranspiration: Photosynthesis system, sap flow, and eddy covariance. Hydrology and Earth System Sciences, 18(3), 1053-1072.

Zreda, M., Shuttleworth, W., Zeng, X., Zweck, C., Desilets, D., Franz, T., et al. (2012). COSMOS: The cosmic-ray soil moisture observing system. Hydrology and Earth System Sciences, 16(11), 4079-4099.

Zreda, M., Desilets, D., Ferré, T., & Scott, R. L. (2008). Measuring soil moisture content non-invasively at intermediate spatial scale using cosmic-ray neutrons. Geophysical Research Letters, 35(21).

CHAPTER 3: COMBINING REMOTE AND PROXIMAL SENSING TO ESTIMATE EVAPOTRANSPIRATION IN A RIPARIAN ECOSYSTEM IN CENTRAL NEBRASKA

3.1 Abstract

Sound methods for simultaneously estimating hydrologic fluxes and state variables are critical to quantifying the complexity of water consumption from riparian ecosystems that have connected surface and groundwater. While the volume of earth observation data has significantly increased over the past few years, fundamental questions still remain as to how best combine and leverage datasets of state variables and fluxes from different sources and spatiotemporal resolutions. The primary objective of this study was to compare remotely sensed actual evapotranspiration (ET_a) values with both proximal sensed and in-situ observations to elucidate spatiotemporal correlations between ET_a and state variables of soil water content (SWC) and depth to water table (DTWT). The study was conducted at a 132-ha riparian site in Nebraska. Here, we used Landsat-8 data coupled with the Mapping Evapotranspiration at high Resolution with Internalized Calibration (METRIC) model to estimate ET_a. Data from stationary and roving cosmic-ray neutron probes were used to estimate SWC. DTWT was estimated from a network of 16 groundwater wells. Comparisons among the datasets reveal that SWC and ET_a were linearly correlated for shallow-rooted vegetation. The correlation between DTWT and ET_a was weak. A simple statistical model of daily ET_a vs. the time ET integration spline method indicates similar seasonal ET_a between methods in 2015 (wet) but a 20% reduction in 2016 (dry). The difference underscores the need for better accounting of local state variables occurring

between the 16-day Landsat overpasses and some inherent limitations of periodic satellite-based remote sensing of seasonal ET_a.

3.2 Introduction

The volume of earth observation data and associated retrievals has significantly increased over the past few years with technological developments in remote sensing, proximal sensing, in-situ sensors, opportunistic sensing, and citizen science (McCabe et al., 2017). With respect to water resources, these technologies can provide high quality datasets describing fluxes and state variables in time and space, thus opening new avenues of research and commercial activities. For example, satellite remote sensing has been widely used to provide valuable information at scales from local to global, but is often limited by time between repeat overpasses. Many governmental and commercial earth-observing satellites (e.g., MODIS, Landsat, SMOS, GRACE, and CubeSats) have diverse mission objectives that include measuring different types of fluxes, tracking air pollution, and monitoring flood propagation, precipitation, groundwater, terrestrial water storage, and soil water content (SWC) (McCabe et al., 2017). Other technologies such as unmanned aerial systems equipped with multispectral sensors have been used to complement a myriad of in-situ sensors to enable scientists to gain a more comprehensive understanding of components of the hydrological cycle near the surface. In-situ sensors provide more frequent observations in time but are limited by spatial coverage and thus spatial representativeness. A fundamental question still remains as to how to best combine the raw datasets of state variables and fluxes (e.g., groundwater, SWC, and evapotranspiration

(ET)) (Peters-Lidard et al., 2017) at different spatiotemporal resolutions. Moreover, there are remaining questions in how the datasets can best be ingested into complex physically based models to help us to better understand hydrologic budgets and to make informed water management decisions (Clark et al., 2017). In this work, we aimed to investigate and characterize spatiotemporal relationships between hydrologic fluxes and state variables at a riparian study site in central Nebraska.

Given the critical importance of actual evapotranspiration (ET_a) in land surface energy and water budgets, a multitude of studies have investigated its relationship with different state variables such as wind speed, solar radiation, SWC, depth to water table (DTWT), and various land cover types (Chen and Shu, 2006; Foolad et al., 2017; Hays, 2003; Kurc and Small, 2004; Villarreal et al., 2016). In humid regions with an abundance of water supply, ET_a is mostly influenced by meteorological factors and vegetation type (Kurc and Small, 2004; Laio et al., 2001; Rodriguez-Iturbe et al., 2001; Shuttleworth, 1991; Western et al., 2002). By comparison, in arid and semi-arid regions with limited water supply, ET_a is further limited by available SWC (Kurc and Small, 2004; Reynolds et al., 2000; Rodriguez-Iturbe et al., 2001). In riparian systems with shallow groundwater, deep-rooted vegetation may extract water from both unsaturated and saturated zones for ET_a, adding complexity to system behavior and feedbacks, particularly in semi-arid regions (e.g., Acharya et al., 2014; Gribovszki et al., 2008; Groeneveld, 2008; Groeneveld et al., 2007; Loheide et al., 2005; Maxwell and Kollet, 2008; Soylu et al., 2011; Troxell, 1936; White, 1932). This applies to quantifying the impact of groundwater depth on ET_a. Surface-groundwater connections complicate the fundamental understanding of vegetation water and energy limitations on ET_a, and also increase the complexity and computational resources needed to apply physically based models to simulate and predict system dynamics (Maxwell and Condon, 2016; Maxwell and Kollet, 2008).

The complexity of connected surface and groundwater systems in riparian areas requires computationally intensive numerical models, and dense spatiotemporal observations of state variables and fluxes are desirable for calibration, validation, and evaluation of those numerical models for an in-depth understanding of hydrological processes and feedbacks. However, it is generally time-consuming and costly to construct monitoring networks in riparian areas with densely distributed sensors, largely due to the significant spatial heterogeneity in those areas (e.g., Yue et al., 2016). As such, given the data needed to ground-truth a model, it is clear that a strategy for combining remote sensing data with proximal sensing data and in-situ observations is both essential and pragmatic. Here, we combined various data sources to estimate spatiotemporal state variables and fluxes over a 4-year period (2013-2016) in a ~132 ha central Nebraska riparian zone along the Platte River. Specifically, we used Landsat 8 data processed with the Mapping Evapotranspiration at high Resolution with Internalized Calibration (METRIC) model (Allen et al., 2007) to estimate ET_a at a 30 m spatial resolution in the area. We combined this with data from a stationary cosmic-ray neutron probe (CRNP) and a roving CRNP (Franz et al., 2015) to provide near surface spatiotemporal SWC maps at the same spatial scale and overpass times of the Landsat 8 satellite. Lastly, a network of 16 groundwater monitoring wells was used to provide observations of DTWT across the study site.

The primary objective of this study was to compare remotely sensed ET_a values with estimates made using proximal sensing and in-situ observations in order to elucidate the spatiotemporal correlations between hydrological fluxes (ET) and key state variables (SWC, DTWT) at the riparian study site. The site contains three distinct land cover types (i.e., cottonwood, dry ridge grasses, and wet slough grasses), making it an effective location to evaluate the connections between ET_a, SWC, and DTWT across a natural vegetation and ground-water gradient. Given the complexity of riparian ecosystems with connected surface and groundwater interactions and feedbacks, establishing sound methods to simultaneously estimate hydrologic fluxes and state variables is a critical first step to evaluate the reliability of physically based models of the ecosystem.

3.3 Materials and Methodology

3.3.1 Study Area

This study was conducted in conjunction with the Platte River Recovery Implementation Program (https://www.platteriverprogram.org/AboutPRRIP/Pages/Default.aspx) that addresses issues related to endangered species and loss of habitat along the Platte River (Smith, 2011). The study site (~132 ha) on Shoemaker Island, is located in a riparian zone of the Platte River in central Nebraska, USA (Figure 3.1) (Yue et al., 2016). The local climate is of a continental semiarid type with the average annual precipitation of 478 mm and the mean annual temperature of 10.3 °C, based on the long-term climatic data (1995-2016) from the Alda 3W station within the Nebraska High Plains Mesonet (https://mesonet.unl.edu/). Soil pit observations at the study site indicate a dominance of coarse to medium sands in the top 1-2 m. According to the Web Soil Survey data (http://websoilsurvey.nrcs.usda.gov/; Soil Survey Staff, 2017), soils at the site are comprised mostly of Barney-Bolent complex (39.3%), Platte-Bolent complex (22.7%), Bolent-Calamus complex (20.0%), and Gothenburg loam (12.9%). The study area is covered by three distinct land covers, namely cottonwood (a mixture of cottonwood (Populus sect. Aigeiros) and red cedar (Juniperus virginiana)), dry ridge grasses (e.g., Poa pratensis and Carex sp.), and wet slough grasses (e.g., Panicum virgatum and Bromus inermis). Figure 3.1 illustrates the gentile topographic relief present at the study site with elevation increasing westward from 589.3 to 592.0 m.a.s.l..

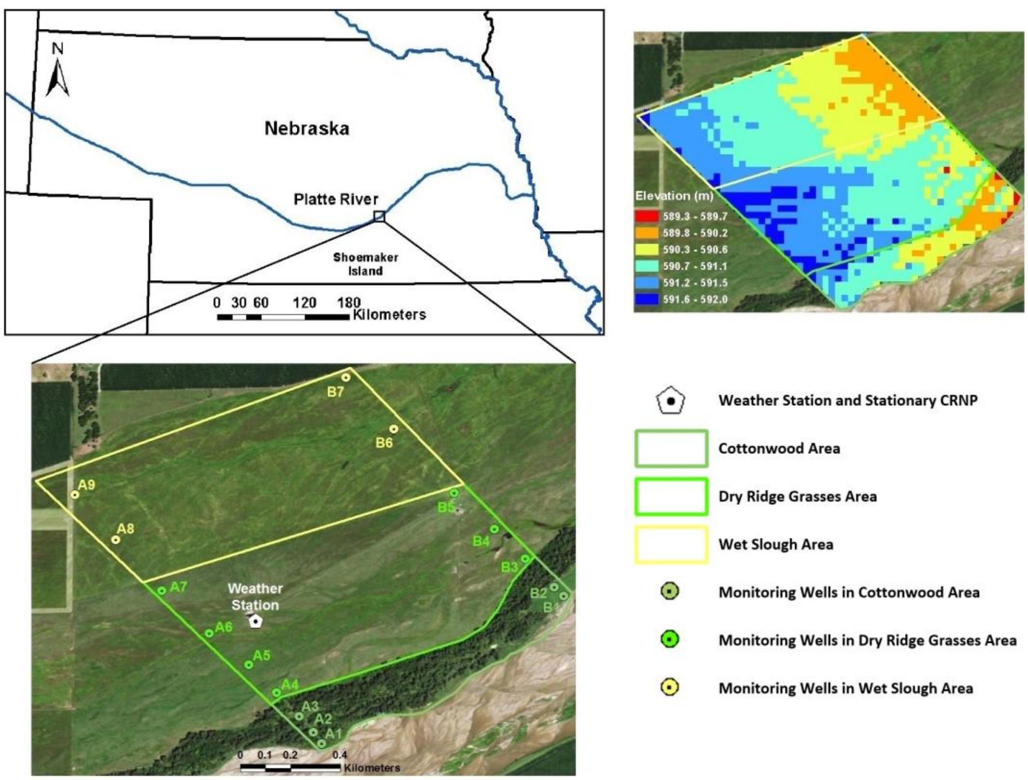

Figure 3.1. Study site (Shoemaker Island) located in the Platte River basin in central Nebraska, USA.

The Alda 3W station (established in 1995) is located in the dry ridge grass area, measures hourly global irradiance, air temperature, relative humidity, wind speed, and precipitation (Figure 3.1). Weather data (2013-2016) at the Alda 3W station were retrieved from the High Plains Regional Climate Center (HPRCC) (https://hprcc.unl.edu/). Hourly and daily reference evapotranspiration (ET_r) were computed for the tall (alfalfa) reference crop using the ASCE standardized Penman-Monteith equation (Allen et al., 2005b). The site also contained 16 shallow monitoring wells installed along two parallel transects (~1200 m in length). Neighboring monitoring wells had separation distances ranging between 5 and 300 m within each transect (Figure 3.1). Hourly water table elevations have been recorded at each monitoring well since June 1, 2013 using vented pressure transducers by Level TROLL 500 (In-Situ Inc., Fort Collins, Colorado, USA), which do not require barometric pressure correction (Yue et al., 2016). A stationary cosmic-ray neutron probe (CRNP) (model CRS 2000/B, HydroInnova LLC, Albuquerque, NM, USA) was installed next to the Alda 3W station (Figure 3.1) on October 7, 2014. The CRNP measures hourly moderated neutron counts, which are converted into near surface SWC (Zreda et al., 2008, 2012). Lastly, a mobile CRNP capable of 1-minute level moderated neutron counts (Franz et al. 2015) was used to make spatial SWC maps of the study area on select sampling dates.

3.4 Methods

In order to achieve the main objective of this study, we combined remote sensing, proximal sensing, and in-situ sensors to explore the connections between ET_a, SWC, and DTWT. Daily ET_a was estimated at the study site using the METRIC model with Landsat

8 images during 4 growing seasons (2013-2016). Spatial SWC maps were made using roving CRNP surveys from October 2014 through November 2015 (see Table 3.1 for survey dates). Groundwater data from 16 monitoring wells were used to construct DTWT maps (2013-2016) for the study site using Simple Kriging (SK) interpolation method. In addition, the normalized difference vegetation index (NDVI) was calculated from Landsat 8 images for the 4 growing seasons (2013-2016). Based on the boundaries of the three land cover classes, the spatial average value of each variable (ET_a, SWC, DTWT, and NDVI) was extracted from each dataset for each land cover class on the days whenever the ET_a products were available, and statistical relationships between ET_a and state variables were explored. Lastly, following the estimates from simple statistical models using NDVI and SWC, daily and growing season ET_a was calculated for the study area, and the results were compared with daily and growing season METRIC ET_a interpolated by the cubic spline method detailed in Allen et al., (2005a). The following sections provide further details on the methods used in this study.

Table 3.1. Roving CRNP survey dates at the study site.

Survey Number	**Date**
1	2014/11/21
2	2014/12/05
3	2015/05/12
4	2015/05/23
5	2015/07/21
6	2015/07/24
7	2015/08/13
8	2015/08/31
9	2015/09/03
10	2015/09/13

3.4.1 Spatiotemporal estimation of ET_a using METRIC

METRIC is a satellite-based image-processing model that estimates ET_a as a residual of a surface energy balance (Allen et al., 2007). METRIC uses the principles and techniques originated in the Surface Energy Balance Algorithms for Land (SEBAL), a widely used ET_a estimation model, developed by Bastiaanssen and others (Bastiaanssen, 1995; Bastiaanssen et al., 1998). METRIC uses weather-based ET_r to establish energy balance conditions at a “cold” pixel, which is a primary difference between METRIC and SEBAL. In contrast, SEBAL assumes all available energy is converted to evaporation at a temperature similar to that of a local water body for the “cold” condition of the image (Allen et al., 2007). In both METRIC and SEBAL methods energy consumed by ET_a is calculated as the residual of the surface energy equation:

$$LE = R_n - G - H \tag{1}$$

where LE is the latent heat energy (W/m^2) consumed by ET_a; R_n is the net radiation (W/m^2); G is the ground heat flux (W/m^2) conducted into the ground; and H is the sensible heat flux (W/m^2) convected into the air. Satellite-measured narrow-band reflectance and surface temperature are used to compute R_n. Ground heat flux is derived from R_n, surface temperature, and vegetation indices. Sensible heat flux is estimated from surface roughness, surface temperature ranges, and wind speed using buoyancy correction. Finally, LE is calculated as the residual of the Eq. (1) (see Allen et al., 2007 for more detailed information). LE is estimated at the exact time of the satellite overpass for each pixel. ET_a is then calculated by dividing LE by latent heat of vaporization:

$$\mathrm{ET_{inst}} = 3600\,\frac{\mathrm{LE}}{\lambda\rho_w} \qquad (2)$$

where ET_{inst} is the instantaneous ET (mm h^{-1}); 3600 converts seconds to hours; ρ_w is the density of water (~1000 kg m^{-3}); and λ is the latent heat of vaporization (J kg^{-1}) that can be computed using T_s, which is the surface temperature (K):

$$\lambda = [2.501 - 0.00236(T_s - 273.15)] \times 10^6 \qquad (3)$$

The reference ET fraction (ET_rF) for each pixel is calculated as the ratio of the computed ET_{inst} from each pixel to the hourly ET_r:

$$\mathrm{ET_rF} = \frac{\mathrm{ET_{inst}}}{\mathrm{ET_r}} \qquad (4)$$

We note that ET_rF is very similar to the well-known crop coefficient (K_c), and is used to extrapolate ET_a from the image time to periods of 24 hours or longer (Allen et al., 2007). Lastly, in order to calculate the daily ET_a over 24 hours, ET_rF values for each individual pixel were multiplied by the daily ET_r values computed from the weather data, assuming consistency between ET_rF at overpass time and ET_rF for the 24-hour period (Allen et al., 2007):

$$\mathrm{ET_a} = \mathrm{ET_rF} \times \mathrm{ET_r} \qquad (5)$$

Further technical details on SEBAL and METRIC can be found elsewhere (e.g., Allen et al., 2011, 2005a, 2007; Bastiaanssen et al., 2005; Bastiaanssen, 1995; Bastiaanssen et al., 1998; Irmak et al., 2012).

In this study, the METRIC model was applied based to Landsat 8 images (30 m spatial resolution) to determine the spatial ET_a across the study area. However, due to cloudiness conditions, we were not able to use all available Landsat 8 images for the study site. Between 2013 and 2016, we used 25 Landsat 8 images that contained zero percent cloudiness over the study area. A summary of Landsat 8 images used in the study is given in Table 3.2. The results of the METRIC model are presented in sections 3.1 and 3.2.

Table 3.2. Landsat 8 images used in this study with their Path and Row.

Date	**Path**	**Row**	**Date**	**Path**	**Row**
2013/06/10	29	32	2015/03/12	29	32
2013/06/26	29	32	2015/04/29	29	32
2013/07/03	30	32	2015/06/16	29	32
2013/07/12	29	32	2015/07/18	29	32
2013/08/20	30	32	2015/08/03	29	32
2013/08/29	29	32	2015/09/04	29	32
2013/09/21	30	32	2016/06/02	29	32
2013/10/07	30	32	2016/06/18	29	32
2014/03/09	29	32	2016/07/20	29	32
2014/06/13	29	32	2016/08/21	29	32
2014/07/15	29	32	2016/10/08	29	32
2014/09/17	29	32	2016/10/24	29	32
2014/10/03	29	32			

3.4.2 Spatiotemporal observations of DTWT using monitoring well data

Hourly groundwater level data obtained from 16 monitoring wells (Figure 3.1), during 4 growing seasons (2013-2016), were used to observe DTWT fluctuations at different locations across the study area. A SK method has been shown to be an accurate method for DTWT spatial interpolations (Sun et al., 2009; Zimmerman et al., 1999). Therefore, in this study, the SK method was used to produce DTWT maps for days when

ET_a maps were available from the METRIC model (see Table 3.2 for dates). The DTWT maps are summarized in section 3.3.

3.4.3 Spatiotemporal estimates of SWC using the stationary and mobile CRNP

Ten mobile CRNP surveys were carried out at the site to estimate SWC from October 2014 through November 2015. The roving CRNP system was mounted to an all-terrain vehicle driven at the speeds of 8-15 km hr^{-1} at ~15-20 m spacing for each reading of the moderated neutron counts. It required about 180 minutes to complete the survey of the study area. The mobile CRNP records epithermal neutron intensity integrated over one-minute counting intervals (Franz et al., 2015). The change in epithermal neutron intensity is inversely correlated to the mass of hydrogen in the measurement volume (Zreda et al., 2012). The authors note that SWC changes are by far the largest contributor to the changes in hydrogen mass (McJannet et al., 2014). Numerous validation studies across the globe (Bogena et al., 2013; Franz et al., 2012, 2016; Hawdon et al., 2014) have shown the CRNP to have area-average measurement uncertainty of less than 0.03 cm^3cm^{-3}, within the top 0.3 m of soil profile, validated against a variety of industry standard SWC point scale probes. The measurement volume of the CRNP is roughly a disk, with a ~250 m radius circle and penetration depths of 0.15 to 0.40 m (Köhli et al., 2015) depending on local conditions. For simplicity, a constant penetration depth of 0.3 m was assumed for all surveys.

In order to provide a SWC map, a spatial map of neutron intensity was first estimated, and then a calibration function was applied following Franz et al., (2015). The neutron intensity map was created in two steps. First, a drop-in-the-bucket preprocessing step was applied, where a dense grid was generated (here 20 by 20 m) and all raw data points were found within a certain radius (here 50 m). Then, the average of all raw data found within the search radius was assigned to the grid center. This oversampling approach is necessary for sharpening the image quality and is a common strategy used in remote sensing analyses (see Chan et al., 2014) when overlapping area-average observations are collected, like the CRNP in this study. Next, an inverse-distance-weighted approach was used on the resampled 20 m grid to produce a neutron intensity estimate. The gridded neutron intensity estimate was converted to SWC following Franz et al., (2015). The authors refer the readers to the rapidly growing CRNP literature (see Zreda et al., 2012) instead of providing full details of the methodology here for the purpose of brevity. The hourly stationary CRNP data were processed in the same manner. Finally, spatial SWC maps were produced on the same days as the METRIC ET_a dates by merging the stationary time series and spatial maps using linear regression for each grid location following (Franz et al., 2015).

3.5 Results

Figure 3.2 provides a summary of time series for daily rainfall, ET_r, DTWT, and stationary CRNP-estimated SWC between 2013 and 2016. In addition, spatial averages of ET_a, DTWT, and SWC are also provided for each of the three land covers. Individual maps for each state variable and flux are discussed in the following sections. First, we will explore the relationships between ET_a, DTWT, and SWC. Only the 2016 growing season maps are provided here for conciseness (Figures 3.3-3.6); whereas, the maps for 2013-2015 are provided in the supplemental material, and their data are used in the following analyses. Lastly, the METRIC model produces ET_rF (Kc) maps; therefore, spatial relationships among ET_rF and DTWT and SWC are also explored.

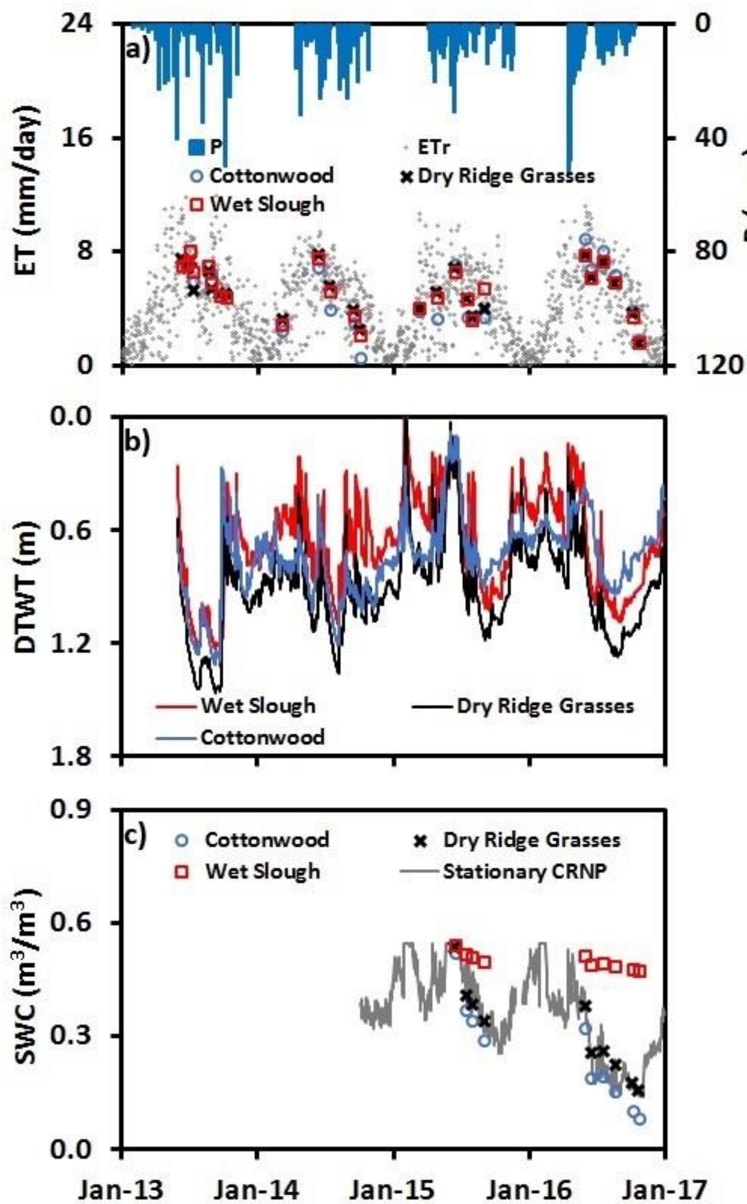

Figure 3.2. a) Daily P, ET_r, and average daily ET_a in satellite overpass days in different land covers, b) average depth to the water table (DTWT), based on groundwater observation data, in different land covers, and c) continuous SWC measured by stationary CRNP and average SWC in different land covers measured by CRNP rover.

3.5.1 Spatiotemporal observations of ET_rF

The METRIC model was applied to 25 Landsat 8 images during 4 growing seasons (2013-2016). The spatial ET_rF values were sampled at different locations across the study area during production of ET_a maps. Figure 3.3 illustrates ET_rF maps of the study site in 2016, produced by the METRIC method. Generally, ET_rF ranges from 0 to about 1.1, where 1.0 indicates equivalency with the tall (alfalfa) reference ET. Figure 3.3 also displays the boundaries of the 3 distinct vegetation types as shown in Figure 3.1. Based on the processed images, cottonwood areas tended to have higher ET_rF values compared to the other two land covers, especially the dry ridge grass area in the early (March-April-May (MAM)) and late growing season (September-October (SO)). However, in the mid growing season (JJA), the grass areas usually had higher ET_rF values. We note that the pattern of ET_rF was highly variable between and within seasons, subject to meteorological conditions and moisture availability in the soil and shallow alluvial aquifer. Section 4.1 explores these correlations explicitly.

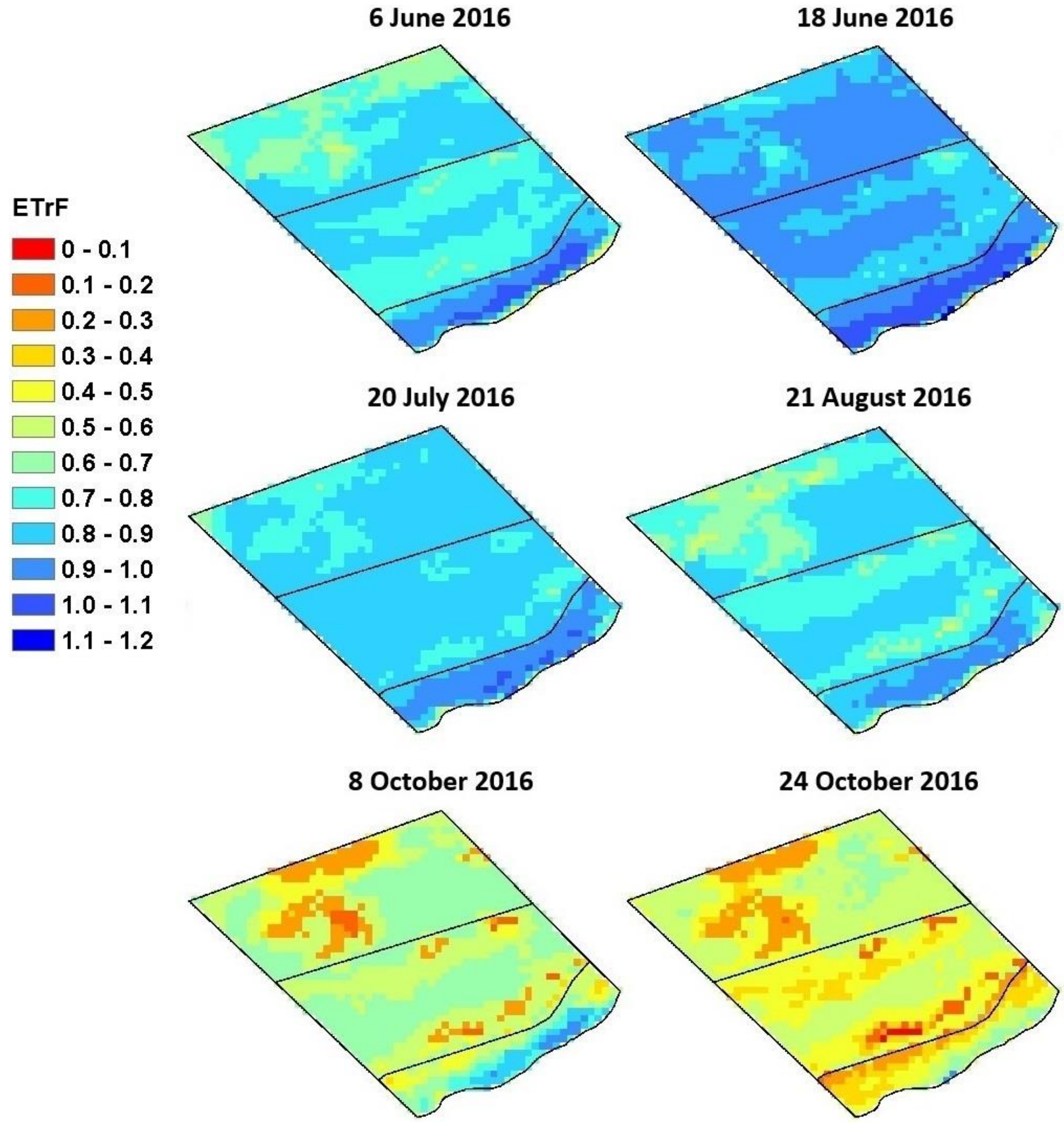

Figure 3.3. Sample ET_rF maps of study site in 2016, produced by METRIC method (rest of ET_rF maps can be found in supplemental materials).

3.5.2 Spatiotemporal observations of ET_a

Figure 3.4 illustrates ET_a maps of the study site in 2016 generated using the METRIC method. Because ET_rF maps were used to make the ET_a maps, similar spatiotemporal patterns as the ones of ET_rF are shown in the ET_a maps. Figure 3.2a illustrates the spatially averaged ET_a rate values for different land covers with minimal differences in the average ET_a amongst those land covers. Figure 3.2a also illustrates the daily ET_r values calculated from the ASCE standardized Penman-Monteith equation. We note that average ET_a values for the different land covers were always less than ET_r, indicating that water limitations existed across the study site during the study period.

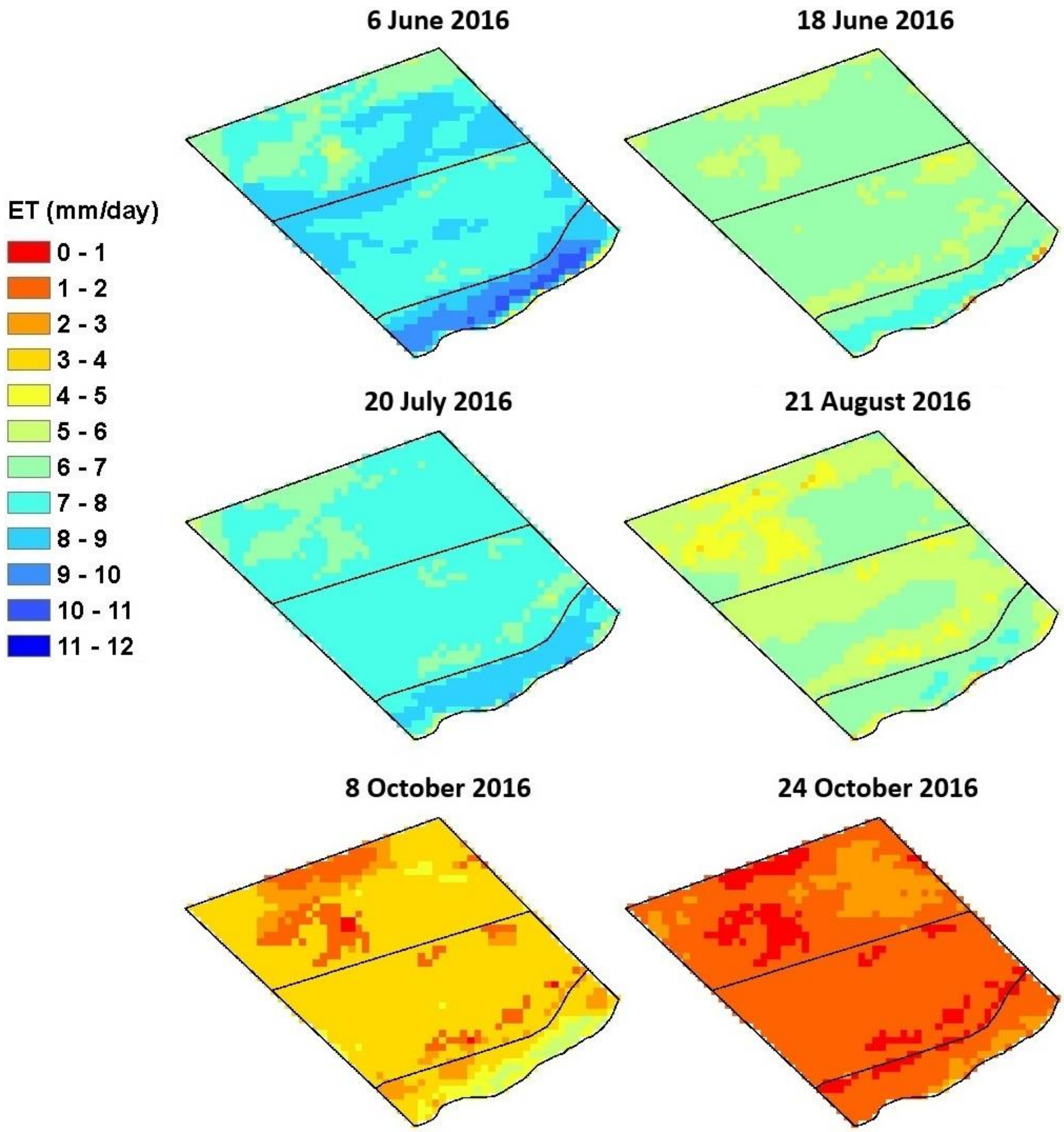

Figure 3.4. Sample ET_a maps of study site in 2016, produced by METRIC method (rest of ET_a maps can be found in supplemental materials).

3.5.3 Spatiotemporal observations of DTWT

Figure 3.5 presents the 2016 DTWT maps corresponding to the ET_a observation dates. Figure 3.2b illustrates the average DTWT values for different land covers, indicating that DTWT was deepest in the dry ridge grass area, which tended to have slightly higher land elevation (Figure 3.1). The wet slough area had the shallowest DTWT during the observation period. Visual observations of the DTWT maps in Figure 3.5 indicate no clear spatial patterns. We suspect this may be due to the limited number of observation wells and spatial interpolation technique, as well as heterogeneous vegetation conditions.

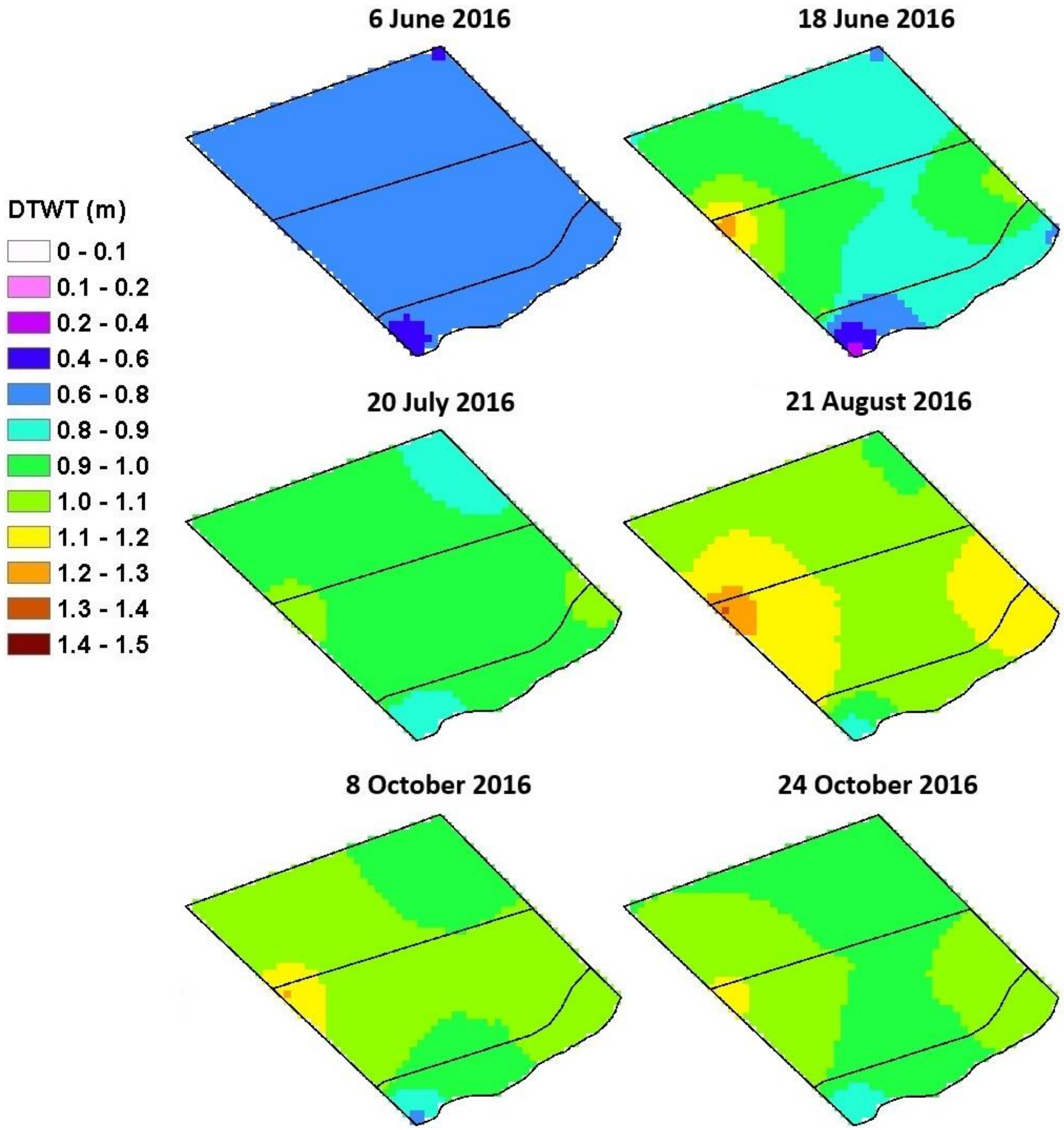

Figure 3.5. Sample DTWT maps of study site in 2016 based on groundwater observations (rest of DTWT maps can be found in supplemental materials).

3.5.4 Spatiotemporal observations of SWC

The hourly moderated neutron counts from the stationary CRNP measurements were converted into SWC (Figure 3.2c) following standard correction procedures and calibration methods (Zreda et al., 2012). Figure 3.6 illustrates the 2016 SWC maps interpolated from the roving and stationary CRNP. In order to provide SWC maps on the same days as ET_a, a linear regression procedure was used to compare each 20 m grid location from the rover surveys to the fixed CRNP values following Franz et al., (2015).

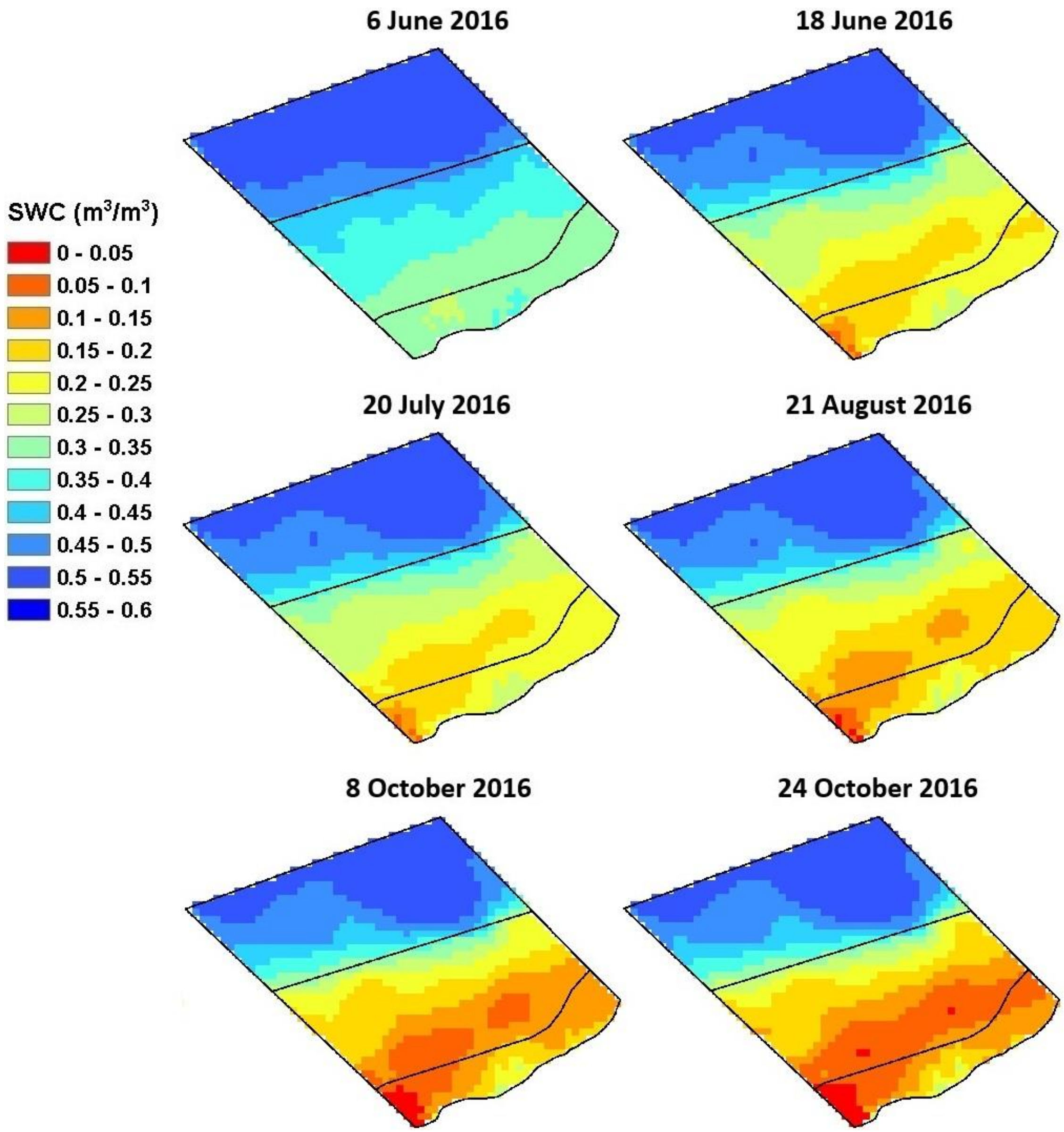

Figure 3.6. Sample SWC maps of study site in 2016 based on CRNP SWC data (rest of SWC maps can be found in supplemental materials).

Figure 3.7a illustrates the spatial distribution of correlation coefficient (R^2) values. Figure 3.7b shows the cumulative distribution function (CDF) of R^2 and associated p values for each 20 m grid location. Figure 3.7b illustrates that approximately 60% of grid cells have $R^2 > 0.50$ and 65% of grid cells had p values < 0.05. The area with the poorest performance of the regression was in the wet slough area, where there were minimal temporal changes in the SWC during the rover surveys (i.e., they were always wet). The SWC maps in Figure 3.6 clearly illustrate that SWC increased from the southern to northern part of the study area, meaning that the wet slough and dry ridge grass areas had higher SWC values compared to the cottonwood area during all the rover CRNP surveys. The SWC patterns in general followed the elevation contours at the site (Figure 3.1). Figure 3.2c also illustrates the average SWC values for each land cover on the days of the Landsat overpass dates and stationary CRNP SWC. The stationary CRNP SWC data were closest to the dry ridge grass SWC. The spatial average of SWC also indicates that the cottonwood area had the lowest SWC values and the wet slough had the highest SWC values.

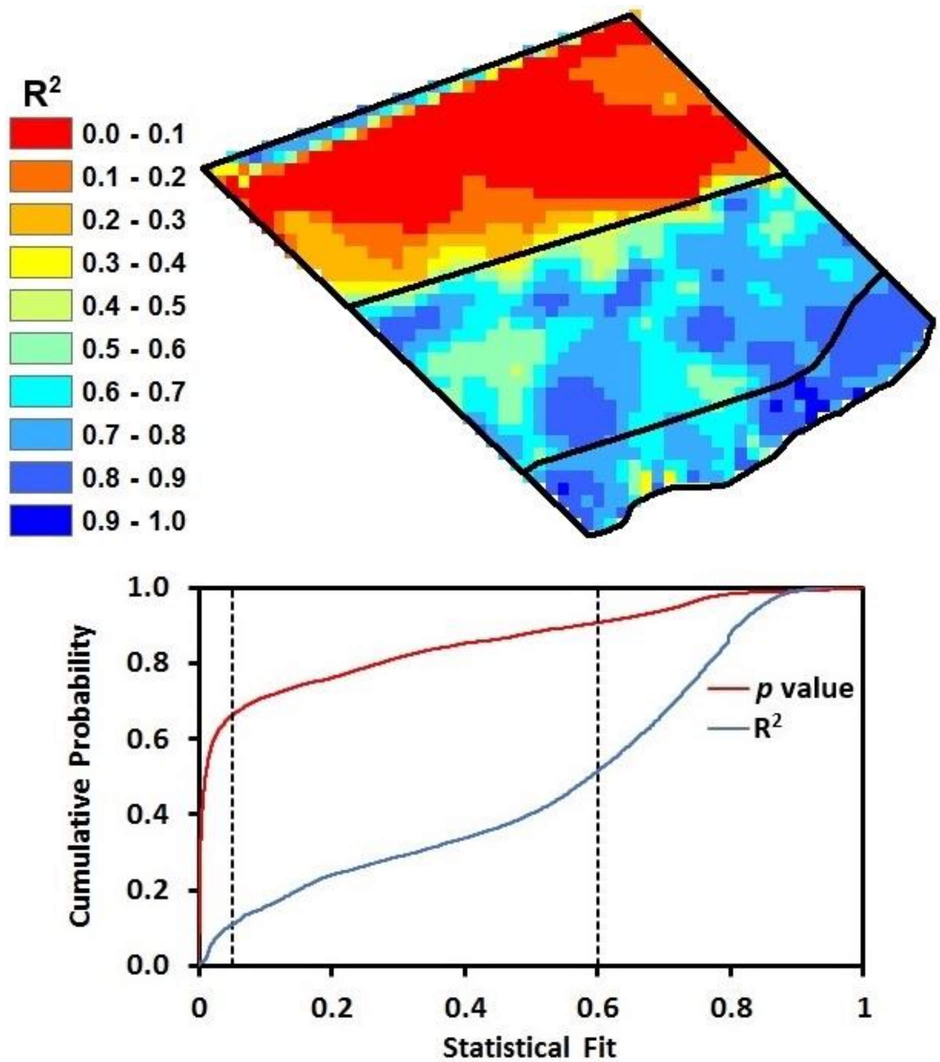

Figure 3.7. a) Spatial distribution of linear R^2 values using the rover SWC survey value and fixed SWC CRNP value for a 20 m grid. b) CDF of grid R^2 and p values from linear regression.

3.6 Discussion

The METRIC method was applied to generate a total of 25 daily ET_a maps based on available Landsat images having no cloud coverage over the study area during 4 growing seasons (2013-2016). Ten rover CRNP SWC surveys, from October 2014 through November 2015 (Table 3.1), were conducted. Statistically combining the rover surveys with the stationary CRNP data allowed us to generate daily SWC maps. Daily DTWT maps were generated during the 4 growing seasons (2013-2016) from the 16 well locations. The paucity of available Landsat data and CRNP surveys underscores the challenge of using spatially exhaustive but temporally limited data to construct a continuum of ET_a. With respect to the Landsat satellite, the 16-day overpass and cloud contamination issues can greatly reduce the number of images to use in the temporal interpolation. Likewise, the roving CRNP is often limited by field access and labor availability. The DTWT spatial interpolation method is limited by the localized conditions of the well data and the number of available wells. Therefore, strategies to combine infrequent spatial data and spatially limited temporal point data remain an important challenge in order to generate spatiotemporal data that can be utilized by models. In order to overcome this challenge, the next sections evaluate the use of continuous sensor data with simple linear regression models to make spatiotemporal predictions for ET_a. Lastly seasonal estimations regarding land cover average ET_a are discussed.

3.6.1 Relationships between ET_a and ET_rF with SWC, DTWT, and NDVI

Figures 3.8 to 3.10 illustrate the linear correlations of ET_a and ET_rF with SWC, DTWT, and NDVI averaged over each of the three land cover types. It is worth mentioning that, while the correlation of ET_a and ET_rF with DTWT and NDVI were examined during 4 growing seasons (2013-2016), the correlation of ET_a and ET_rF with SWC were explored just during 2 growing seasons (2015-2016) due to the lack of SWC data.

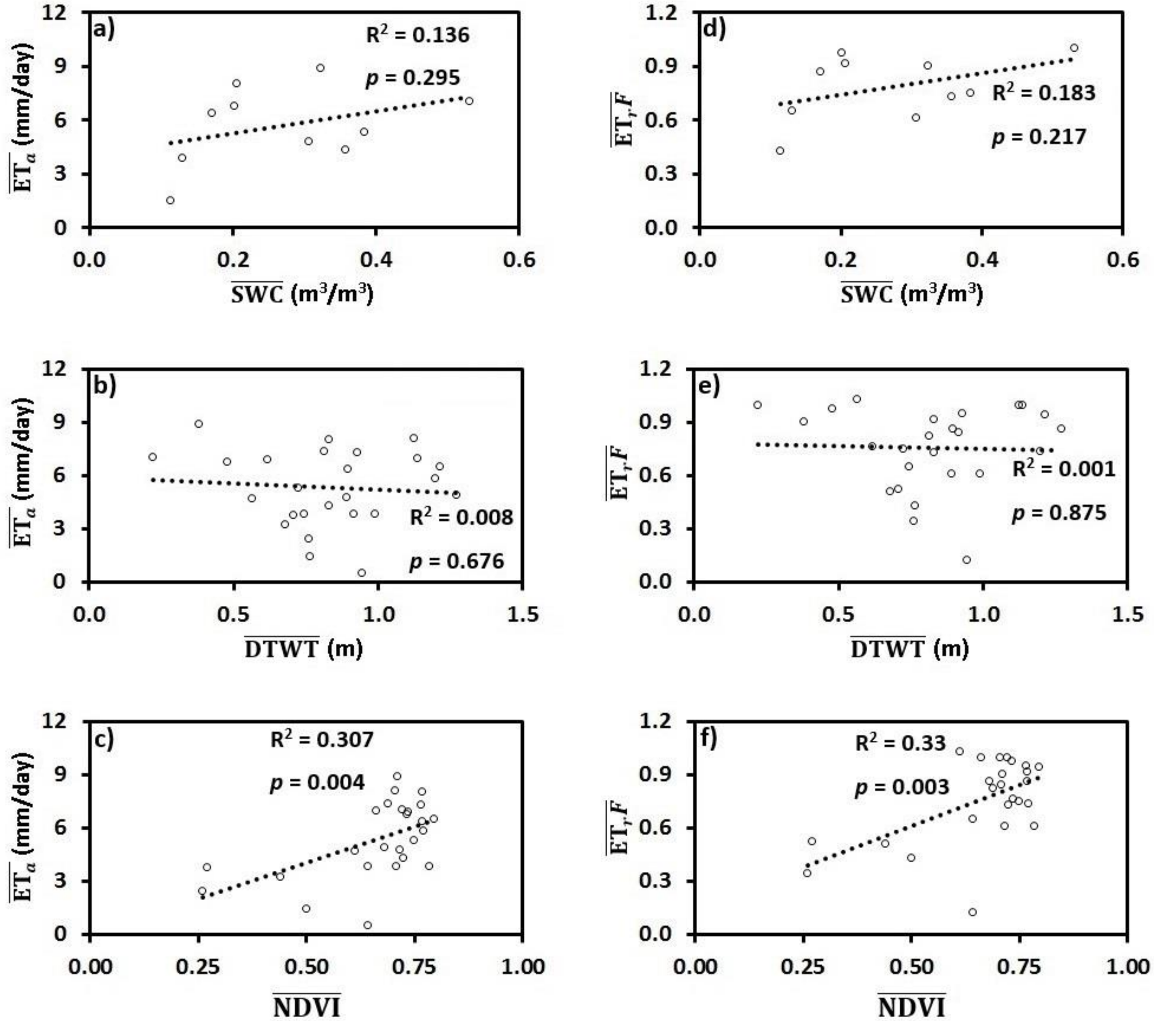

Figure 3.8. a) The relationship between ET_a (mm/day) and SWC (m^3/m^3), b) relationship between ET_a (mm/day) and DTWT (m), c) relationship between ET_a (mm/day) and NDVI, d) relationship between ET_rF and SWC (m^3/m^3), e) relationship between ET_rF and DTWT (m), and f) relationship between ET_rF and NDVI in the cottonwood area at the study site.

In general, both ET_a and ET_rF had stronger linear correlations with SWC than with DTWT and NDVI, specifically in the wet slough area (ET_a, R^2=0.393, p=0.052) and dry ridge grass (ET_a, R^2=0.323, p=0.086) area as compared to the cottonwood area (R^2=0.136, p=0.295). This confirms the limiting control and importance of SWC on ET_a in semi-arid areas with shallow rooted vegetation. A much weaker relationship can also be seen in the cottonwood area. The results show no relationships between ET_a and ET_rF and DTWT in any of the three land covers.

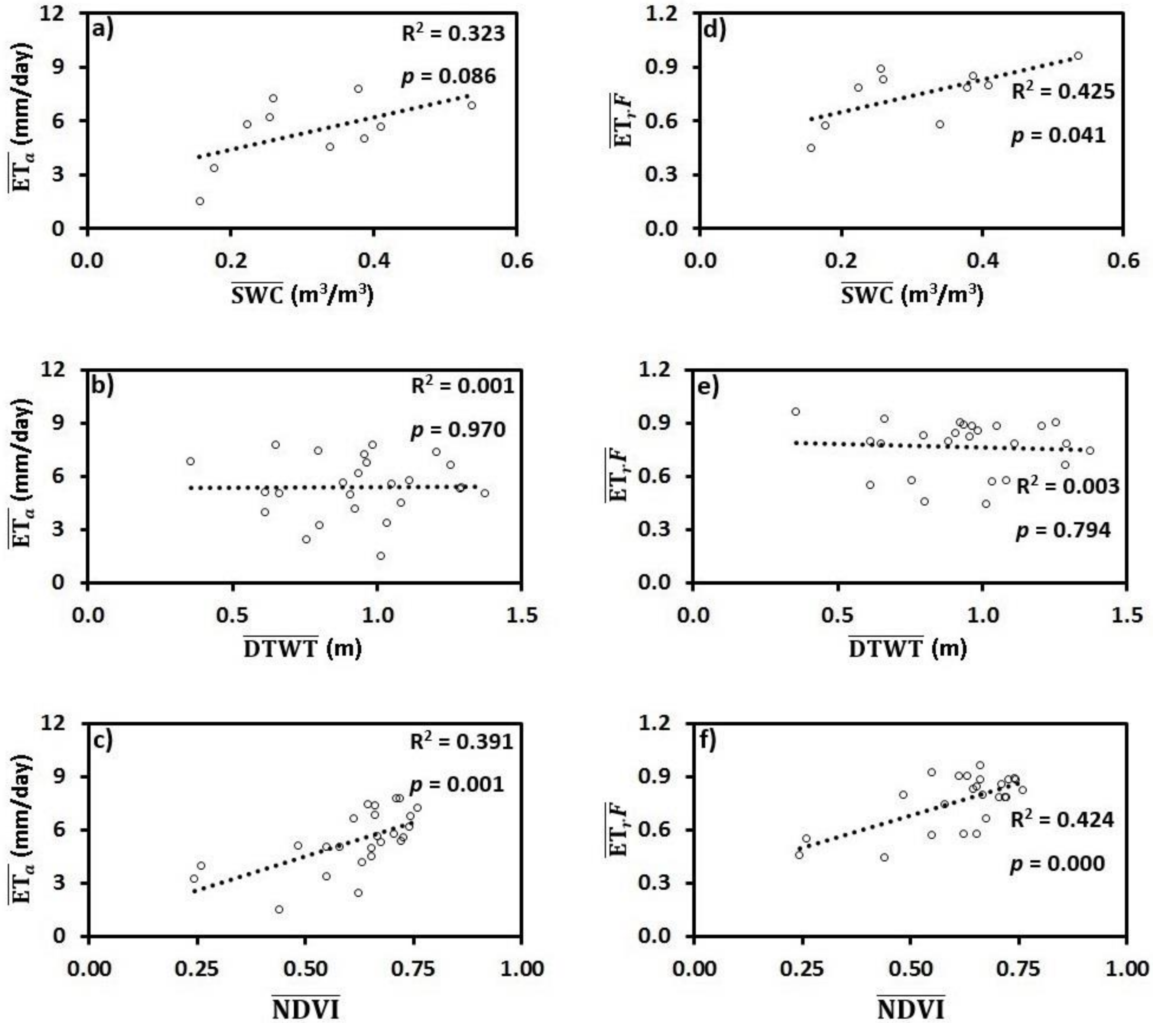

Figure 3.9. a) The relationship between ET_a (mm/day) and SWC (m^3/m^3), b) relationship between ET_a (mm/day) and DTWT (m), c) relationship between ET_a (mm/day) and NDVI, d) relationship between ET_rF and SWC (m^3/m^3), e) relationship between ET_rF and DTWT (m), and f) relationship between ET_rF and NDVI in the dry ridge grasses area at the study site.

We note the data limitations of DTWT and spatial resolution differences make this analysis and conclusion challenging here and in surface-groundwater studies in general. The analysis between ET_a and ET_rF versus NDVI in all the land covers show strong correlations, specifically between ET_rF and NDVI (R^2>0.33, p<0.003). Lastly we note that ET_a may be nonlinearly dependent on SWC and DTWT. Therefore, the use of spatial averages may mask the nonlinearity, causing the low R^2 values.

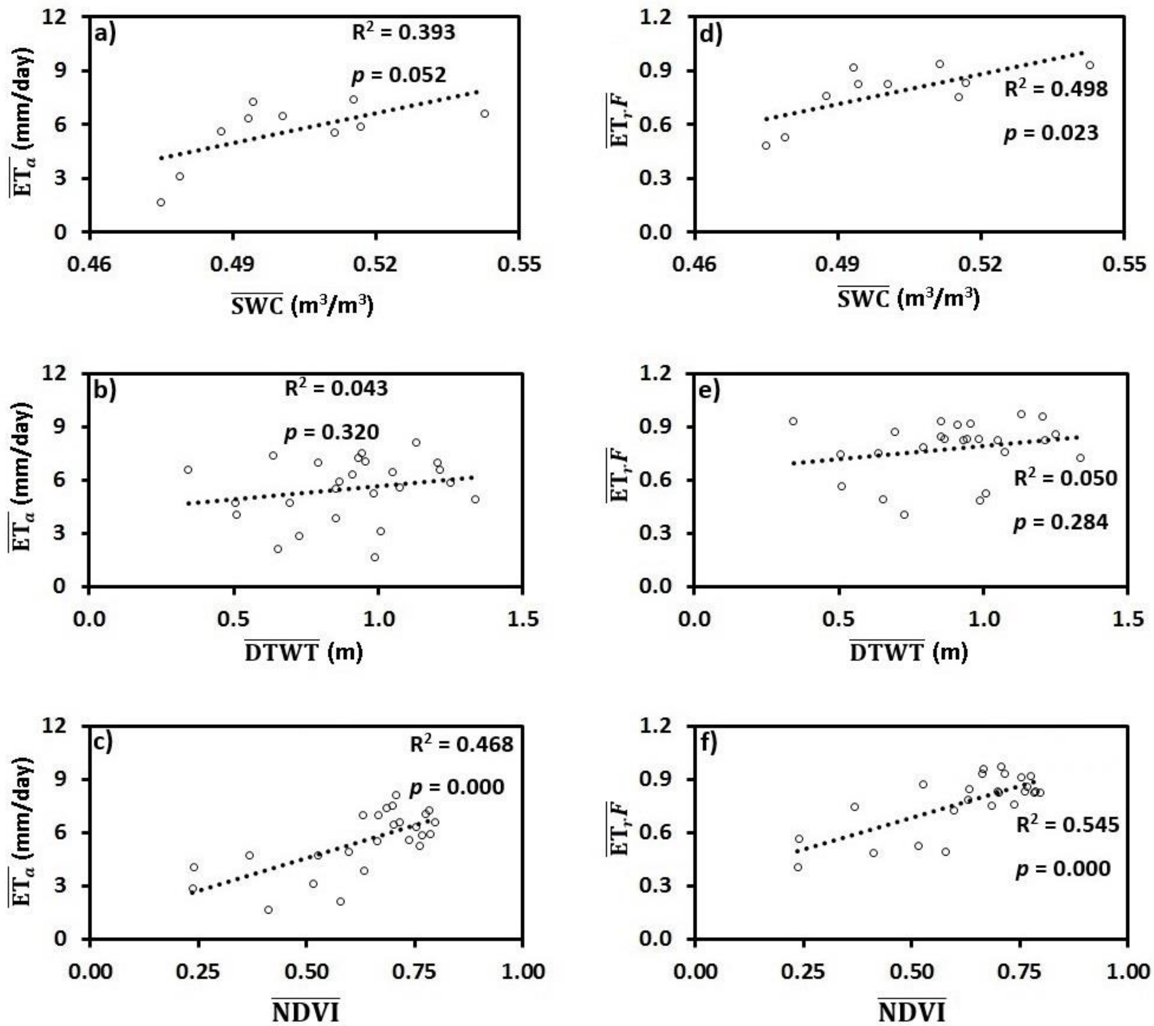

Figure 3.10. a) The relationship between ET_a (mm/day) and SWC (m^3/m^3), b) relationship between ET_a (mm/day) and DTWT (m), c) relationship between ET_a (mm/day) and NDVI, d) relationship between ET_rF and SWC (m^3/m^3), e) relationship between ET_rF and DTWT (m), and f) relationship between ET_rF and NDVI in the wet slough area at the study site.

3.6.2 Estimation of area average daily and seasonal ET_a

For illustrative and comparative purposes, a simple multivariate linear regression model between daily CRNP SWC, Landsat NDVI, and weather station ET_r, was used to estimate daily growing season ET_a for 2015 and 2016 averaged over the study area. The statistical model of ET_a was compared to the more commonly used cubic spline method for estimating daily and seasonal ET_a (Allen et al., 2005a), see Figure 3.11. Given the 16-day overpass time of Landsat 8, daily ET_a time integration of observations are uncertain and subject to local conditions that may further limit ET_a. The statistical model was estimated using the 2015 METRIC data resulting in $ET_rF = 0.575*NDVI + 1.088*SWC - 0.0287$, $R^2 = 0.98$, $p = 0$ and RMSE = 0.238. The model was then validated against the 2016 METRIC data resulting in $R^2 = 0.88$, $p = 0$ and RMSE = 1.077. Figures 3.11a, c, d indicate excellent daily and seasonal ET_a agreement in 2015, which was a wet year as shown by Figure 3.2c. However, the drier SWC conditions of 2016 indicate different daily and seasonal ET_a, Figures 3.11b, c, and d. Seasonal ET_a estimated with the statistical model was about 20% lower (720 vs 580 mm) as compared to the ET_a from cubic spline method in 2016. Unfortunately, no independent surface energy balance methods were available for the study area to confirm the predicted reduction in 2016 seasonal ET_a. We note that due to the weak correlation between DTWT and ET_a, DTWT was not included in the multi-linear regression equation. We also note that deep SWC changes below the sensitivity of the CRNP (~>0.4 m) were not accounted for in the statistical model. Of particular importance, DTWT observations between 2015 and 2016 (Figure 3.2b) indicate further drawdown in 2016 accounting for some of the water used by the vegetation and supporting the higher seasonal ET_a values from METRIC and the cubic spline time integration. Future work at sites with direct surface energy balance observations (i.e. eddy covariance) should better quantify whether these differences in seasonal ET_a noted between the cubic spline method using METRIC data and observations are real and which ones are closest to reality. The study presented here was a first attempt to illustrate the connections and dependence between remotely sensed fluxes and proximal sensing/in-situ observations of state variables. The main point is that local SWC conditions on the ground between 16-day Landsat overpasses may lead to significant differences in daily and seasonal ET_a estimates of riparian study sites.

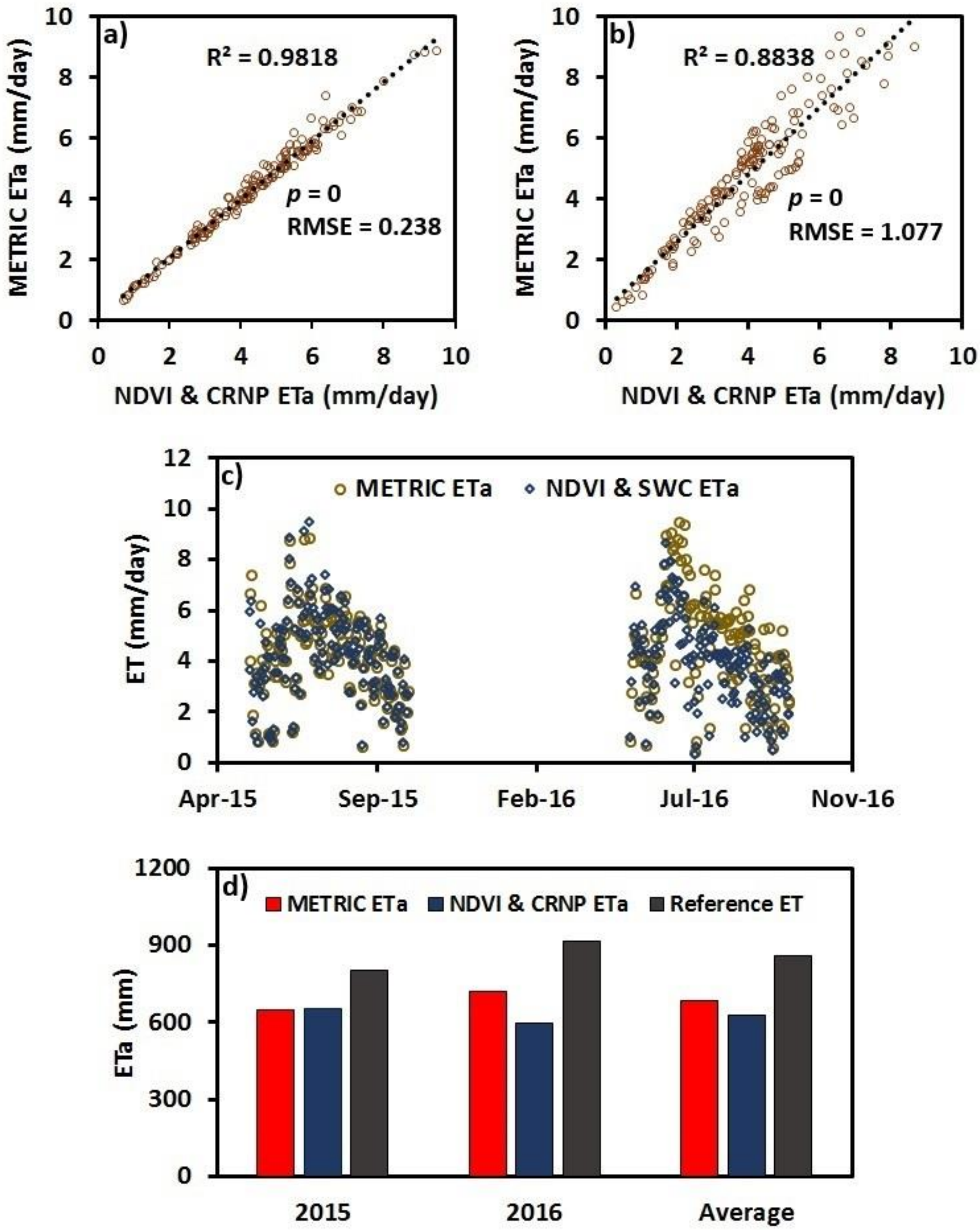

Figure 3.11. Daily and seasonal ET_a estimates of the study site during calibration growing seasons a) (2015) and b) validation growing seasons (2016) using the standard METRIC interpolation method vs NDVI & CRNP-SWC statistical model. c) Daily ET_a and d) seasonal values are also compared.

3.7 Conclusions

Calibration, validation, and evaluation of complex physically based models with surface and groundwater connections require rich spatiotemporal datasets of water fluxes and state variables. This paper attempts to generate novel spatiotemporal datasets of ET_a, SWC, and DTWT using a combination of remote (METRIC model) and proximal sensing methods (fixed and roving CRNP) in a well instrumented riparian study site in central Nebraska. Comparison of the datasets reveal that SWC and ET_a were linearly correlated for shallow rooted vegetation at the study site. The correlation between DTWT and ET_a was weak but may be limited by the localized conditions of the groundwater observations. Lastly a simple statistical model of daily ET_a vs. the calculated daily ET_a from the commonly used cubic spline method indicate similar seasonal ET_a values in the wet conditions of 2015. Comparison of the two temporal interpolation methods in the drier conditions of 2016 indicate a 20% difference in seasonal ET_a. The difference underscores the need for better accounting for local state variable changes between the 16-day overpass of the Landsat 8 satellite.

3.8 Acknowledgments

The material for this work is based in part on work supported by the Platte River Recovery Implementation Program. The groundwater level data analyzed in this study can be obtained from the Platte River Recovery Implementation Program (grieblings@headwaterscorp.com) and the meteorological data can be accessed from the High Plains Regional Climate Center at http://www.hprcc.unl.edu/. TEF would also like to acknowledge the financial support of the USDA National Institute of Food and Agriculture, Hatch project #1009760. The authors would also like to thank Scott Griebling for his help with field work data processing.

3.9 References

Acharya, S., Mylavarapu, R., & Jawitz, J. (2014). Evapotranspiration Estimation from Diurnal Water Table Fluctuations: Implementing Drainable and Fillable Porosity in the White Method. Vadose Zone Journal, 13(9). https://doi.org/10.2136/vzj2014.04.0048

Allen, R., Irmak, A., Trezza, R., Hendrickx, J. M. H., Bastiaanssen, W., & Kjaersgaard, J. (2011). Satellite-based ET estimation in agriculture using SEBAL and METRIC. Hydrological Processes, 25(26), 4011–4027. https://doi.org/10.1002/hyp.8408

Allen, R. G., Tasumi, M., & Trezza, R. (2007). Satellite-Based Energy Balance for Mapping Evapotranspiration with Internalized Calibration (METRIC)—Model. Journal of Irrigation and Drainage Engineering, 133(4), 380–394. https://doi.org/10.1061/(ASCE)0733-9437(2007)133:4(380)

Allen, R. G., Tasumi, M., Trezza, R., & Kjaersgaard, J. (2005). METRIC: mapping evapotranspiration at high resolution–applications manual for Landsat satellite imagery. University of Idaho, 130.

Allen, R. G., Walter, I. A., Elliott, R. L., Howell, T. A., Itenfisu, D., Jensen, M. E., & Snyder, R. L. (2005). The ASCE Standardized Reference Evapotranspiration Equation. ASCE Publications.

Bastiaanssen, Noordman, Pelgrum, Davids, Thoreson, & Allen. (2005). SEBAL Model with Remotely Sensed Data to Improve Water-Resources Management under Actual Field Conditions. Journal of Irrigation and Drainage Engineering, 131(1), 85–93. https://doi.org/10.1061/(ASCE)0733-9437(2005)131:1(85)

Bastiaanssen, W. G. M. (1995). Regionalization of Surface Flux Densities and Moisture Indicators in Composite Terrain: A Remote Sensing Approach Under Clear Skies in Mediterranean Climates. DLO Winand Staring Centre.

Bastiaanssen, W. G. M., Menenti, M., Feddes, R. A., & Holtslag, A. A. M. (1998). A remote sensing surface energy balance algorithm for land (SEBAL). 1. Formulation. Journal of Hydrology, 212, 198–212. https://doi.org/10.1016/S0022-1694(98)00253-4

Bogena, H. R., Huisman, J. A., Baatz, R., Hendricks Franssen, H.-J., & Vereecken, H. (2013). Accuracy of the cosmic-ray soil water content probe in humid forest ecosystems: The worst case scenario. Water Resources Research, 49(9), 5778–5791. https://doi.org/10.1002/wrcr.20463

Chan, S., Njoku, E., & Colliander, A. (2014). Soil Moisture Active Passive (SMAP) Algorithm Theoretical Basis Document Level 1C Radiometer Data Product. Jet Propulsion Laboratory California Institute of Technology Pasadena, CA.

Chen, X., & Shu, L. (2006). Groundwater evapotranspiration captured by seasonally pumped wells in river valleys. Journal of Hydrology, 318(1), 334–347. https://doi.org/10.1016/j.jhydrol.2005.06.025

Clark, M. P., Bierkens, M. F. P., Samaniego, L., Woods, R. A., Uijlenhoet, R., Bennett, K. E., … Peters-Lidard, C. D. (2017). The evolution of process-based hydrologic models: historical challenges and the collective quest for physical realism. Hydrol. Earth Syst. Sci., 21(7), 3427–3440. https://doi.org/10.5194/hess-21-3427-2017

Foolad, F., Franz, T. E., Wang, T., Gibson, J., Kilic, A., Allen, R. G., & Suyker, A. (2017). Feasibility analysis of using inverse modeling for estimating field-scale evapotranspiration in maize and soybean fields from soil water content monitoring networks. Hydrol. Earth Syst. Sci., 21(2), 1263–1277. https://doi.org/10.5194/hess-21-1263-2017

Franz, T. E., Wahbi, A., Vreugdenhil, M., Weltin, G., Heng, L., Oismueller, M., … Desilets, D. (2016). Using Cosmic-Ray Neutron Probes to Monitor Landscape Scale Soil Water Content in Mixed Land Use Agricultural Systems. Applied and Environmental Soil Science. https://doi.org/10.1155/2016/4323742

Franz, T. E., Wang, T., Avery, W., Finkenbiner, C., & Brocca, L. (2015). Combined analysis of soil moisture measurements from roving and fixed cosmic ray neutron probes for multiscale real-time monitoring. Geophysical Research Letters, 42(9), 2015GL063963. https://doi.org/10.1002/2015GL063963

Franz, T. E., Zreda, M., Rosolem, R., & Ferre, T. P. A. (2012). Field Validation of a Cosmic-Ray Neutron Sensor Using a Distributed Sensor Network. Vadose Zone Journal, 11(4). https://doi.org/10.2136/vzj2012.0046

Gribovszki, Z., Kalicz, P., Szilágyi, J., & Kucsara, M. (2008). Riparian zone evapotranspiration estimation from diurnal groundwater level fluctuations. Journal of Hydrology, 349(1), 6–17. https://doi.org/10.1016/j.jhydrol.2007.10.049

Groeneveld, D. P. (2008). Remotely-sensed groundwater evapotranspiration from alkali scrub affected by declining water table. Journal of Hydrology, 358(3), 294–303. https://doi.org/10.1016/j.jhydrol.2008.06.011

Groeneveld, D. P., Baugh, W. M., Sanderson, J. S., & Cooper, D. J. (2007). Annual groundwater evapotranspiration mapped from single satellite scenes. Journal of Hydrology, 344(1), 146–156. https://doi.org/10.1016/j.jhydrol.2007.07.002

Hawdon, A., McJannet, D., & Wallace, J. (2014). Calibration and correction procedures for cosmic-ray neutron soil moisture probes located across Australia. Water Resources Research, 50(6), 5029–5043. https://doi.org/10.1002/2013WR015138

Hays, K. B. (2003). Water use by saltcedar (Tamarix sp.) and associated vegetation on the Canadian, Colorado and Pecos Rivers in Texas (Thesis). Texas A&M University. Retrieved from http://oaktrust.library.tamu.edu/handle/1969.1/ETD-TAMU-2003-THESIS-H394

Irmak, A., Allen, R. G., Kjaersgaard, J., Huntington, J., Kamble, B., Trezza, R., & Ratcliffe, I. (2012). Operational Remote Sensing of ET and Challenges. https://doi.org/10.5772/25174

Köhli, M., Schrön, M., Zreda, M., Schmidt, U., Dietrich, P., & Zacharias, S. (2015). Footprint characteristics revised for field-scale soil moisture monitoring with cosmic-ray neutrons. Water Resources Research, 51(7), 5772–5790. https://doi.org/10.1002/2015WR017169

Kurc, S. A., & Small, E. E. (2004). Dynamics of evapotranspiration in semiarid grassland and shrubland ecosystems during the summer monsoon season, central New Mexico. Water Resources Research, 40(9), W09305. https://doi.org/10.1029/2004WR003068

Laio, F., Porporato, A., Fernandez-Illescas, C. P., & Rodriguez-Iturbe, I. (2001). Plants in water-controlled ecosystems: active role in hydrologic processes and response to water stress. Advances in Water Resources, 24(7), 745–762. https://doi.org/10.1016/S0309-1708(01)00007-0

Loheide, S. P., Butler, J. J., & Gorelick, S. M. (2005). Estimation of groundwater consumption by phreatophytes using diurnal water table fluctuations: A saturated-unsaturated flow assessment. Water Resources Research, 41(7), W07030. https://doi.org/10.1029/2005WR003942

Maxwell, R. M., & Condon, L. E. (2016). Connections between groundwater flow and transpiration partitioning. Science, 353(6297), 377–380. https://doi.org/10.1126/science.aaf7891

Maxwell, R. M., & Kollet, S. J. (2008). Interdependence of groundwater dynamics and land-energy feedbacks under climate change. Nature Geoscience; London, 1(10), 665–669. https://doi.org/http://dx.doi.org/10.1038/ngeo315

McCabe, M. F., Rodell, M., Alsdorf, D. E., Miralles, D. G., Uijlenhoet, R., Wagner, W., … Wood, E. F. (2017). The future of Earth observation in hydrology. Hydrology and Earth System Sciences; Katlenburg-Lindau, 21(7), 3879–3914. https://doi.org/http://dx.doi.org/10.5194/hess-21-3879-2017

McJannet, D., Franz, T., Hawdon, A., Boadle, D., Baker, B., Almeida, A., … Desilets, D. (2014). Field testing of the universal calibration function for determination of soil moisture with cosmic-ray neutrons. Water Resources Research, 50(6), 5235–5248. https://doi.org/10.1002/2014WR015513

Peters-Lidard, C. D., Clark, M., Samaniego, L., Verhoest, N. E. C., van Emmerik, T., Uijlenhoet, R., … Woods, R. (2017). Scaling, similarity, and the fourth paradigm for hydrology. Hydrol. Earth Syst. Sci., 21(7), 3701–3713. https://doi.org/10.5194/hess-21-3701-2017

Reynolds, J. F., Kemp, P. R., & Tenhunen, J. D. (2000). Effects of long-term rainfall variability on evapotranspiration and soil water distribution in the Chihuahuan Desert: A modeling analysis. Plant Ecology, 150(1–2), 145–159. https://doi.org/10.1023/A:1026530522612

Rodriguez-Iturbe, I., Porporato, A., Laio, F., & Ridolfi, L. (2001). Plants in water-controlled ecosystems: active role in hydrologic processes and response to water stress. Advances in Water Resources, 24(7), 695–705. https://doi.org/10.1016/S0309-1708(01)00004-5

Shuttleworth, W. J. (1991). Evaporation Models in Hydrology. In Land Surface Evaporation (pp. 93–120). Springer, New York, NY. https://doi.org/10.1007/978-1-4612-3032-8_5

Smith, C. B. (2011). Adaptive management on the central Platte River – Science, engineering, and decision analysis to assist in the recovery of four species. Journal of Environmental Management, 92(5), 1414–1419. https://doi.org/10.1016/j.jenvman.2010.10.013

Soil Survey Staff, Natural Resources Conservation Service, United States Department of Agriculture. Web Soil Survey. Available online at http://websoilsurvey.nrcs.usda.gov/. Accessed in August, 2017.

Soylu, M. E., Istanbulluoglu, E., Lenters, J. D., & Wang, T. (2011). Quantifying the impact of groundwater depth on evapotranspiration in a semi-arid grassland region. Hydrol. Earth Syst. Sci., 15(3), 787–806. https://doi.org/10.5194/hess-15-787-2011

Sun, Y., Kang, S., Li, F., & Zhang, L. (2009). Comparison of interpolation methods for depth to groundwater and its temporal and spatial variations in the Minqin oasis of northwest China. Environmental Modelling & Software, 24(10), 1163–1170. https://doi.org/10.1016/j.envsoft.2009.03.009

Troxell, H. C. (1936). The diurnal fluctuation in the ground-water and flow of the santa ana river and its meaning. Eos, Transactions American Geophysical Union, 17(2), 496–504. https://doi.org/10.1029/TR017i002p00496

Villarreal, S., Vargas, R., Yepez, E. A., Acosta, J. S., Castro, A., Escoto-Rodriguez, M., … Watts, C. J. (2016). Contrasting precipitation seasonality influences evapotranspiration dynamics in water-limited shrublands. Journal of Geophysical Research: Biogeosciences, 121(2), 2015JG003169. https://doi.org/10.1002/2015JG003169

Western, A. W., Grayson, R. B., & Blöschl, G. (2002). Scaling of Soil Moisture: A Hydrologic Perspective. Annual Review of Earth and Planetary Sciences, 30(1), 149–180. https://doi.org/10.1146/annurev.earth.30.091201.140434

White, W. N. (1932). A Method of Estimating Ground-water Supplies Based on Discharge by Plants and Evaporation from Soil: Results of Investigations in Escalante Valley, Utah. U.S. Government Printing Office.

Yue, W., Wang, T., Franz, T. E., & Chen, X. (2016). Spatiotemporal patterns of water table fluctuations and evapotranspiration induced by riparian vegetation in a semiarid area. Water Resources Research, 52(3), 1948–1960. https://doi.org/10.1002/2015WR017546

Zimmerman, D., Pavlik, C., Ruggles, A., & Armstrong, M. P. (1999). An Experimental Comparison of Ordinary and Universal Kriging and Inverse Distance Weighting. Mathematical Geology, 31(4), 375–390. https://doi.org/10.1023/A:1007586507433

Zreda, M., Desilets, D., Ferré, T. P. A., & Scott, R. L. (2008). Measuring soil moisture content non-invasively at intermediate spatial scale using cosmic-ray neutrons. Geophysical Research Letters, 35(21), L21402. https://doi.org/10.1029/2008GL035655

Zreda, M., Shuttleworth, W. J., Zeng, X., Zweck, C., Desilets, D., Franz, T., & Rosolem, R. (2012). COSMOS: the COsmic-ray Soil Moisture Observing System. Hydrol. Earth Syst. Sci., 16(11), 4079–4099. https://doi.org/10.5194/hess-16-4079-2012

CHAPTER 4: COMPARISON OF THE AUTOMATICALLY CALIBRATED GOOGLE EVAPOTRANSPIRATION APPLICATION - EEFLUX AND THE MANUALLY CALIBRATED METRIC APPLICATION

4.1 Abstract

Reliable evapotranspiration (ET) estimation is a key factor for water resources planning**,** attaining sustainable water resources use, irrigation water management, and water regulation. During the past few decades, researchers have developed a variety of remote sensing techniques to estimate ET. The Earth Engine Evapotranspiration Flux (EEFlux) application uses Landsat imagery archives on the Google Earth Engine platform to calculate the daily evapotranspiration at the local field scale (30 m). Automatically calibrated for each Landsat image, the EEFlux application design is based on the widely vetted Mapping Evapotranspiration at high Resolution with Internalized Calibration (METRIC) model and produces ET estimation maps for any Landsat 5, 7 or 8 scene in a matter of seconds. In this research we evaluate the consistency and accuracy of EEFlux products that are produced when standard US and global assets are used. Processed METRIC products for 58 scenes distributed around the western and central United States were used as the baseline for comparison. The goal of this paper is to compare the results from EEFlux with the standard METRIC applications to illustrate the utility of the EEFlux products as they currently stand. Given that EEFlux is derived from METRIC, differences are expected to occur due to differing calibration methods (automatic versus manual) and differing input datasets. The products compared include the fraction of reference ET

(ET_rF), actual ET (ET_a), and surface energy balance components net radiation (R_n), ground heat flux (G), and sensible heat flux (H), as well as T_s, albedo and NDVI. The product comparisons show that the intermediate products of T_s, Albedo, and NDVI, and also R_n have similar values and behavior for both EEFlux and METRIC. Larger differences were found for H and G. Despite the more significant differences in H and G, results show that EEFlux is able to calculate ET_rF and ET_a values comparable to the values from trained expert METRIC users for agricultural areas. For non-agricultural areas such as semi-arid rangeland and forests, the automated EEFlux calibration algorithm needs to be improved in order to be able to reproduce ET_rF and ET_a that is similar to the manually calibrated METRIC products.

4.2 Introduction

Reliable and accurate estimates of water consumption are essential for water rights management, water resources planning and water regulation, especially for agricultural fields that may have specifically attached water rights (Allen et al., 2011a). Over the past few decades, a variety remote sensing techniques have been used to quantify evapotranspiration (ET) at the field and larger scales over large range of agricultural and nonagricultural land uses (Allen et al., 2011a; Anderson et al., 2011; Bastiaanssen, 1998; Courault et al., 2005; Kustas and Norman, 1996; Morton, 1983). Among the types of remote sensing of ET models, surface energy balance techniques are one of the more popular methods used. The Mapping Evapotranspiration at high Resolution with Internalized Calibration (METRIC) application (Allen et al., 2007a, 2005a) is one of the more widely used surface energy balance models in operational practice, and employs principles and techniques that originated with the Surface Energy Balance Algorithms for Land (SEBAL) (Bastiaanssen et al., 1998).

The accuracy of METRIC ET has been evaluated using measured ET by Lysimeter, Bowen ratio and eddy covariance towers in a range of locations of the U.S. (Allen et al., 2015, 2007b; Geli et al., 2017; Irmak et al., 2011; Medellín-Azuara et al., 2018; Morton et al., 2013; Tasumi et al., 2005). Because results of comparisons between METRIC ET and measured ET have been promising, and due to the physically-based employment of surface energy balance algorithms, METRIC is considered to be a well-established model that has been routinely applied as part of the water resources management operations in a number of states and federal agencies (Irmak et al., 2012). However, applying METRIC can often be time-consuming, since a well-trained expert is typically needed to calibrate and run the model. Calibration of METRIC is required for each Landsat scene and image date and entails the determination and assignment of extreme ranges in ET (high and low) to locations within an image. The step calibrates temperature-impacted components of the surface energy balance to reproduce the assigned ET range. Different users who might not be equally experienced can produce different results. To reduce the uncertainties associated with the calibration process, and to save time and money, Allen et al., 2013 and Morton et al., 2013, designed automated calibration algorithms for the METRIC model to generate ET estimates comparable to ones manually produced from well-trained users. Comparison results have suggested that an automated calibration algorithm can estimate ET comparable to the ET estimated by trained users, and the variation within populations of ET produced with automated calibrations have mimicked the variation produced manually between different users (Morton et al., 2013).

Although the automated calibration of the METRIC application reduces some of the expertise requirements of ET production, users still have to accrue and assemble a variety of inputs including the satellite image, land cover map, digital elevation map, local weather data, and soils map, from a variety of sources and platforms. There can be a significant amount of pre-processing required for the different inputs before applying the algorithms. The input and data handling can be one of the most time consuming parts of the overall process. As a means to automate data assembling and handling and to speed the ET computation process, the Earth Engine Evapotranspiration Flux (EEFlux) application was designed and developed on the Google Earth Engine platform based on the METRIC model (Allen et al., 2007a). EEFlux utilizes Landsat imagery archives stored on Google Earth Engine, a cloud-based platform (see Allen et al., 2015). A web-based interface provides users with the ability to request ET estimation maps for any Landsat 5, 7 or 8 scene in a matter of seconds. EEFlux also provides rapid generation of intermediate product maps, such as surface temperature (T_s), normalized difference vegetation index (NDVI) and albedo maps for given Landsat scene that may be useful for other applications besides ET.

The goal of this paper is to compare the results from EEFlux with standard manually calibrated METRIC products to assess the utility and accuracy of EEFlux products as they currently stand. Though METRIC does not represent ground-truth, its standing in the scientific community is established, making it a reasonable benchmark for comparison. Further, given that EEFlux is derived from METRIC, it is useful to examine the differences between their products. Differences are expected due to the differing energy balance calibrations (automatic versus manual), versions of METRIC, geographic location and differing input datasets. Because of the continuing evolution of both METRIC and EEFlux, there are algorithmic differences beyond the energy balance calibrations, but these generally tend to have more minor impacts on the final ET products relative to calibration and input differences. Therefore, this paper does not seek to trace each algorithmic difference but touches on some of the significant known differences. The products compared include the fraction of reference ET (ET_rF), actual ET (ET_a), net radiation (R_n), ground heat flux (G), sensible heat flux (H), T_s, albedo and NDVI. Those products were gathered from 58 METRIC scenes in the western and central United States that were produced by trained individuals.

4.3 Materials and Methods

4.3.1 Study Area

A suite of images from different parts of the western and central U.S. were chosen to compare the performance of automatically calibrated EEFlux to manually calibrated METRIC, and locations within agricultural fields and non-agricultural land areas were examined. These areas were selected due to the importance of water in the areas and the significant impacts of water on the study areas' economies. In this comparison analysis, we used existing processed METRIC images that had been developed to identify or address particular water resources issues in key areas. Analyzing different regions of the U.S. provided a basis for examining regional differences in comparison statistics.

In total 58 Landsat image dates were evaluated in this study. Figure 4.1 shows the Landsat scene locations and study areas of the research. In central Nebraska, areas along the Platte River were the focus of study, where 15 Landsat images (Paths 29-30 and Rows 31-32), during summer 2002, were utilized. In western Wyoming, agricultural areas along the Green River were evaluated. That area falls into 2 Landsat rows on a single path (Path 37 and Rows 30-31). We utilized 9 Landsat images during summer 2011 for the comparison. Southern California was the third study area (Path 39 and Row 37). Due to its very dry climate, the California location had the highest frequency of cloudless images, so that we were able to evaluate 13 Landsat images from late January 2014 to early November 2014. A large irrigated area in southern Idaho comprised a fourth area containing 15 Landsat image dates from year 2016 (Path 40 and Row 30). That location represents a large irrigated region receiving irrigation water from the Snake River and from the Snake Plain Aquifer. The fifth location was comprised of agricultural areas in the Klamath basin of southern Oregon and northern California where we evaluated 6 Landsat images (Path 45 and Row 31), during the growing season of year 2004.

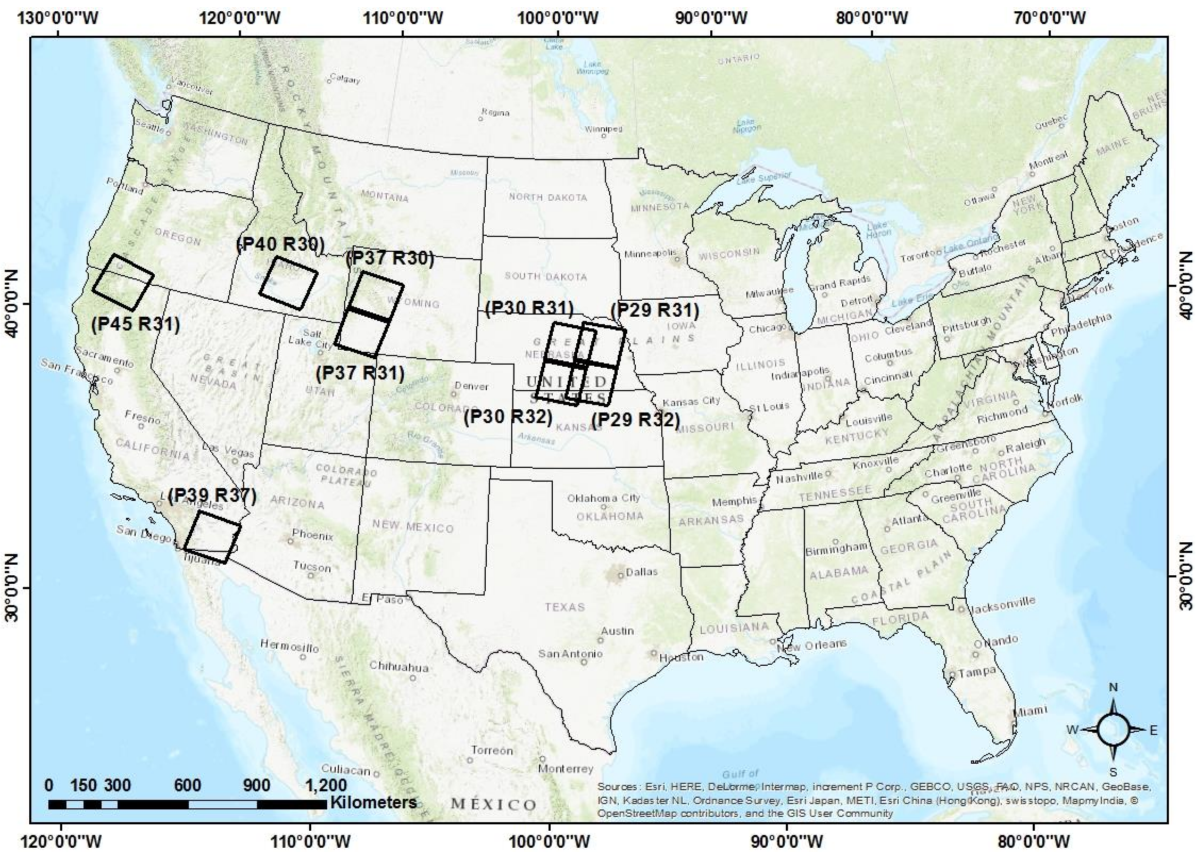

Figure 4.1. Locations of Landsat Scenes evaluated in this study.

4.3.2 Methods

Because the objective of this study was the comparison between the automatically calibrated EEFlux products to manually produced METRIC products, we discuss the primary differences between the two applications and refer the readers to primary documents that explain the details of the METRIC model (e.g., Allen et al., 2011a, 2007a, 2005a; Bastiaanssen et al., 1998; Irmak et al., 2012). We note that the Google Earth Engine-based EEFlux application is still being actively developed by the University of Nebraska-Lincoln (UNL), University of Idaho (UI) and Desert Research Institute (DRI). EEFlux production data from version 0.9.4 was used in this study.

In this section, we briefly explain the sampling methods we used and introduce the criteria used to compare EEFlux and METRIC products. We note that METRIC algorithms have been improved upon and evolved over time, with applications of METRIC in the study areas occurring over a number of different years (2002-2016), and using different versions of METRIC algorithms. The different versions of METRIC include differences in produced energy balance components that are generally minor, for example, in the calculation of ground heat flux and aerodynamic roughness.

4.3.2.1 Similarities and Differences between EEFlux and METRIC

EEFlux employs primary METRIC algorithms that conduct a full energy balance at the land surface and calculate latent heat energy (LE, W/m^2) on a pixel by pixel basis as a residual of the surface energy balance equation:

$$LE = R_n - G - H \tag{1}$$

where LE is heat energy used by water in its phase change from liquid to gas during the ET_a process, R_n is net radiation flux density (W/m^2); G is the ground heat flux density (W/m^2) representing sensible heat conducted into the ground; and H is the sensible heat flux density (W/m^2) convected into the air. LE is estimated at the exact time of the satellite overpass for each pixel. ET_a is then calculated by dividing LE by the latent heat of vaporization:

$$ET_{inst} = 3600 \frac{LE}{\lambda \rho_w} \tag{2}$$

where ET_{inst} is the instantaneous ET flux (mm h^{-1}); 3600 converts seconds to hours; ρ_w is the density of water (~1000 kg m^{-3}); and λ is the latent heat of vaporization (J kg^{-1}) that can be computed using T_s, which is the surface temperature (K):

$$\lambda = [2.501 - 0.00236(T_s - 273.15)] \times 10^6 \quad (3)$$

The ET_rF is calculated for each pixel as the ratio of the computed ET_{inst} from each pixel to the instantaneous tall crop reference evapotranspiration (ET_r):

$$ET_rF = \frac{ET_{inst}}{ET_r} \quad (4)$$

ET_rF is used as a vehicle for extrapolating ET from the instant of the overpass to the surrounding 24-hour period. Lastly, daily ET_a over the 24 hour period is calculated by multiplying ET_rF values for each individual pixel by the daily ET_r computed from local or gridded weather data, assuming consistency between ET_rF at overpass time and ET_rF for the 24-hour period (Allen et al., 2007a):

$$ET_a = ET_rF \times ET_r \quad (5)$$

Equivalency of instantaneous and 24-hour ET_rF is applied to land uses that typically have an adequate water supply for full ET, including agriculture and wetland classes. For most other classes such as rangeland and forest, the well-known evaporative fraction, EF, (Crago, 1996) is used to extrapolate to the full day, where EF = $ET_{inst}/(Rn\text{-}G)_{inst}$. Both EEFlux and METRIC applications utilize hourly and daily ET_r computed for the tall reference crop of alfalfa to convert ET_rF to daily ET_a, where the tall alfalfa reference approximates maximum, energy-limited ET from a well-watered, extensive surface of vegetation. ET_r is computed using the ASCE Standardized Penman-Monteith method (ASCE 2005).

One of the primary differences between EEFlux and METRIC is in the use of sources of weather data in their calibration and calculations. METRIC generally uses ground-based hourly weather data from an agriculturally sited weather station to calculate ET_r for the solution of the surface energy balance equation during calibration and estimation of any background evaporation caused by recent precipitation events. EEFlux uses gridded hourly and daily weather data stored on Earth Engine. For locations processed in the US, EEFlux uses North American Land Data Assimilation System (NLDAS) (https://ldas.gsfc.nasa.gov/nldas/) (Cosgrove et al., 2003) hourly weather data for calibration and GridMet gridded weather data (Abatzoglou John T., 2013) for determining background evaporation. In California, EEFlux uses spatial California Irrigation Management Information System (CIMIS) (https://cimis.water.ca.gov/) daily weather data, if available for the particular date, instead of GridMet. For locations outside of the conterminous United States, EEFlux uses the six-hourly CFSv2 operational analysis (Saha et al., 2013; Yuan et al., 2011) and the Climate Forecast System Reanalysis (CFSR) (http://cfs.ncep.noaa.gov/cfsr/) (Saha et al., 2010) gridded weather data for all calculations.

The use of gridded weather data in EEFlux can explain, to some extent, differences between METRIC and EEFlux final products, including estimates for daily ET_a. This is discussed in more detail in the following sections. More detailed information on METRIC and EEFlux ET_r calculations is found elsewhere (Allen et al., 2005b, 2015; Blankenau, 2017).

During calibration, METRIC and EEFlux solve the energy balance equation by applying an estimate for ET_a at low ET and high ET conditions and solving for H = Rn – G – LE. The low and high ET calibration end-points are referred to as hot and cold pixels. In METRIC, these end-points are searched for automatically or manually, and EEFlux, they are determined automatically. LE is computed by multiplying ET_r by the assumed fraction of ET_r at the calibration points (typically between 0 and 0.1 for the hot pixel and between 1 and 1.05 for the cold pixel). The estimate for instantaneous ET_r does not have a large effect on the ET_rF or ET_a values, since ET_rF is assigned to the end-point conditions. However, it does have an impact on the internally computed H, which is used to absorb and later correct for systematic biases in the other parameters, including Rn, G, albedo, aerodynamic roughness and ET_r (Allen et al., 2007a).

A significant internal difference between EEFlux and METRIC is in the way they calculate G. Some versions of METRIC evaluated calculated G by the following equations depending on the pixel leaf area index (LAI) value:

$$\frac{G}{R_n} = 0.05 + 0.18e^{-0.521\,LAI} \qquad (LAI \geq 0.5) \qquad (6a)$$

$$\frac{G}{R_n} = \frac{1.80(T_s\text{-}273.15)}{R_n+0.084} \qquad (LAI < 0.5) \qquad (6b)$$

whereas later versions of METRIC calculated G as a function of sensible heat flux for LAI > 0.5 and equation 6b otherwise. Very recent versions of METRIC calculate G as a function of LAI only. The version of EEFlux evaluated calculated G as:

$$G = (0.1 + 0.17e^{-0.55\,LAI}) \times R_n \qquad (7)$$

LAI is estimated from surface-corrected NDVI. Due to the differences in calculation of G, the G products often do not match well between METRIC and EEFlux. These differences are carried into the calibration of H, as previously described, but are generally factored back out during calculation of ET_a due to the internal bias correction of METRIC and EEFlux. This is shown later in the results.

METRIC and EEFlux use similar methods for estimating aerodynamic roughness length for momentum transfer, z_{om}, used in calculating aerodynamic resistance in the calculation of H, sensible heat flow from the surface to the air. z_{om} is estimated as a function of estimated LAI for agricultural land classes and as fixed values for nonagricultural classes. METRIC and EEFlux apply a Perrier (1982) roughness function for trees, where roughness is a convex function of amount of ground cover. Some versions of METRIC provide for local modification of land cover maps to specify orchard, vineyard and tall (corn) crops so that special estimation can be made for z_{om} as well as albedo and surface temperature to account for shadowing in deep canopies.

4.3.2.2 Sampling method and comparison criteria

For the comparisons, the highest percentage cloud-free images were selected for the five locations and, for the few images having minor cloud cover, a cloud mask was applied to avoid sampling from clouded areas. A minimum thermal threshold of 270 (K) was used to further screen sampling pixels to avoid thermal pixels lying near the edges of cloud masks or at the edge of gaps in Landsat 7 images caused by the Scan Line Corrector failure. Occasionally, thermal pixels in Landsat 7 images are contaminated by cubic convolution-averaged non-data values stemming from the original native thermal resolution of 60 m.

For the comparison, we randomly chose 1000 pixels from specified areas of interest in the Landsat scenes. These areas targeted primary agricultural areas and adjacent non-agricultural areas comprised of rangeland or forests. National Land Cover Database (NLCD) (https://www.mrlc.gov/) raster data were used to distinguish between agricultural and non-agricultural land covers during sampling. Pixels designated as 81 and 82 NLCD class numbers were used to represent agricultural areas. Non-agricultural pixels were sampled from among all pixels not labeled 81 or 82 in the area of interest. We used a 7×7 focal standard deviation on NDVI to avoid sampling from agricultural field edges, which usually contain mixed pixels, by selecting a pixel only when the standard deviation of the NDVI for those 49 pixels was less than 0.05. Pixels with negative values were removed from the sample selection.

Root Mean Square Error (RMSE) and Coefficient of Determination (R^2) were calculated for each set of data to compare EEFlux products with the same products from METRIC. In addition, slopes of EEFlux products vs. METRIC products with zero intercept were calculated to indicate when EEFlux underestimated or overestimated the products, on average, compared to METRIC. In this study, R^2 values higher than 0.8, RMSE values less than 15% of the average magnitude of each product, and slope values between 0.9 to 1.1 were conidered acceptable, in terms of expected error common to operationally produced spatial ET products (Allen et al., 2011a, 2011b, 2007a; Gonzalez-Dugo et al., 2009; Kalma et al., 2008).

4.4 Results

Five locations in the United States comprised of nine Landsat image scenes were used to compare the automatically calibrated EEFlux products to the manually calibrated METRIC products. Although the final and primary products of the applications are ET_rF and ET_a, we also compared intermediate products from the models including T_s, albedo, and NDVI, and the primary components of the energy balance: R_n, G, and H. EEFlux is a user-friendly web-based platform that enables users to download the intermediate products of T_s, albedo, and NDVI in addition to ET_rF and ET_a. Therefore, it is useful to confirm similarity with METRIC for those additional products.

We compared the intermediate and final products for each location and calculated R^2, RMSE, and slopes relative to the METRIC products. Figure 4.2 shows an example comparison for each product sampled from within agricultural fields in Path 29 Row 32 in central Nebraska for a Landsat 5 (2002/06/28) image. Additional graphs of the same format as Figure 4.2 are included for each location studied in the Supplemental Figures 4.1-4.8.

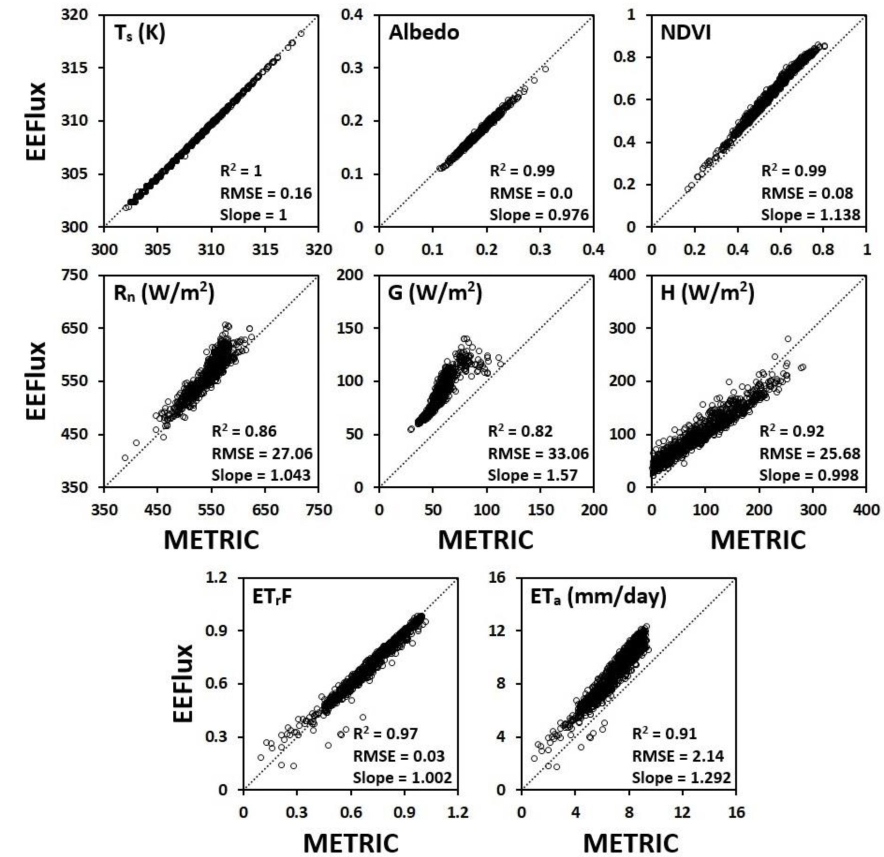

Figure 4.2. Comparison between various components of EEFlux and METRIC models for agricultural fields located in central Nebraska (Path 29 Row 32, Landsat 5, 2002/06/28).

The comparisons in Figure 4.2 indicate that the three intermediate products of T_s, Albedo, and NDVI have nearly identical values between EEFlux and METRIC. Their R^2 and slope values are nearly equal to 1 and they have very small RMSE values. The slope for NDVI is greater than 1 due to the particular METRIC version computing NDVI using top-of-atmosphere reflectance values rather than using surface reflectance values as is done in EEFlux. The R_n and H products are also similar between the two models, with R^2 and slope close to 1. Considering the magnitudes of the two products, RMSE values are relatively small. The EEFlux version evaluated uses a different equation to compute G, as compared to the METRIC version applied in Nebraska. Therefore, as expected, G values do not match well, with a positive offset in EEFlux estimates of about 20 W/m^2; However, the R^2 and RMSE values are still within the acceptable range. Moreover, due to the self-reducing bias reduction used internally in EEFlux and METRIC, the systematic bias in G largely cancels out during production of ET_rF (Allen et al., 2007b).

The agreement found with the intermediate products and energy balance components are good indicators of strong correlation and similarity in algorithm performance between EEFlux and METRIC. ET_rF values from EEFlux and METRIC were very similar, with R^2 and slope close to 1 and RMSE value of 0.03. This indicates similarity in the energy balance calibration performed in EEFlux via the automated scheme and the manually-determined calibration in METRIC. For daily ET_a, however, EEFlux had a significant bias relative to METRIC, with RMSE exceeding 2 mm/d and slope of 1.3. The higher estimation of ET_a from EEFlux, given similarity in ET_rF, traces to the conversion of ET_rF to ET_a by multiplying by daily ET_r, which is derived from synoptic gridded weather data in EEFlux as compared to being derived from local measured point or gridded weather data collected from agricultural environments. The general aridity of synoptic weather data, with generally lower humidity content and higher air temperature than experienced under irrigated conditions, especially in semiarid and arid climates (Jensen and Allen, 2016; Temesgen B. et al., 1999), causes overstatement of ET_r by the Penman-Monteith combination reference equation that presumes a well-watered surface and associated air temperature and humidity parameters (ASCE-EWRI 2005). This is discussed more in a later section.

4.4.1 Overall Summary of EEFlux vs METRIC comparisons

A summary of comparisons over all 58 images and five locations was compiled by combining all sampled data and calculating overall R^2, RMSE, and slope values. For individual image and location comparisons, the reader is referred to Supplemental Tables 4.1-4.6 that provide statistics for both agricultural and non-agricultural areas for each image date. Table 4.1 presents the overall R^2, RMSE, and slope values for all products for agricultural and non-agricultural areas. Intermediate products of T_s, Albedo, and NDVI were relatively similar between agricultural and non-agricultural classes, with R^2 and slope values close to 1 and with relatively small RMSE values. R_n estimates by EEFlux correlated well with those by METRIC, with an average R^2 value of 0.93 and slope of 1.02 for agricultural areas and average R^2 of 0.87 and slope of 1.02 for non-agricultural areas. Relative RMSE for R_n was less than 5%, on average, for R_n for both land covers. The other two energy balance components sampled (G and H) did not match as well between EEFlux and METRIC. The poor agreement for G is attributed to the previously noted differences between METRIC and EEFlux equations for G. Although the equations for G differed between EEFlux and the various METRIC versions, the average RMSE and slope indicate that EEFlux still calculated ET_rF and ET_a values that compared well to METRIC for agricultural areas, with R^2 values of 0.82 and 0.76 for ET_rF and ET_a, respectively. The relatively good agreement for ET_rF and the relatively poor agreement in H is partly explained by the systematic differences in estimates for G, which are embedded into the calibrated estimates for H, and that are then removed from the ET estimates during the ET production steps, due to the internal, systematic bias correction of METRIC and EEFlux. Differences in H are also traceable to the sources used to compute instantaneous ET_r as noted previously, where generally higher estimates in ET_r in EEFlux produce lower values for H during the surface energy balance calibration.

Because METRIC typically uses ground-based weather data for hourly and daily ET_r calculation, and EEFlux uses gridded weather data sets to derive ET_r, the calculated ET_r values used in computations can be different due to differences in origin of weather data and aridity biases common to the gridded weather data sets. While several of the METRIC applications applied only a single ET_r value for an entire Landsat image for both energy balance calibration and for interpolation to 24-hour periods, ET_r values used in EEFlux can vary across the image through the gridded weather data that has an approximately 12 km grid spacing for NLDAS-2 hourly data, for CONUS, and 4 km grid spacing for GRIDMET 24-hour data. In order to explore differences among ET_r values used in METRIC and EEFlux, we calculated averages of gridded ET_r values for each image date and associated ratios of those average values to the typically single scene-wide METRIC ET_r values. Table 4.1 summarizes average slopes of 24-hour EEFlux ET_r values to METRIC ET_r values. On average, over all five locations and the dates evaluated, the grid-based ET_r ran higher than ground-based calculated ET_r by ratios of 1.10 and 1.09 for agricultural and non-agricultural land uses, respectively. The approximately 10% higher ET_r estimation by the gridded data suggests that general ET applications with EEFlux can be biased 10% high solely due to the aridity bias of the gridded data sets (Blankenau, 2017; Lewis et al., 2014). This bias is the basis for ongoing studies and development of methods to identify and condition gridded data sets to remove aridity bias prior to calculation of reference ET, which represents near maximum ET in well-watered environments (Jensen and Allen 2016). We further explored the ET_r biases for each individual date and location as described later in the discussion section.

Table 4.1. Average values for R2, RMSE, and slope for EEFlux vs. METRIC, based on a comparison over all data (Ag sample size = 47838, Non-Ag sample size = 35110).

Product	Average R^2		Average Slope		Average RMSE	
	Ag	Non-Ag	Ag	Non-Ag	Ag	Non-Ag
T_s (K)	1.00	1.00	1.00	1.00	0.53	0.51
Albedo	0.98	0.97	1.00	1.00	0.01	0.01
NDVI	0.97	0.93	1.09	1.11	0.07	0.06
R_n (W/m^2)	0.93	0.87	1.02	1.02	26.77	31.63
G (W/m^2)	0.53	0.26	1.43	1.22	41.77	40.59
H (W/m^2)	0.47	0.37	1.03	0.94	69.02	71.53
ET_r (mm)	---	---	1.10	1.09	---	---
ET_rF	0.82	0.45	0.94	0.64	0.13	0.21
ET_a (mm/day)	0.76	0.44	1.01	0.70	1.23	1.39

4.4.2 ET_rF and ET_a examples

For most applications, the primary products of EEFlux and METRIC that are of most interest are ET_rF and ET_a. Therefore, this results section focuses on those two products. Figure 4.3 illustrates ET_rF and ET_a correlations and behavior between EEFlux and METRIC over individual sample points for two locations (central Nebraska and southcentral Idaho) and two Landsat systems for agricultural areas. The top two rows of graphs show good EEFlux calibration and estimation relative to the METRIC calibration and estimation, producing relatively good R^2, RMSE, and slope values. The lower row of graphs illustrates a poorer calibration where EEFlux substantially underestimated ET_rF and ET_a especially in the lower end of the ET spectrum, as reflected in poor R^2, RMSE, and slope values. The poor agreement for the particular location and date indicate that the EEFlux automated calibration algorithms can fail under some conditions. As previously noted, those algorithms are under continued improvement by the UNL and UI developers. While the automated calibration of EEFlux is prone to producing poor calibrations under some circumstances, it should be noted that manually calibrated METRIC can also depart from the ground truth (Anderson et al., 2012). In the 2002/5/2 application shown in Figure 4.3, the METRIC application diagnosed a substantial impact of recent rain on elevating minimum ET_rF to no lower than 0.6 across the Landsat scene, even for bare soils. The EEFlux application, which used GRIDMET-based precipitation, did not diagnose that same evaporation residual, apparently due to low precipitation amounts present in the gridded data set, and EEFlux therefore projected minimum values for ET_rF of 0.0. This last illustration illustrates some of the challenges associated with what are sometimes labeled as ‘wet’ images, where atmospheric conditions are clear for processing, but the land surface is relatively wet from recent precipitation events.

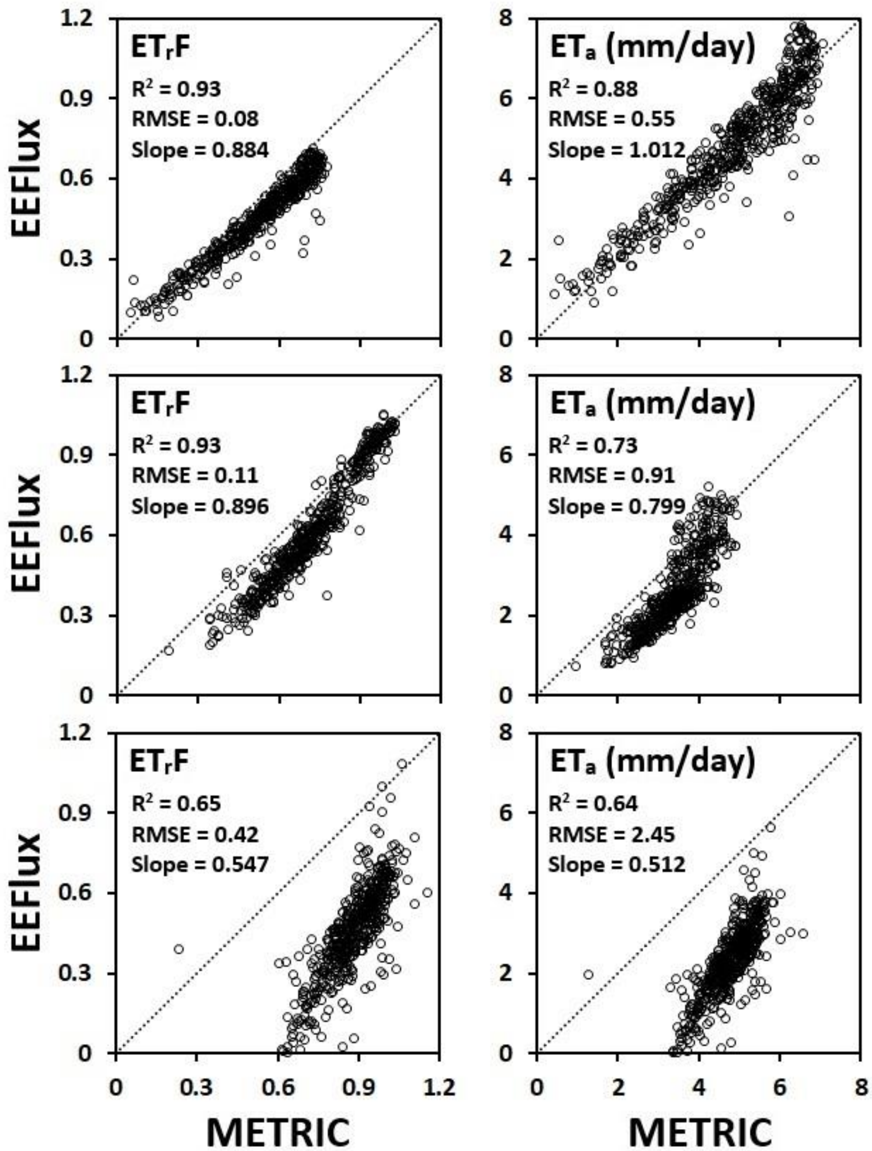

Figure 4.3. Examples of ET_rF and ET_a calibrations at agricultural fields in different locations. The upper two graphs: good calibration (P29 R31, Landsat 7, central Nebraska, 2002/9/8). The middle two graphs: relatively good calibration (P40 R30, Landsat 7, southcentral Idaho, 2016/9/27). The lower two graphs: poor calibration (P30 R31, Landsat 5, central Nebraska, 2002/5/2).

In the following section, we explore the differences between EEFlux and METRIC by discussing average statistics determined for ET_rF and ET_a for each of five locations.

4.4.3 EEFlux ET_rF vs METRIC ET_rF

Table 4.2 provides a statistical summary for ET_rF comparisons for each of the nine Landsat path and row locations evaluated that were located in five general USA locations. Statistics are provided for agricultural and non-agricultural land uses. Figure 4.4 illustrates average slope values for ET_rF for the different locations and Figure 4.5 presents average RMSE values for ET_rF. The supplemental Figure 4.9 provides similar plots showing average R^2 values for ET_rF. As shown in Table 4.2 and Figures 4.4 and 4.5, there was minor underestimation of ET_rF values by EEFlux, relative to METRIC, within agricultural land uses for some locations. However, the results were generally good, and EEFlux, on average, is judged to have produced reasonably accurate and useful ET_rF imagery, particularly in southern California, southern Oregon, the Green River area of Wyoming, and in southern Idaho, with average R^2 values higher than 0.84 and average slope values larger than 0.93, and where, in some of the areas, slopes were nearly 1.00. Moreover, the RMSE values in these areas were almost all less than 10% of the average magnitudes of ET_rF values (0-1.05). RMSE values of 10% are considered by Allen et al., 2011b and Jensen and Allen (2016) to be common to ET estimation and ET measurement. Within the agricultural fields in Nebraska, EEFlux performance was not as good or consistent as for the other locations. However, RMSE and R^2 values are still within our acceptable range, except for one scene area which had an ET_rF RMSE value of 0.28 and R^2 value of 0.69. This was previously illustrated in Figure 4.3 and is explained by the impact of recent rains, where EEFlux underestimated ET_rF for agricultural areas for several dates in central Nebraska.

R^2, slope and RMSE values in Table 4.2 and Figures 4.4 and 4.5 indicate that EEFlux ET_rF values did not match METRIC ET_rF values as strongly for non-agricultural land uses as they did for agricultural land uses. EEFlux tended to underestimate ET_rF for all non-agricultural land covers sampled and produced RMSE values that were higher than those for agricultural land uses within the same Landsat scene. Some of the differences are due to different means for estimating soil heat flux, for aerodynamic roughness of natural vegetation systems, and potentially due to impacts of the digital elevation model (DEM) used to estimate solar radiation and aerodynamic behavior in complex terrain that is characteristic of natural systems. Differences are also attributed to the weather data sources used in the application of the evaporative fraction (EF) function to nonagricultural land uses, where a ratio of ET_a to $R_n – G$ is used to transform ET_rF to 24-hour ET_rF values, rather than assuming that 24-hour ET_rF equals instantaneous ET_rF as is done for agricultural land uses (Allen et al., 2007b). The typically stronger ET_r from gridded weather data impacts this transformation. Causes of these differences, with location, continue to be investigated.

Table 4.2. Average values for R^2, slope and RMSE for ET_rF for each Landsat scene location evaluated. RMSE values are unitless.

Path	Row	Year	Processed Year	Ag ET_rF				Non-Ag ET_rF			
				n	R^2	Slope	RMSE	n	R^2	Slope	RMSE
29	31	2002	2014	2003	0.84	0.80	0.16	1063	0.83	0.63	0.26
29	32	2002	2014	2387	0.86	0.86	0.15	1309	0.32	0.42	0.30
30	31	2002	2014	3187	0.69	0.72	0.28	1910	0.19	0.40	0.42
30	32	2002	2014	3302	0.94	0.94	0.11	3906	0.50	0.55	0.28
37	30	2011	2013	4815	0.84	0.93	0.11	915	0.52	0.61	0.18
37	31	2011	2013	3608	0.89	1.05	0.10	1921	0.31	0.72	0.14
39	37	2014	2014	10152	0.86	1.00	0.13	6311	0.61	0.81	0.14
40	30	2016	2016	12164	0.89	0.95	0.10	12416	0.52	0.81	0.16
45	31	2004	2011	5765	0.89	0.98	0.10	5759	0.49	0.70	0.18

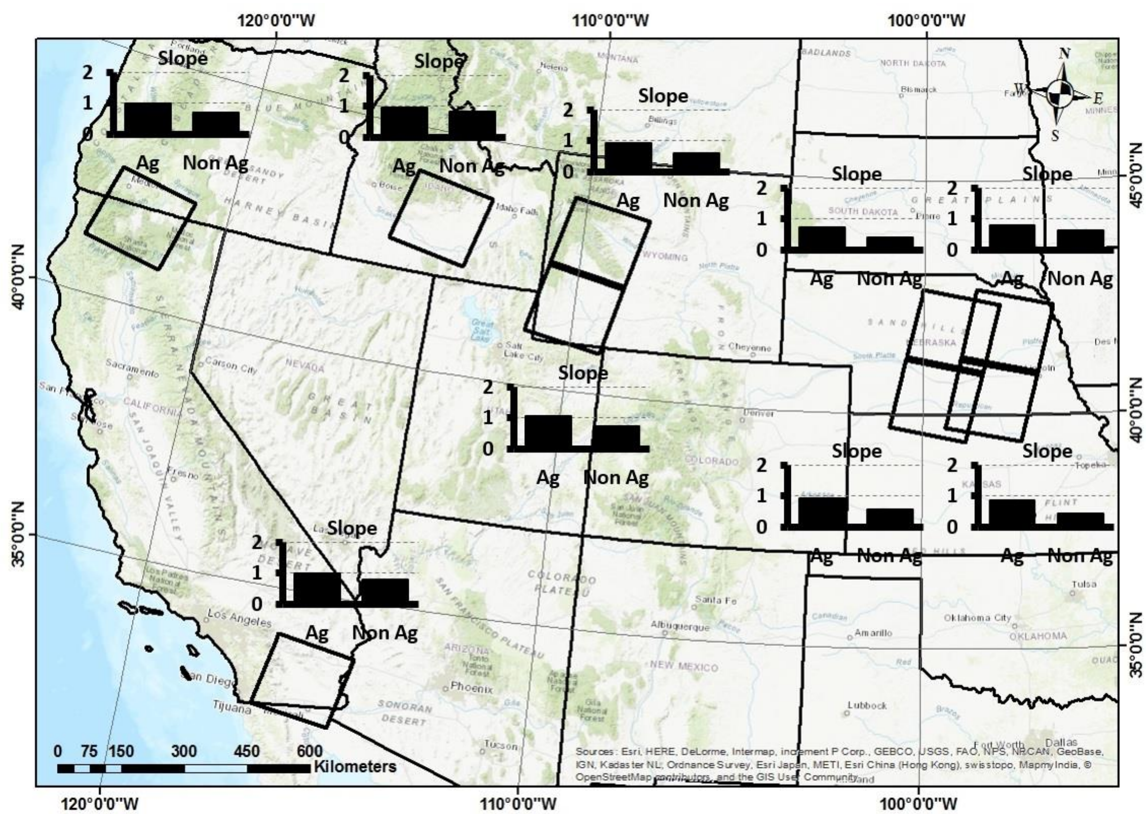

Figure 4.4. Average slope values for ET_rF for EEFlux vs. METRIC for different locations and scenes for agricultural and nonagricultural land uses.

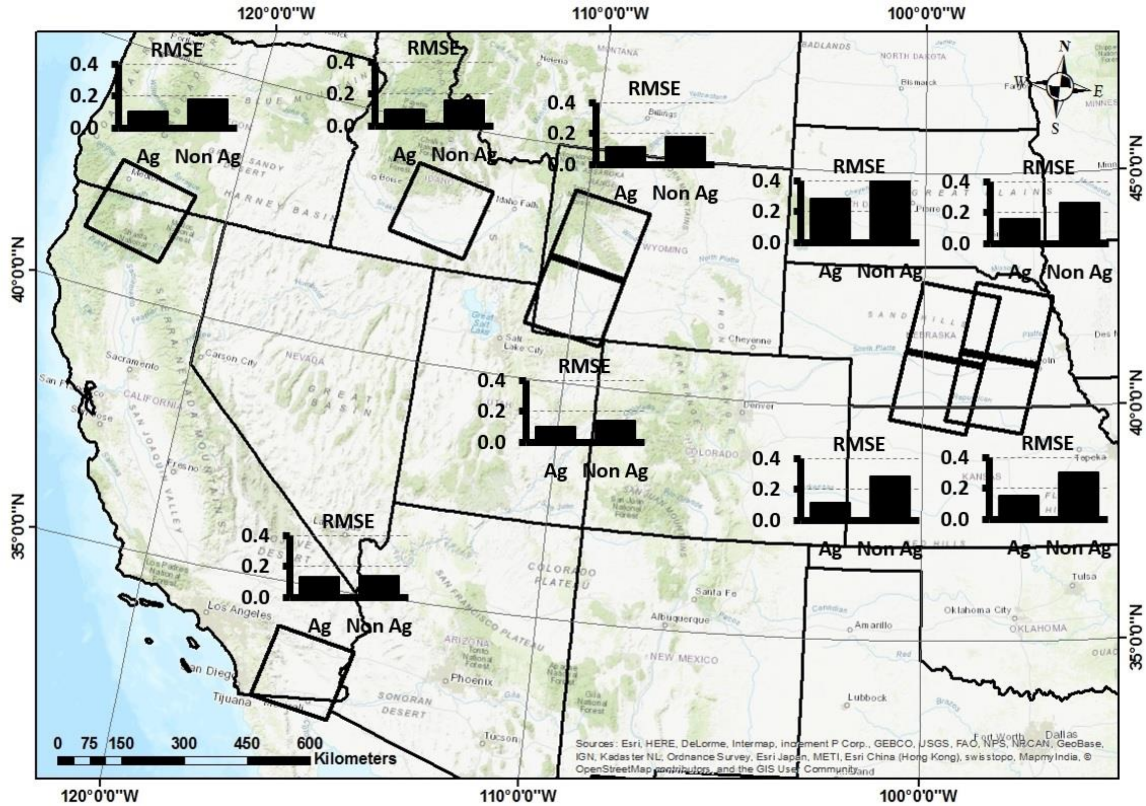

Figure 4.5. Average RMSE values for ET_rF for EEFlux vs. METRIC for different locations and scenes for agricultural and nonagricultural land uses.

4.4.4 EEFlux ET_a vs METRIC ET_a for Individual Locations

Table 4.3 provides a statistical summary for ET_a comparisons for the nine Landsat path and row locations evaluated, for both agricultural and non-agricultural land uses. Figures 4.6 and 4.7 show average slopes and RMSE values for ET_a. Supplemental Figure 4.10 provides similar plots for average R^2 values for ET_a. As shown in Table 4.3 and Figures 4.6 and 4.7, slope values increased over those for ET_rF for both agricultural and non-agricultural areas for most of the locations investigated. As discussed previously, that is largely a consequence of ET_r overestimation by use of the gridded weather data set (Blankenau, 2017; Lewis et al., 2014). R^2 and slope values were generally within the acceptable accuracy range for agricultural areas. R^2 values were mostly larger than 0.8 and

RMSE values were generally in the range of 0.9 to 1.1 mm/d, except one location where it was 0.69 mm/d. Most R^2 values were less than 0.8 for non-agricultural land uses and RMSE values in all locations, except for southern California and southern Idaho, were larger for non-agricultural land uses as compared to agricultural lands. Slope values show that EEFlux tended to underestimate ET_a for non-agricultural land uses everywhere except for southern Idaho. In general, ET_a was substantially lower in non-agricultural land uses than in agricultural areas due to limits on ET imposed by precipitation amount. The agricultural areas sampled were generally all irrigated.

Table 4.3. Average values for R^2, slope and RMSE for 24-hour ET_a for each Landsat scene location evaluated. RMSE values have units of mm/d.

Path	Row	Year	Processed Year	Ag ET_a				Non-Ag ET_a			
				n	R^2	Slope	RMSE	n	R^2	Slope	RMSE
29	31	2002	2014	2003	0.84	0.92	0.93	1063	0.83	0.73	1.90
29	32	2002	2014	2387	0.87	1.11	1.76	1309	0.39	0.54	2.33
30	31	2002	2014	3187	0.50	0.69	1.89	1910	0.49	0.46	2.67
30	32	2002	2014	3302	0.86	0.91	0.92	3906	0.52	0.57	1.78
37	30	2011	2013	4815	0.83	0.91	1.11	915	0.58	0.54	1.58
37	31	2011	2013	3608	0.87	1.02	0.88	1921	0.34	0.62	1.13
39	37	2014	2014	10152	0.76	1.10	1.22	6311	0.51	0.96	0.97
40	30	2016	2016	12164	0.82	1.13	1.29	12416	0.53	1.05	1.15
45	31	2004	2011	5765	0.89	1.11	0.80	5759	0.54	0.82	0.86

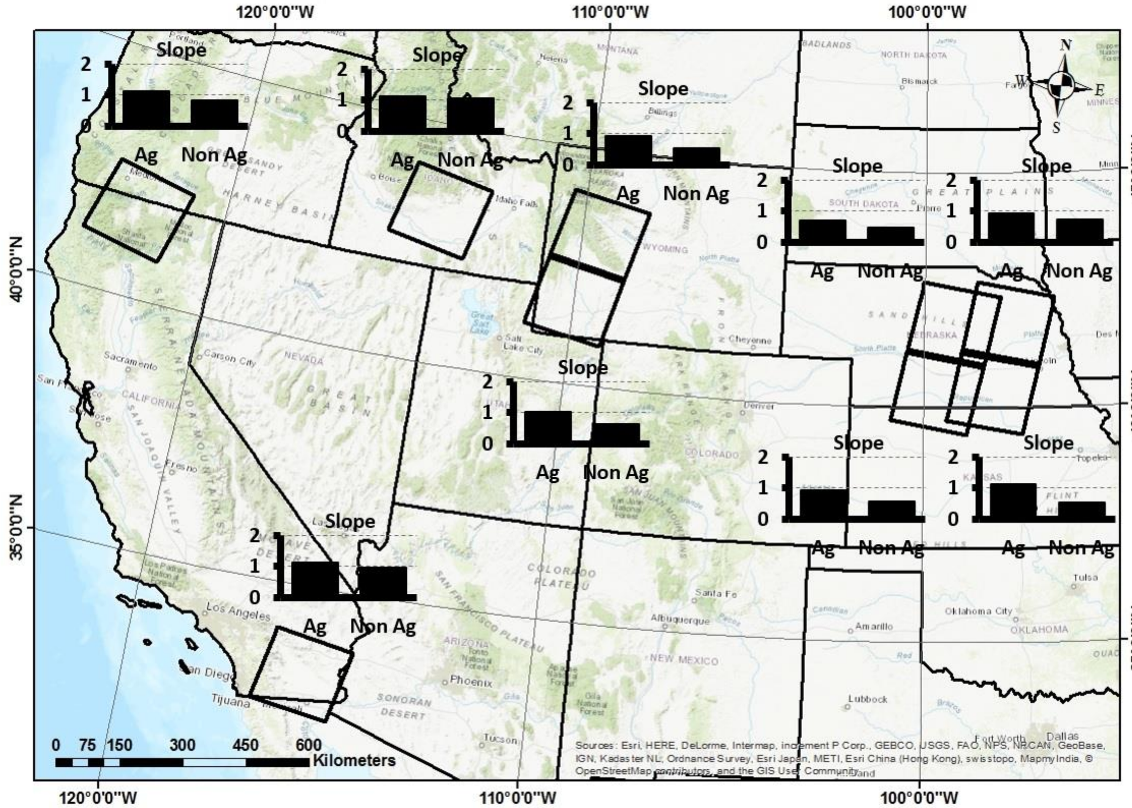

Figure 4.6. Average slope values for ET_a for EEFlux vs. METRIC for different locations and scenes for agricultural and nonagricultural land uses.

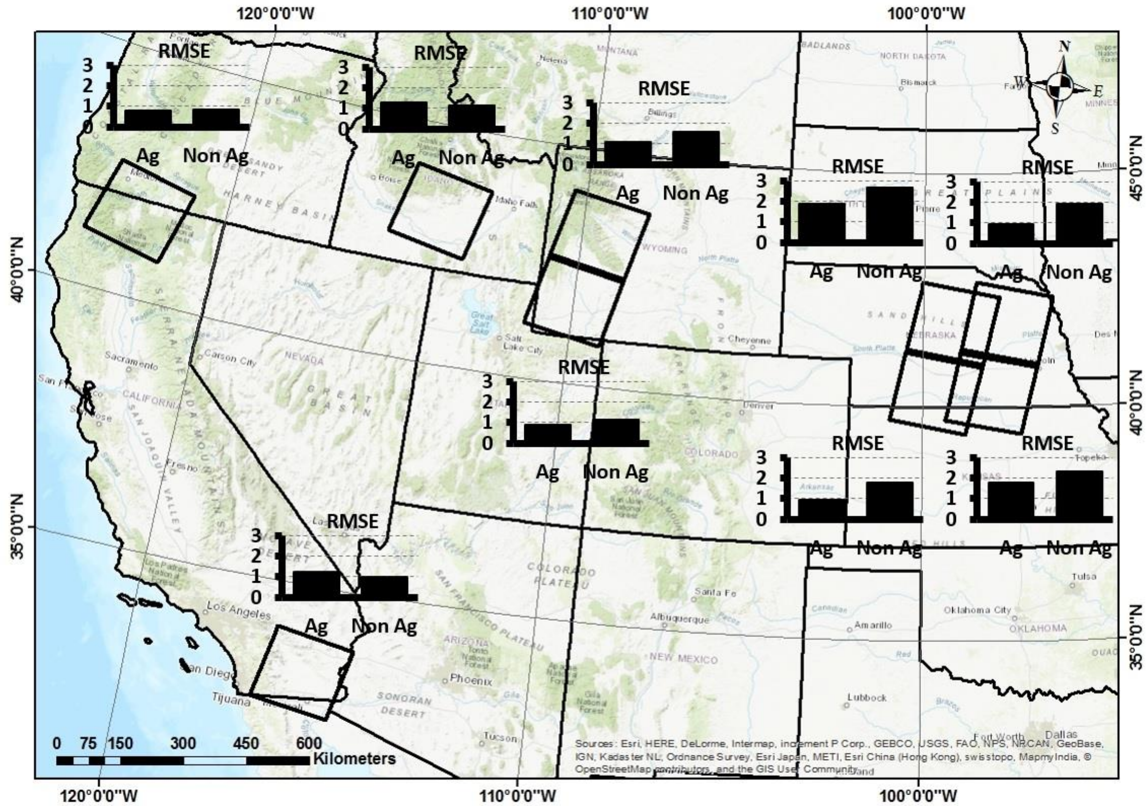

Figure 4.7. Average RMSE values (mm/d) for ET_a for EEFlux vs. METRIC for different locations and scenes for agricultural and nonagricultural land uses.

4.4.5 Time dependency of EEFlux performance

Because the study area in southern California had the broadest time series of processed images, we chose this location to explore the time dependency of EEFlux performance and to assess the impact of time of year on performances of the two processing systems. As described earlier we evaluated 13 processed Landsat 8 images for the southern California location. The first and last images evaluated were the 26th of January 2014 and the 10th of November 2014, respectively. Figure 4.8 shows R^2, slope, and RMSE values for ET_rF and ET_a for agricultural and non-agricultural land uses for different comparison dates. Generally, there was not any statistical correlation between the performance of EEFlux as compared to that of METRIC with time of year. While R^2 values for both ET_rF and ET_a were always higher for agricultural land uses as opposed to non-agricultural land uses, no trends through time were detected. The slope values were similar over time for both agricultural and non-agricultural land uses. However, slopes for non-agricultural ET_rF and ET_a do show a slight trend, decreasing from March through November. RMSE values for ET_rF, like R^2 and slope values did not follow any visible trend during 2014 in the agricultural land uses in southern California. However, as observed in the bottom plot of Figure 4.8, RMSE values for ET_a increased for both land covers during summer time, indicating larger differences between EEFlux ET_a values and METRIC values during the primary growing season when ET_a was higher.

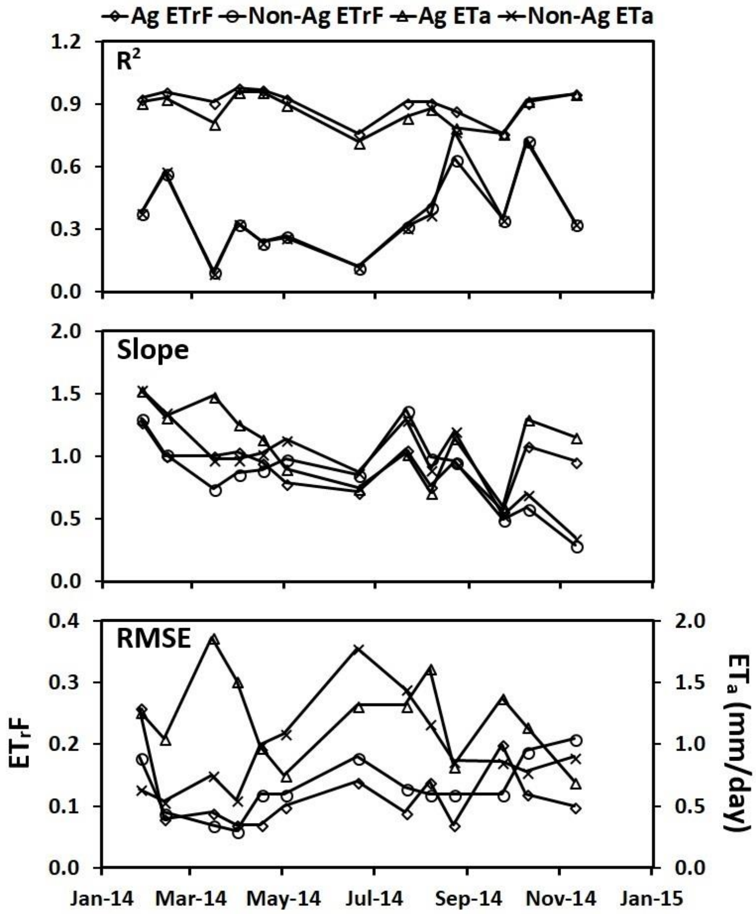

Figure 4.8. a) R2 b) slope and c) RMSE values for EEFlux vs. METRIC for a series of comparison dates (Path 39 Row 37).

4.5 Discussion

Based on the comparison results, we conclude that the implementation of EEFlux on GEE, including the automated internal calibration, has been relatively successful. EEFlux ET_rF and ET_a results matched those from manually applied METRIC applications for most of the agricultural areas evaluated. For some dates within central Nebraska, EEFlux performance was poorer than for the other locations for agricultural land uses. Some of the increased error is due to fewer Landsat images processed for that region due to extensive cloud clover. In one location we were able to evaluate only 3 Landsat image dates (Path 29

Row 31) and for the other three Worldwide Reference System (WRS) scene areas we evaluated 4 image dates; whereas we evaluated 13 Landsat Image dates in California and 15 image dates in Idaho. Having fewer image dates can result in more extreme means due to greater impacts of outliers and/or a smaller sample size. Other impacts, as noted, for central Nebraska is the tendency for more frequent and substantial rainfall during the growing season that increases the impact of background evaporation. This complicates the image calibration. In non-agricultural land uses, EEFlux did not match with METRIC as well as it did for agricultural land uses. This may be partially due to differences among G and H products and DEM sources used. As noted earlier, we evaluated EEFlux version 0.9.4 and, as EEFlux is still in progress, the automated calibration algorithms are expected to be improved in the future, which should result in even more accurate ET_rF and ET_a estimates.

4.6 Other Analyses

4.6.1 Source of Reference ET Estimation

Besides using ET_r for internal energy balance calibration and computation, EEFlux uses gridded weather data to extrapolate instantaneous daily ET_rF values to the 24-hour period, which is then multiplied by 24-hour ET_r to calculate daily ET_a values. Figure 4.9 shows ratios of gridded ET_r values versus the single ET_r values generally used in METRIC computations for each image date and location. As shown in Figure 4.9, for most dates and locations, the average gridded ET_r values used in EEFlux were higher than the associated single average gridded ET_r values used by METRIC, with variation within each location from about 0.9 to 1.3. As we discussed earlier, the average EEFlux-gridded ET_r was larger than the METRIC calculated, ground-based ET_r values by an average ratio of 1.10 and 1.09 for agricultural and non-agricultural land uses, respectively. The higher 24-hour ET_r estimation in EEFlux due to the gridded weather data source, leads to some degree of daily ET_a overestimation.

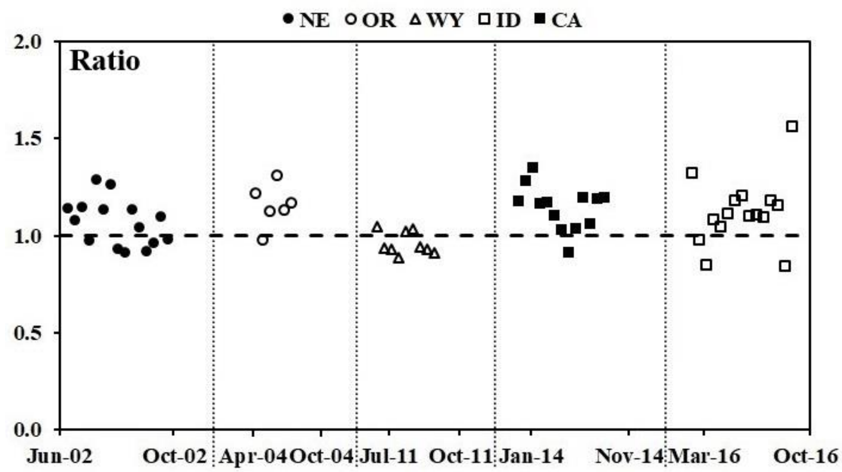

Figure 4.9. Ratio of calculated 24-hour ET_r used in EEFlux (based on gridded weather data) to that used in the METRIC model (calculated from ground-based weather station data) for five different Landsat scene locations and comparison days.

4.6.2 Impact of METRIC Calibration Style (User) on METRIC Estimation

Some of the differences noted between ET_rF and ET_a from EEFlux vs. METRIC could stem from the semi-subjective behavior for METRIC estimates that are traceable to the particular individual user and situation responsible for the METRIC application and calibration. To explore the impact of METRIC user, two different METRIC users with varying experience and expertise in ET image production applied similar METRIC algorithms independently during two different time periods, where they calibrated two image dates in central Nebraska (Path 29 Row 32) for year 2015. Figure 4.10 shows the results of comparisons for two processed Landsat 8 image dates for the agricultural land use. The top two comparisons belong to 18th of July and the two in the bottom belong to 4th of September. While R^2 of ET_rF and ET_a values are higher than 0.89 for both days, the RMSE and slope values are considered to be acceptable for only July 18th, and is not in the acceptable range for September 4th. The average R^2 of ET_rF and ET_a values for combination of all the data were 0.78 and 0.73, respectively. The combined slope values were 0.9 for ET_rF and 1.07 for ET_a values, which do fall within the acceptable ranges. Scatter in the comparisons is due to small differences in the METRIC version used or in internal parameter settings in METRIC such as corrections for low albedo in crops such as corn that have deep canopies (Allen et al., 2007b). Combined RMSE values were 0.14 for ET_rF and 0.98 mm/d for ET_a values. A comparison of these average R^2, slope and RMSE values with average values for EEFlux vs. METRIC summarized in Table.4.1, suggests that, for the locations evaluated, that the EEFlux automated calibration algorithm is generally able to estimate ET_rF and ET_a values for agricultural land uses that are comparable in accuracy and reproducibility to differences noted from METRIC when applied by different trained users. This finding is consistent with that of Medellín-Azuara 2018.

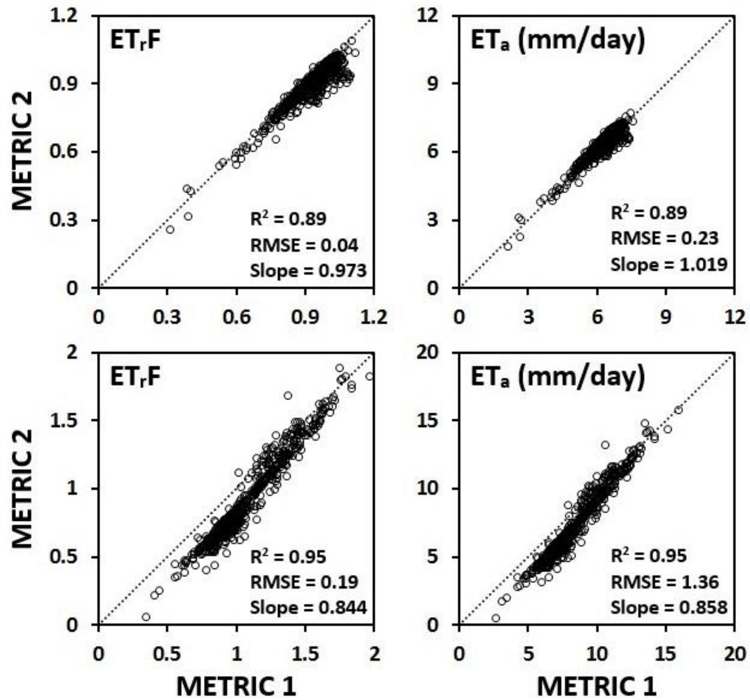

Figure 4.10. Comparison between METRIC products (ET_rF and ET_a) that were manually calibrated and produced by 2 different METRIC users. The top two comparisons are for 18th of July and the bottom two are for 4th of September.

4.7 Summary and Conclusions

The consistency and accuracy of ET products from the automatically calibrated Google Earth Engine EEFlux application were evaluated by comparing EEFlux products to those from manually calibrated METRIC images for 58 Landsat images. Sets of Landsat images from five study locations distributed across central and western USA included both agricultural and non-agricultural land uses. The agricultural areas sampled were typically irrigated. The comparison results show that EEFlux is able to calculate ET_rF and ET_a values in agricultural areas that are comparable to those produced by trained METRIC users and that are generally within accepted accuracy ranges. Differences between EEFlux and METRIC were larger for non-agricultural land uses showing room for improvement to the

EEFlux algorithms. Differences noted could, in part, be the result of EEFlux struggling to account for background evaporation at the hot pixel calibration end point. Hot pixel bias in the hot pixel assigned ETrF tends to affect the non-agricultural pixels more than agricultural pixels because the non-agricultural pixels tend to have lower ET and are therefore more impacted by error or bias in the overall surface energy balance. Another likely reason for the poorer performance for non-agricultural land uses is a bias introduced during the application of EF to extrapolate instantaneous ET_rF to daily ET_rF, as discussed earlier. The EF relies on the instantaneous and 24-hour ET_r, R_n and G being accurate. We have established that both ET_r and G estimates deviate between METRIC and EEFlux, so we would expect to have different results in the non-agricultural areas. In fact, we should expect larger differences between METRIC and EEFlux in non-agricultural areas than in agricultural areas given that the instantaneous ET_rF used in the agricultural areas is robust in the face of biased G and instantaneous ET_r. While EEFlux is still a work in progress, it can be used to rapidly estimate ET_a for areas of interest. However, it is important to be aware of biases in 24-hour ET_a estimates due to aridity biases in the gridded weather data used by EEFlux. Results presented in this paper should provide a good overview of the general variability and error to be expected for ET_rF and ET_a estimates from EEFlux.

4.8 Acknowledgments

We acknowledge and greatly appreciate funding support and development support provided by Google Earth Engine, as well as very positive encouragement by Google Earth Engine to initiate the EEFlux development to promote global access to global ET estimates.

EEFlux development was also supported by the National Aeronautics and Space Administration (NASA) and by the United States Geological Survey (USGS) by funding Landsat Science Team members Allen, Kilic and Huntington. The USGS and state and local water resources agencies, including Idaho Department of Water Resources, the Wyoming Office of the State Engineer, and the Central Platte Natural Resources District supported the development and production of the original METRIC ET products. Work was also supported by the Idaho and Nebraska Agricultural Experiment Stations.

4.9 References

Abatzoglou John T., 2013. , in: Development of Gridded Surface Meteorological Data for Ecological Applications and Modelling.

Allen, R.G., Burnett, B., Kramber, W., Huntington, J., Kjaersgaard, J., Kilic, A., Kelly, C., Trezza, R., 2013. Automated Calibration of the METRIC-Landsat Evapotranspiration Process. JAWRA J. Am. Water Resour. Assoc. 49, 563–576. https://doi.org/10.1111/jawr.12056

Allen, R.G., Irmak, A., Trezza, R., Hendrickx, J.M.H., Bastiaanssen, W., Kjaersgaard, J., 2011a. Satellite-based ET estimation in agriculture using SEBAL and METRIC. Hydrol. Process. 25, 4011–4027. https://doi.org/10.1002/hyp.8408

Allen, R.G., Morton, C., Kamble, B., Kilic, A., Huntington, J., Thau, D., Gorelick, N., Erickson, T., Moore, R., Trezza, R., Ratcliffe, I., Robison, C., 2015. EEFlux: A Landsat-based Evapotranspiration mapping tool on the Google Earth Engine. American Society of Agricultural and Biological Engineers, pp. 1–11. https://doi.org/10.13031/irrig.20152143511

Allen, R.G., Pereira, L.S., Howell, T.A., Jensen, M.E., 2011b. Evapotranspiration information reporting: I. Factors governing measurement accuracy. Agric. Water Manag. 98, 899–920. https://doi.org/10.1016/j.agwat.2010.12.015

Allen, R.G., Tasumi, M., Trezza, R., 2007a. Satellite-Based Energy Balance for Mapping Evapotranspiration with Internalized Calibration (METRIC)—Model. J. Irrig. Drain. Eng. 133, 380–394. https://doi.org/10.1061/(ASCE)0733-9437(2007)133:4(380)

Allen, R.G., Tasumi, M., Trezza, R., Kjaersgaard, J., 2005a. METRIC: mapping evapotranspiration at high resolution–applications manual for Landsat satellite imagery. Univ. Ida. 130.

Allen, R.G., Tasumi Masahiro, Morse Anthony, Trezza Ricardo, Wright James L., Bastiaanssen Wim, Kramber William, Lorite Ignacio, Robison Clarence W., 2007b. Satellite-Based Energy Balance for Mapping Evapotranspiration with Internalized Calibration (METRIC)—Applications. J. Irrig. Drain. Eng. 133, 395–406. https://doi.org/10.1061/(ASCE)0733-9437(2007)133:4(395)

Allen, R.G., Walter, I.A., Elliott, R.L., Howell, T.A., Itenfisu, D., Jensen, M.E., Snyder, R.L., 2005b. The ASCE Standardized Reference Evapotranspiration Equation. ASCE Publications.

Anderson, M.C., Kustas, W.P., Alfieri, J.G., Gao, F., Hain, C., Prueger, J.H., Evett, S., Colaizzi, P., Howell, T., Chávez, J.L., 2012. Mapping daily evapotranspiration at Landsat spatial scales during the BEAREX’08 field campaign. Adv. Water Resour., The Bushland Evapotranspiration and Agricultural Remote Sensing Experiment 2008 50, 162–177. https://doi.org/10.1016/j.advwatres.2012.06.005

Anderson, M.C., Kustas, W.P., Norman, J.M., Hain, C.R., Mecikalski, J.R., Schultz, L., González-Dugo, M.P., Cammalleri, C., d’Urso, G., Pimstein, A., Gao, F., 2011. Mapping daily evapotranspiration at field to continental scales using geostationary and polar orbiting satellite imagery. Hydrol Earth Syst Sci 15, 223–239. https://doi.org/10.5194/hess-15-223-2011

Bastiaanssen, W.G.M., 1998. Remote sensing in water resources management: the state of the art. Remote Sens. Water Resour. Manag. State Art.

Bastiaanssen, W.G.M., Menenti, M., Feddes, R.A., Holtslag, A.A.M., 1998. A remote sensing surface energy balance algorithm for land (SEBAL). 1. Formulation. J. Hydrol. 212, 198–212. https://doi.org/10.1016/S0022-1694(98)00253-4

Blankenau, P., 2017. Bias and Other Error in Gridded Weather Data Sets and Their Impacts on Estimating Reference Evapotranspiration. Civ. Eng. Theses Diss. Stud. Res.

Cosgrove, B.A., Lohmann, D., Mitchell, K.E., Houser, P.R., Wood, E.F., Schaake, J.C., Robock, A., Marshall, C., Sheffield, J., Duan, Q., Luo, L., Higgins, R.W., Pinker, R.T., Tarpley, J.D., Meng, J., 2003. Real-time and retrospective forcing in the North American Land Data Assimilation System (NLDAS) project. J. Geophys. Res. Atmospheres 108. https://doi.org/10.1029/2002JD003118

Courault, D., Seguin, B., Olioso, A., 2005. Review on estimation of evapotranspiration from remote sensing data: From empirical to numerical modeling approaches. Irrig. Drain. Syst. 19, 223–249. https://doi.org/10.1007/s10795-005-5186-0

Crago, R.D., 1996. Conservation and variability of the evaporative fraction during the daytime. J. Hydrol. 180, 173–194. https://doi.org/10.1016/0022-1694(95)02903-6

Geli, H.M.E., Neale, C.M.U., Verdin, J.P., 2017. Estimating Crop Water Use with Remote Sensing: Development of Guidelines and Specifications – Part 2: Evapotranspiration Model Intercomparison. US Geol. Surv. Sci. Investig. Rep. 2017 (under review).

Gonzalez-Dugo, M.P., Neale, C.M.U., Mateos, L., Kustas, W.P., Prueger, J.H., Anderson, M.C., Li, F., 2009. A comparison of operational remote sensing-based models for estimating crop evapotranspiration. Agric. For. Meteorol., Special Section on Water and

Carbon Dynamics in Selected Ecosystems in China 149, 1843–1853. https://doi.org/10.1016/j.agrformet.2009.06.012

Irmak, A., Allen, R.G., Kjaersgaard, J., Huntington, J., Kamble, B., Trezza, R., Ratcliffe, I., 2012. Operational Remote Sensing of ET and Challenges. https://doi.org/10.5772/25174

Irmak, A., Ratcliffe, I., Ranade, P., Hubbard, K.G., Singh, R.K., Kamble, B., Kjaersgaard, J., 2011. ESTIMATION OF LAND SURFACE EVAPOTRANSPIRATION WITH A SATELLITE REMOTE SENSING PROCEDURE. Gt. Plains Res. 21, 73–88.

Jensen, M.E., Allen, R.G., 2016. Evaporation, Evapotranspiration, and Irrigation Water Requirements. American Society of Civil Engineers.

Kalma, J.D., McVicar, T.R., McCabe, M.F., 2008. Estimating Land Surface Evaporation: A Review of Methods Using Remotely Sensed Surface Temperature Data. Surv. Geophys. 29, 421–469. https://doi.org/10.1007/s10712-008-9037-z

Kustas, W.P., Norman, J.M., 1996. Use of remote sensing for evapotranspiration monitoring over land surfaces. Hydrol. Sci. J. 41, 495–516. https://doi.org/10.1080/02626669609491522

Lewis, C.S., Geli, H.M.E., Neale, C.M.U., 2014. Comparison of the NLDAS Weather Forcing Model to Agrometeorological Measurements in the western United States. J. Hydrol. 510, 385–392. https://doi.org/10.1016/j.jhydrol.2013.12.040

Medellín-Azuara, J., Paw U, K.., Jin, Y., Lund, J.R., 2018. A Comparative Study for Estimating Crop Evapotranspiration in the Sacramento-San Joaquin Delta.

Morton, C.G., Huntington, J.L., Pohll, G.M., Allen, R.G., McGwire, K.C., Bassett, S.D., 2013. Assessing Calibration Uncertainty and Automation for Estimating Evapotranspiration from Agricultural Areas Using METRIC. JAWRA J. Am. Water Resour. Assoc. 49, 549–562. https://doi.org/10.1111/jawr.12054

Morton, F.I., 1983. Operational estimates of areal evapotranspiration and their significance to the science and practice of hydrology. J. Hydrol. 66, 1–76. https://doi.org/10.1016/0022-1694(83)90177-4

Perrier, A., 1982. Land surface processes: vegetation. In land surface processes in atmospheric general circulation models, Eagelson P (ed.). Cambridge University Press, Cambridge. 395–448. Cambridge University Press, Cambridge.

Saha, S., Moorthi, S., Pan, H.-L., Wu, X., Wang, Jiande, Nadiga, S., Tripp, P., Kistler, R., Woollen, J., Behringer, D., Liu, H., Stokes, D., Grumbine, R., Gayno, G., Wang, Jun, Hou, Y.-T., Chuang, H., Juang, H.-M.H., Sela, J., Iredell, M., Treadon, R., Kleist, D., Van Delst, P., Keyser, D., Derber, J., Ek, M., Meng, J., Wei, H., Yang, R., Lord, S., van den Dool, H., Kumar, A., Wang, W., Long, C., Chelliah, M., Xue, Y., Huang, B., Schemm, J.-K., Ebisuzaki, W., Lin, R., Xie, P., Chen, M., Zhou, S., Higgins, W., Zou, C.-Z., Liu, Q., Chen, Y., Han, Y., Cucurull, L., Reynolds, R.W., Rutledge, G., Goldberg, M., 2010. The NCEP Climate Forecast System Reanalysis. Bull. Am. Meteorol. Soc. 91, 1015–1058. https://doi.org/10.1175/2010BAMS3001.1

Saha, S., Moorthi, S., Wu, X., Wang, J., Nadiga, S., Tripp, P., Behringer, D., Hou, Y.-T., Chuang, H., Iredell, M., Ek, M., Meng, J., Yang, R., Mendez, M.P., van den Dool, H., Zhang, Q., Wang, W., Chen, M., Becker, E., 2013. The NCEP Climate Forecast System Version 2. J. Clim. 27, 2185–2208. https://doi.org/10.1175/JCLI-D-12-00823.1

Tasumi, M., Trezza, R., Allen, R.G., Wright, J.L., 2005. Operational aspects of satellite-based energy balance models for irrigated crops in the semi-arid U.S. Irrig. Drain. Syst. 19, 355–376. https://doi.org/10.1007/s10795-005-8138-9

Temesgen B., Allen R. G., Jensen D. T., 1999. Adjusting Temperature Parameters to Reflect Well-Watered Conditions. J. Irrig. Drain. Eng. 125, 26–33. https://doi.org/10.1061/(ASCE)0733-9437(1999)125:1(26)

Yuan, X., Wood, E.F., Luo, L., Pan, M., 2011. A first look at Climate Forecast System version 2 (CFSv2) for hydrological seasonal prediction. Geophys. Res. Lett. 38. https://doi.org/10.1029/2011GL047792

CHAPTER 5: SUMMARY AND CONCLUSIONS

5.1 Summary and Conclusion

In this study, different techniques were used to estimate ET_a at the field scale and also explored the relationships between ET_a and some key hydrological state variables (e.g., soil water content and groundwater). Novel proximal and remote sensing datasets were combined with in-situ sensors to investigate spatiotemporal changes in ET_a and what factors controlled it.

In chapter 2, the feasibility of using inverse vadose zone modeling for field ET_a estimation was investigated at a long-term agricultural monitoring site in eastern Nebraska. SWC data from both point sensors and the area-average were used to estimate ET_a. The point scale SWC data were measured by in-situ sensors, theta probes (TP), and the area-average SWC data were recorded by CRNP. In order to check the accuracy of the estimated values, the estimated ET_a were compared to the measured ET_a by an eddy-covariance tower at the same field. The results indicate reasonable estimates of daily and annual ET_a but with varied soil hydraulic function parameterizations. The varied soil hydraulic parameters were expected given the heterogeneity of soil texture at the site and consistent with the principle of equifinality in hydrologic systems. While this study focused on one particular site, the framework can be easily applied to other SWC monitoring networks across the globe.

In chapter 3, novel spatiotemporal datasets of ET_a, SWC, and DTWT using a combination of remote (METRIC model) and proximal sensing methods (fixed and roving CRNP) were generated in a well instrumented riparian study site in central Nebraska. ET_a

was estimated by applying METRIC model on Landsat images. Data from stationary and roving cosmic-ray neutron probes were used to generate spatial SWC maps. DTWT was made based on the groundwater data from a network of 16 observation wells. Comparison of the datasets reveal that SWC and ET_a were linearly correlated for shallow rooted vegetation at the study site. The correlation between DTWT and ET_a was weak but may be limited by the localized conditions of the groundwater observations. A simple statistical model of daily ET_a vs. the calculated daily ET_a from the commonly used cubic spline method indicate similar seasonal ET_a values in the wet conditions of 2015. Comparison of the two temporal interpolation methods in the drier conditions of 2016 indicate a 20% difference in seasonal ET_a. The difference underscores the need for better accounting for local state variable changes between the 16-day overpass of the Landsat 8 satellite.

In chapter 4, the functionality of automatically calibrated EEFlux was evaluated by comparing the EEFlux products to 58 existing manually calibrated METRIC images in nine different locations. The comparison results showed that EEFlux is able to calculate ET_rF and ET_a values in agricultural areas comparable to the ones from trained expert METRIC users. Based on the comparisons, the EEFlux automated calibration algorithm needs to be improved in order to be able to calculate ET_rF and ET_a in non-agricultural areas as good as manually calibrated METRIC ones. While EEFlux is still a work in progress, it could be used to quickly estimate ET_a for areas of interest but it is important to acknowledge and be aware of the biases due to the gridded weather data EEFlux is fed and be aware of the general variability and error expected in ET_rF and ET_a estimates.

5.2 Future Work

For future research, the following recommendations are suggested based upon the experience gained while carrying out this research:

- While the study in chapter 2 focused on one particular site, we believe the framework can be easily applied to other SWC monitoring networks across the globe, and in order to be more assured about the framework that would be ideal to evaluate the performance of framework elsewhere.
- In chapter 3, based on the results, SWC and ET_a were linearly correlated but the correlation between DTWT and ET_a was weak at the study site. The results can be time, therefore, repeating the same study at the study site seems essential. Also the results can be site specific and applying the same method elsewhere is desirable.
- Based on the comparisons, in chapter 4, the EEFlux automated calibration algorithm needs to be improved in order to be able to calculate ET_rF and ET_a in non-agricultural areas as good as manually calibrated METRIC ones. The differences between EEFlux and METRIC in non-agricultural areas could, in part, be the result of poor hot pixel selection and improvement in hot pixel selection might improve EEFlux functionality in non-agricultural areas

APPENDIX A: SUPPLEMENTAL TABLES

Supplemental Table 4.1. R^2 values for different products between EEFlux and METRIC by scene location and date for agricultural land uses.

R^2 (Agricultural Lands)												
Path	Row	Date	Satellite	T_s	Albedo	NDVI	Rn	G	H	ET_r	ET_rF	ET_a
29	31	6/28/2002	L5	1.00	0.98	0.99	0.72	0.87	0.94	---	0.96	0.95
29	31	8/15/2002	L5	1.00	0.95	0.99	0.29	0.88	0.73	---	0.94	0.91
29	31	9/8/2002	L7	0.98	0.96	0.99	0.61	0.66	0.90	---	0.93	0.88
29	32	5/3/2002	L7	0.98	0.98	0.99	0.79	0.03	0.83	---	0.87	0.87
29	32	6/28/2002	L5	1.00	0.99	0.99	0.86	0.82	0.92	---	0.97	0.91
29	32	8/15/2002	L5	1.00	0.97	1.00	0.66	0.84	0.87	---	0.97	0.95
29	32	9/8/2002	L7	0.99	0.97	0.99	0.69	0.57	0.93	---	0.95	0.94
30	31	5/2/2002	L5	0.97	0.90	0.97	0.62	0.75	0.53	---	0.65	0.64
30	31	6/11/2002	L7	0.99	0.96	0.96	0.87	0.31	0.91	---	0.92	0.90
30	31	7/29/2002	L7	0.98	0.88	0.96	0.83	0.44	0.94	---	0.95	0.95
30	31	9/15/2002	L7	0.97	0.95	0.94	0.74	0.71	0.54	---	0.81	0.54
30	32	5/2/2002	L5	0.99	0.91	0.96	0.75	0.14	0.84	---	0.86	0.85
30	32	6/11/2002	L7	0.99	0.95	0.93	0.87	0.08	0.95	---	0.94	0.88
30	32	7/29/2002	L7	1.00	0.93	0.99	0.91	0.86	0.98	---	0.98	0.98
30	32	9/15/2002	L7	0.98	0.95	0.94	0.79	0.75	0.75	---	0.87	0.72
37	30	7/15/2011	L5	0.98	0.85	0.86	0.10	0.71	0.52	---	0.29	0.26
37	30	7/23/2011	L7	0.99	0.99	0.96	0.26	0.77	0.48	---	0.64	0.46
37	30	8/16/2011	L5	1.00	0.99	0.99	0.91	0.63	0.80	---	0.95	0.92
37	30	9/1/2011	L5	1.00	0.97	0.99	0.61	0.61	0.73	---	0.87	0.82
37	30	9/25/2011	L7	1.00	0.96	0.98	0.84	0.33	0.81	---	0.93	0.89
37	31	7/15/2011	L5	1.00	1.00	0.98	0.43	0.85	0.83	---	0.81	0.75
37	31	7/23/2011	L7	1.00	1.00	0.99	0.61	0.79	0.80	---	0.90	0.88
37	31	8/16/2011	L5	1.00	0.99	0.99	0.93	0.79	0.95	---	0.96	0.96
37	31	9/1/2011	L5	1.00	0.99	0.99	0.68	0.70	0.88	---	0.89	0.86
39	37	1/26/2014	L8	1.00	0.98	0.98	0.79	0.50	0.99	---	0.93	0.91
39	37	2/11/2014	L8	1.00	0.99	0.98	0.85	0.53	0.98	---	0.96	0.93
39	37	3/15/2014	L8	1.00	0.99	1.00	0.86	0.33	0.92	---	0.91	0.81
39	37	3/31/2014	L8	1.00	0.99	1.00	0.94	0.63	0.99	---	0.98	0.96
39	37	4/16/2014	L8	1.00	0.99	1.00	0.96	0.48	0.99	---	0.97	0.96
39	37	5/2/2014	L8	1.00	0.99	1.00	0.94	0.17	0.96	---	0.93	0.90

Supplemental Table 4.1. (continued)

R^2 (Agricultural Lands)												
Path	Row	Date	Satellite	T_s	Albedo	NDVI	Rn	G	H	ET_r	ET_rF	ET_a
39	37	6/19/2014	L8	1.00	1.00	1.00	0.97	0.08	0.88	---	0.76	0.72
39	37	7/21/2014	L8	1.00	1.00	1.00	0.96	0.01	0.97	---	0.91	0.84
39	37	8/6/2014	L8	1.00	1.00	1.00	0.96	0.00	0.98	---	0.91	0.88
39	37	8/22/2014	L8	1.00	1.00	1.00	0.88	0.73	0.97	---	0.87	0.79
39	37	9/23/2014	L8	1.00	0.99	0.98	0.89	0.16	0.72	---	0.76	0.76
39	37	10/9/2014	L8	1.00	0.99	0.99	0.88	0.46	0.99	---	0.91	0.92
39	37	11/10/2014	L8	1.00	0.98	0.99	0.76	0.59	0.98	---	0.95	0.95
40	30	3/19/2016	L7	0.99	0.94	0.99	0.64	0.31	0.72	---	0.62	0.53
40	30	4/20/2016	L7	1.00	0.96	1.00	0.92	0.75	0.99	---	0.97	0.92
40	30	5/30/2016	L8	1.00	0.97	1.00	0.94	0.53	0.90	---	0.95	0.89
40	30	6/7/2016	L7	0.99	0.94	0.99	0.94	0.72	0.98	---	0.94	0.80
40	30	6/23/2016	L7	0.99	0.97	0.99	0.94	0.27	0.95	---	0.94	0.88
40	30	7/1/2016	L8	0.99	0.95	0.99	0.85	0.76	0.92	---	0.93	0.85
40	30	7/9/2016	L7	0.99	0.97	0.99	0.93	0.43	0.96	---	0.95	0.88
40	30	7/25/2016	L7	1.00	0.96	1.00	0.95	0.65	0.99	---	0.96	0.89
40	30	8/2/2016	L8	0.99	0.96	0.98	0.90	0.21	0.90	---	0.84	0.81
40	30	8/10/2016	L7	1.00	0.99	1.00	0.96	0.72	0.96	---	0.96	0.91
40	30	8/18/2016	L8	0.99	0.95	0.99	0.92	0.06	0.98	---	0.94	0.89
40	30	9/11/2016	L7	0.98	0.95	0.99	0.81	0.10	0.88	---	0.82	0.71
40	30	9/19/2016	L8	1.00	0.94	1.00	0.83	0.67	0.96	---	0.95	0.90
40	30	9/27/2016	L7	0.99	0.94	1.00	0.73	0.66	0.97	---	0.93	0.73
40	30	10/21/2016	L8	0.98	0.93	1.00	0.40	0.85	0.93	---	0.75	0.36
45	31	4/30/2004	L5	1.00	0.99	0.98	0.89	0.72	0.79	---	0.92	0.90
45	31	6/1/2004	L5	0.99	0.95	0.97	0.79	0.81	0.74	---	0.92	0.91
45	31	8/4/2004	L5	1.00	0.99	0.99	0.90	0.77	0.93	---	0.96	0.93
45	31	8/20/2004	L5	1.00	0.98	0.99	0.90	0.85	0.96	---	0.98	0.96
45	31	9/21/2004	L5	0.99	0.98	0.99	0.83	0.79	0.87	---	0.95	0.94
45	31	10/7/2004	L5	0.99	0.98	0.96	0.85	0.69	0.93	---	0.95	0.94

Supplemental Table 4.2. R^2 values for different products between EEFlux and METRIC by scene location and date for non-agricultural land uses.

R^2 (Non-Agricultural Lands)												
Path	Row	Date	Satellite	T_s	Albedo	NDVI	Rn	G	H	ET_r	ET_rF	ET_a
29	31	6/28/2002	L5	1.00	0.95	1.00	0.71	0.69	0.90	---	0.84	0.83
29	31	8/15/2002	L5	1.00	0.96	0.99	0.67	0.65	0.83	---	0.83	0.84
29	31	9/8/2002	L7	0.99	0.94	0.99	0.54	0.52	0.92	---	0.83	0.81
29	32	5/3/2002	L7	0.97	0.98	0.99	0.69	0.67	0.11	---	0.17	0.17
29	32	6/28/2002	L5	1.00	0.95	1.00	0.77	0.39	0.82	---	0.68	0.65
29	32	8/15/2002	L5	1.00	0.95	0.99	0.61	0.37	0.85	---	0.73	0.74
29	32	9/8/2002	L7	0.98	0.93	0.99	0.44	0.35	0.77	---	0.62	0.62
30	31	5/2/2002	L5	0.93	0.59	0.85	0.02	0.17	0.01	---	0.12	0.12
30	31	6/11/2002	L7	0.98	0.81	0.91	0.50	0.38	0.89	---	0.87	0.86
30	31	7/29/2002	L7	0.94	0.73	0.79	0.47	0.00	0.86	---	0.83	0.83
30	31	9/15/2002	L7	0.94	0.64	0.93	0.14	0.33	0.85	---	0.67	0.70
30	32	5/2/2002	L5	0.97	0.63	0.83	0.08	0.29	0.08	---	0.18	0.16
30	32	6/11/2002	L7	0.97	0.72	0.89	0.42	0.18	0.75	---	0.75	0.76
30	32	7/29/2002	L7	0.96	0.69	0.91	0.41	0.00	0.91	---	0.75	0.75
30	32	9/15/2002	L7	0.97	0.65	0.95	0.26	0.21	0.74	---	0.49	0.49
37	30	7/15/2011	L5	1.00	1.00	0.99	0.91	0.38	0.68	---	0.78	0.79
37	30	7/23/2011	L7	1.00	0.99	0.99	0.87	0.64	0.30	---	0.71	0.69
37	30	8/16/2011	L5	1.00	0.99	0.99	0.94	0.36	0.60	---	0.84	0.83
37	30	9/1/2011	L5	1.00	0.99	0.98	0.79	0.44	0.32	---	0.71	0.72
37	30	9/25/2011	L7	0.99	0.98	0.97	0.76	0.46	0.47	---	0.69	0.62
37	31	7/15/2011	L5	1.00	0.99	1.00	0.93	0.53	0.76	---	0.85	0.85
37	31	7/23/2011	L7	1.00	0.99	1.00	0.92	0.55	0.55	---	0.85	0.84
37	31	8/16/2011	L5	1.00	0.98	0.99	0.83	0.18	0.65	---	0.64	0.57
37	31	9/1/2011	L5	1.00	0.99	0.99	0.86	0.17	0.80	---	0.75	0.78
39	37	1/26/2014	L8	1.00	0.96	0.56	0.71	0.37	0.76	---	0.38	0.38
39	37	2/11/2014	L8	1.00	0.97	0.69	0.66	0.34	0.60	---	0.57	0.58
39	37	3/15/2014	L8	1.00	0.96	0.86	0.63	0.25	0.42	---	0.10	0.09
39	37	3/31/2014	L8	1.00	0.94	0.93	0.70	0.16	0.79	---	0.33	0.33
39	37	4/16/2014	L8	1.00	0.96	0.96	0.71	0.02	0.44	---	0.24	0.24
39	37	5/2/2014	L8	1.00	0.97	0.94	0.79	0.17	0.39	---	0.27	0.26

Supplemental Table 4.2. (continued)

R2 (Non-Agricultural Lands)												
Path	Row	Date	Satellite	T_s	Albedo	NDVI	Rn	G	H	ET_r	ET_rF	ET_a
39	37	6/19/2014	L8	1.00	0.98	0.93	0.82	0.02	0.25	---	0.12	0.12
39	37	7/21/2014	L8	1.00	0.98	0.96	0.83	0.12	0.65	---	0.32	0.31
39	37	8/6/2014	L8	1.00	0.98	0.88	0.77	0.08	0.78	---	0.41	0.37
39	37	8/22/2014	L8	1.00	0.97	0.95	0.68	0.21	0.82	---	0.64	0.77
39	37	9/23/2014	L8	1.00	0.95	0.86	0.66	0.11	0.48	---	0.35	0.35
39	37	10/9/2014	L8	1.00	0.97	0.88	0.76	0.02	0.92	---	0.73	0.72
39	37	11/10/2014	L8	1.00	0.92	0.90	0.66	0.51	0.88	---	0.33	0.33
40	30	3/19/2016	L7	0.98	0.94	0.97	0.62	0.23	0.83	---	0.48	0.49
40	30	4/20/2016	L7	0.98	0.92	0.96	0.69	0.46	0.85	---	0.72	0.73
40	30	5/30/2016	L8	1.00	0.97	0.97	0.69	0.37	0.68	---	0.65	0.63
40	30	6/7/2016	L7	0.99	0.97	0.96	0.90	0.25	0.96	---	0.88	0.89
40	30	6/23/2016	L7	0.98	0.89	0.95	0.80	0.15	0.74	---	0.62	0.62
40	30	7/1/2016	L8	0.99	0.87	0.98	0.83	0.32	0.75	---	0.60	0.61
40	30	7/9/2016	L7	0.98	0.84	0.91	0.81	0.12	0.62	---	0.61	0.60
40	30	7/25/2016	L7	0.99	0.88	0.98	0.84	0.22	0.93	---	0.85	0.84
40	30	8/2/2016	L8	0.99	0.91	0.92	0.76	0.02	0.76	---	0.77	0.77
40	30	8/10/2016	L7	1.00	0.97	0.99	0.89	0.10	0.94	---	0.88	0.88
40	30	8/18/2016	L8	0.99	0.91	0.97	0.76	0.12	0.94	---	0.75	0.77
40	30	9/11/2016	L7	0.98	0.93	0.92	0.63	0.04	0.82	---	0.55	0.53
40	30	9/19/2016	L8	0.99	0.93	0.99	0.58	0.21	0.82	---	0.81	0.81
40	30	9/27/2016	L7	0.97	0.90	0.95	0.60	0.21	0.86	---	0.57	0.60
40	30	10/21/2016	L8	0.96	0.82	0.97	0.30	0.56	0.70	---	0.21	0.19
45	31	4/30/2004	L5	0.99	0.97	0.96	0.75	0.50	0.21	---	0.31	0.33
45	31	6/1/2004	L5	1.00	0.96	0.98	0.84	0.74	0.02	---	0.41	0.41
45	31	8/4/2004	L5	1.00	0.99	0.95	0.80	0.46	0.44	---	0.59	0.59
45	31	8/20/2004	L5	1.00	0.97	0.98	0.75	0.30	0.58	---	0.63	0.62
45	31	9/21/2004	L5	1.00	0.96	0.97	0.76	0.59	0.18	---	0.42	0.47
45	31	10/7/2004	L5	1.00	0.97	0.93	0.68	0.64	0.39	---	0.43	0.45

Supplemental Table 4.3. Slope values for different products between EEFlux and METRIC by scene location and date for agricultural land uses.

Slope (Agricultural Lands)												
Path	Row	Date	Satellite	T_s	Albedo	NDVI	Rn	G	H	ET_r	ET_rF	ET_a
29	31	6/28/2002	L5	1.00	0.99	1.15	1.03	1.55	1.35	1.14	0.82	0.94
29	31	8/15/2002	L5	1.00	1.01	1.15	1.01	1.44	2.07	1.09	0.74	0.80
29	31	9/8/2002	L7	1.00	1.00	1.22	1.02	1.45	0.99	1.15	0.88	1.01
29	32	5/3/2002	L7	1.00	1.00	1.15	0.98	1.38	1.25	0.98	0.53	0.52
29	32	6/28/2002	L5	1.00	0.98	1.14	1.04	1.57	1.00	1.30	1.00	1.29
29	32	8/15/2002	L5	1.00	0.99	1.14	0.99	1.42	1.57	1.14	0.75	0.85
29	32	9/8/2002	L7	1.00	0.99	1.20	1.03	1.44	0.96	1.27	0.91	1.15
30	31	5/2/2002	L5	1.00	1.01	1.16	0.98	1.70	1.37	0.94	0.55	0.51
30	31	6/11/2002	L7	1.00	1.00	1.14	0.99	1.55	1.39	0.92	0.70	0.64
30	31	7/29/2002	L7	1.00	0.99	1.14	1.05	1.55	1.15	1.14	0.89	1.01
30	31	9/15/2002	L7	1.00	1.05	1.21	0.97	1.33	1.75	1.05	0.85	0.87
30	32	5/2/2002	L5	1.00	1.00	1.15	0.99	1.45	1.01	0.92	0.81	0.74
30	32	6/11/2002	L7	1.00	1.01	1.16	1.01	1.38	1.09	0.97	0.80	0.78
30	32	7/29/2002	L7	1.00	0.99	1.12	1.06	1.64	1.31	1.11	1.00	1.10
30	32	9/15/2002	L7	1.00	1.04	1.20	0.99	1.36	1.50	0.98	1.02	0.99
37	30	7/15/2011	L5	1.00	1.01	1.13	1.07	1.46	1.95	1.06	0.96	1.01
37	30	7/23/2011	L7	1.00	1.02	1.14	1.06	1.43	2.39	0.95	0.91	0.86
37	30	8/16/2011	L5	1.00	1.01	1.13	0.97	1.31	1.51	0.94	0.82	0.77
37	30	9/1/2011	L5	1.00	1.01	1.15	1.01	1.32	1.44	0.90	1.03	0.91
37	30	9/25/2011	L7	1.00	1.04	1.22	0.97	1.14	0.95	1.03	1.05	1.08
37	31	7/15/2011	L5	1.00	1.01	1.10	1.06	1.52	1.68	1.05	1.00	1.05
37	31	7/23/2011	L7	1.00	1.02	1.13	1.05	1.41	1.52	0.95	1.02	0.97
37	31	8/16/2011	L5	1.00	1.01	1.11	1.01	1.29	1.18	0.94	1.13	1.06
37	31	9/1/2011	L5	1.00	1.01	1.14	1.03	1.51	1.36	0.92	1.03	0.95
39	37	1/26/2014	L8	1.00	1.00	1.21	1.03	1.21	0.77	1.27	1.28	1.53
39	37	2/11/2014	L8	1.00	0.99	1.17	1.04	1.38	0.88	1.39	1.01	1.32
39	37	3/15/2014	L8	1.00	0.99	1.11	1.04	1.29	0.85	1.60	1.01	1.49
39	37	3/31/2014	L8	1.00	0.99	1.09	1.04	1.22	0.96	1.32	1.04	1.26
39	37	4/16/2014	L8	1.00	0.99	1.07	1.05	1.26	1.02	1.31	0.95	1.14
39	37	5/2/2014	L8	1.00	0.99	1.04	1.05	1.24	1.08	1.31	0.79	0.90

Supplemental Table 4.3. (continued)

Slope (Agricultural Lands)												
Path	Row	Date	Satellite	T_s	Albedo	NDVI	Rn	G	H	ET_r	ET_rF	ET_a
39	37	6/19/2014	L8	1.00	0.99	1.00	1.05	1.33	1.03	1.14	0.72	0.75
39	37	7/21/2014	L8	1.00	0.99	1.00	1.05	1.31	0.82	1.13	1.06	1.03
39	37	8/6/2014	L8	1.00	0.99	1.01	1.06	1.67	1.10	0.96	0.76	0.71
39	37	8/22/2014	L8	1.00	0.99	1.08	1.04	1.92	0.39	1.20	0.96	1.15
39	37	9/23/2014	L8	1.00	1.00	1.08	1.05	1.70	1.53	1.06	0.57	0.60
39	37	10/9/2014	L8	1.00	1.00	1.14	1.06	1.58	0.73	1.19	1.09	1.30
39	37	11/10/2014	L8	1.00	1.00	1.19	1.05	1.54	1.15	1.20	0.96	1.16
40	30	3/19/2016	L7	1.00	0.99	1.00	0.99	1.58	1.17	1.36	0.85	1.13
40	30	4/20/2016	L7	1.00	0.99	1.00	1.02	1.21	0.94	1.27	1.07	1.23
40	30	5/30/2016	L8	1.00	1.00	1.00	1.00	1.27	0.79	1.05	0.96	0.91
40	30	6/7/2016	L7	1.00	1.00	1.00	1.01	1.66	0.76	1.18	0.97	1.12
40	30	6/23/2016	L7	1.00	1.00	1.00	1.01	1.57	0.60	1.17	1.01	1.10
40	30	7/1/2016	L8	1.00	0.99	1.00	1.03	1.67	0.63	1.27	1.03	1.30
40	30	7/9/2016	L7	1.00	0.99	1.00	1.03	1.65	0.48	1.29	0.97	1.20
40	30	7/25/2016	L7	1.00	0.99	1.00	1.01	1.90	0.66	1.31	0.95	1.24
40	30	8/2/2016	L8	1.00	1.00	0.99	1.00	2.12	1.12	1.16	0.79	0.88
40	30	8/10/2016	L7	1.00	0.99	1.00	0.99	1.81	0.77	1.19	0.86	1.01
40	30	8/18/2016	L8	1.00	0.99	0.99	1.03	2.09	0.75	1.15	0.95	1.06
40	30	9/11/2016	L7	1.00	0.99	0.99	1.02	1.43	0.70	1.37	1.10	1.37
40	30	9/19/2016	L8	1.00	0.99	1.00	1.02	1.43	0.75	1.34	0.98	1.29
40	30	9/27/2016	L7	1.00	0.97	1.00	1.04	1.99	1.52	0.88	0.90	0.80
40	30	10/21/2016	L8	1.00	0.98	0.99	1.05	1.79	0.77	1.65	1.00	1.63
45	31	4/30/2004	L5	1.00	0.99	1.13	0.97	1.36	1.04	1.23	0.84	1.03
45	31	6/1/2004	L5	1.00	1.00	1.10	0.99	1.24	1.01	0.99	1.04	1.03
45	31	8/4/2004	L5	1.00	0.99	1.11	1.01	1.33	1.17	1.14	0.92	1.04
45	31	8/20/2004	L5	1.00	0.99	1.12	1.01	1.07	0.96	1.32	1.00	1.32
45	31	9/21/2004	L5	1.00	0.98	1.16	1.07	1.29	1.00	1.15	1.06	1.21
45	31	10/7/2004	L5	1.00	0.97	1.22	1.09	1.44	1.14	1.19	1.06	1.26

Supplemental Table 4.4. Slope values for different products between EEFlux and METRIC by scene location and date for non-agricultural land uses.

Slope (Non-Agricultural Lands)												
Path	Row	Date	Satellite	T_s	Albedo	NDVI	Rn	G	H	ET_r	ET_rF	ET_a
29	31	6/28/2002	L5	1.00	0.99	1.16	1.02	1.52	1.59	1.16	0.64	0.74
29	31	8/15/2002	L5	1.00	0.99	1.21	0.99	1.24	1.38	1.08	0.58	0.62
29	31	9/8/2002	L7	1.00	0.99	1.23	1.02	1.23	1.16	1.19	0.63	0.72
29	32	5/3/2002	L7	1.00	1.00	1.15	0.98	1.21	1.40	0.99	0.28	0.28
29	32	6/28/2002	L5	1.00	0.98	1.15	1.04	1.43	1.06	1.33	0.76	0.99
29	32	8/15/2002	L5	1.00	0.99	1.21	0.98	1.26	1.34	1.14	0.45	0.51
29	32	9/8/2002	L7	1.00	0.99	1.22	1.03	1.19	1.11	1.28	0.62	0.79
30	31	5/2/2002	L5	1.00	0.99	1.15	0.99	1.60	1.90	0.93	0.17	0.16
30	31	6/11/2002	L7	1.00	1.01	1.14	1.00	1.54	1.82	0.94	0.54	0.49
30	31	7/29/2002	L7	1.00	0.99	1.16	1.06	1.52	1.33	1.14	0.68	0.77
30	31	9/15/2002	L7	1.00	1.03	1.22	0.97	1.47	1.83	1.13	0.35	0.36
30	32	5/2/2002	L5	1.00	1.00	1.14	0.99	1.52	1.26	0.91	0.52	0.47
30	32	6/11/2002	L7	1.00	1.00	1.15	1.02	1.51	1.43	1.04	0.57	0.58
30	32	7/29/2002	L7	1.00	0.99	1.15	1.07	1.53	1.26	1.11	0.74	0.82
30	32	9/15/2002	L7	1.00	1.01	1.22	1.00	1.45	1.38	1.08	0.51	0.53
37	30	7/15/2011	L5	1.00	1.01	1.14	0.99	1.46	1.53	1.02	0.50	0.50
37	30	7/23/2011	L7	1.00	1.02	1.18	0.99	1.19	1.44	0.90	0.63	0.56
37	30	8/16/2011	L5	1.00	1.01	1.18	0.98	1.23	1.27	0.89	0.66	0.56
37	30	9/1/2011	L5	1.00	1.01	1.20	1.00	1.17	1.21	0.85	0.61	0.51
37	30	9/25/2011	L7	1.00	1.03	1.33	0.97	1.02	0.88	0.99	1.05	0.99
37	31	7/15/2011	L5	1.00	1.00	1.11	0.99	1.34	1.40	1.03	0.55	0.53
37	31	7/23/2011	L7	1.00	1.02	1.16	0.99	1.05	1.09	0.96	0.71	0.61
37	31	8/16/2011	L5	1.00	1.01	1.11	1.01	0.93	0.80	0.93	1.28	1.10
37	31	9/1/2011	L5	1.00	1.01	1.16	1.03	1.25	1.20	0.95	0.64	0.55
39	37	1/26/2014	L8	1.00	1.00	1.17	1.02	0.91	0.62	1.19	1.31	1.54
39	37	2/11/2014	L8	1.00	0.99	1.11	1.03	1.31	1.07	1.36	1.02	1.36
39	37	3/15/2014	L8	1.00	0.99	1.03	1.04	0.84	0.75	1.36	0.74	0.98
39	37	3/31/2014	L8	1.00	0.99	0.99	1.05	0.91	0.87	1.14	0.87	0.98
39	37	4/16/2014	L8	1.00	0.99	0.95	1.06	0.90	0.79	1.16	0.90	1.03
39	37	5/2/2014	L8	1.00	0.99	0.93	1.04	0.87	0.77	1.16	0.98	1.14

Supplemental Table 4.4. (continued)

Slope (Non-Agricultural Lands)												
Path	Row	Date	Satellite	T_s	Albedo	NDVI	Rn	G	H	ET_r	ET_rF	ET_a
39	37	6/19/2014	L8	1.00	0.99	0.90	1.05	0.93	0.72	1.03	0.86	0.88
39	37	7/21/2014	L8	1.00	1.00	0.94	1.04	0.82	0.68	0.95	1.37	1.30
39	37	8/6/2014	L8	1.00	0.99	0.91	1.06	1.08	0.84	0.94	0.99	0.90
39	37	8/22/2014	L8	1.00	0.99	1.00	1.04	1.43	0.62	1.24	0.96	1.20
39	37	9/23/2014	L8	1.00	0.99	0.98	1.05	1.14	0.99	1.08	0.50	0.53
39	37	10/9/2014	L8	1.00	1.00	1.04	1.05	1.23	0.81	1.21	0.59	0.70
39	37	11/10/2014	L8	1.00	0.97	1.16	1.07	1.23	1.21	1.25	0.29	0.35
40	30	3/19/2016	L7	1.00	0.99	1.00	0.98	1.53	1.15	1.37	0.47	0.64
40	30	4/20/2016	L7	1.00	1.00	1.00	1.01	1.62	0.92	1.00	1.32	1.33
40	30	5/30/2016	L8	1.00	1.00	1.00	0.99	1.40	0.95	0.88	1.24	1.12
40	30	6/7/2016	L7	1.00	1.00	1.00	1.01	1.50	0.84	1.12	1.02	1.13
40	30	6/23/2016	L7	1.00	1.00	1.00	1.00	1.23	0.85	1.06	1.18	1.32
40	30	7/1/2016	L8	1.00	1.00	0.99	1.02	1.29	0.67	1.17	1.27	1.59
40	30	7/9/2016	L7	1.00	0.99	0.99	1.02	1.32	0.81	1.23	1.38	1.68
40	30	7/25/2016	L7	1.00	0.99	1.00	1.01	1.43	0.88	1.25	0.84	1.06
40	30	8/2/2016	L8	1.00	0.99	0.99	1.00	1.44	0.97	1.14	0.72	0.80
40	30	8/10/2016	L7	1.00	0.99	0.99	0.98	1.60	0.90	1.15	0.81	0.93
40	30	8/18/2016	L8	1.00	0.99	0.98	1.03	2.14	0.71	1.12	0.97	1.09
40	30	9/11/2016	L7	1.00	0.99	0.99	1.02	1.22	0.73	1.18	0.96	1.17
40	30	9/19/2016	L8	1.00	0.99	0.99	1.02	1.48	0.99	1.18	0.80	0.98
40	30	9/27/2016	L7	1.00	0.98	0.99	1.02	2.13	1.35	0.92	0.81	0.74
40	30	10/21/2016	L8	1.00	0.99	0.99	1.04	1.87	1.00	1.61	0.63	1.02
45	31	4/30/2004	L5	1.00	0.99	1.24	1.00	1.18	0.96	1.24	0.69	0.85
45	31	6/1/2004	L5	1.00	1.00	1.20	1.00	1.07	1.02	0.99	0.72	0.70
45	31	8/4/2004	L5	1.00	0.99	1.23	1.02	1.13	1.06	1.18	0.68	0.79
45	31	8/20/2004	L5	1.00	0.99	1.25	1.04	1.06	0.96	1.33	0.84	1.10
45	31	9/21/2004	L5	1.00	0.98	1.35	1.09	1.24	0.96	1.14	0.73	0.83
45	31	10/7/2004	L5	1.00	0.97	1.45	1.12	1.21	0.94	1.17	0.59	0.67

Supplemental Table 4.5. RMSE values for different products between EEFlux and METRIC by scene location and date for agricultural land uses.

RMSE (Agricultural Lands)												
Path	Row	Date	Satellite	T_s	Albedo	NDVI	Rn	G	H	ET_r	ET_rF	ET_a
29	31	6/28/2002	L5	0.20	0.00	0.08	25.41	33.69	44.75	---	0.15	0.91
29	31	8/15/2002	L5	0.16	0.00	0.10	20.16	21.25	158.87	---	0.21	1.19
29	31	9/8/2002	L7	0.51	0.00	0.10	19.53	31.35	23.49	---	0.08	0.55
29	32	5/3/2002	L7	0.43	0.00	0.03	16.69	45.08	68.84	---	0.22	1.72
29	32	6/28/2002	L5	0.16	0.00	0.08	27.06	33.06	25.68	---	0.03	2.14
29	32	8/15/2002	L5	0.12	0.00	0.09	18.24	25.00	142.90	---	0.21	0.94
29	32	9/8/2002	L7	0.50	0.00	0.09	20.80	31.75	20.93	---	0.06	0.88
30	31	5/2/2002	L5	0.28	0.01	0.04	21.08	66.38	87.71	---	0.42	2.45
30	31	6/11/2002	L7	0.51	0.01	0.05	15.56	48.52	76.89	---	0.19	2.14
30	31	7/29/2002	L7	0.72	0.01	0.06	30.84	43.17	34.89	---	0.09	0.67
30	31	9/15/2002	L7	0.65	0.01	0.13	24.29	23.38	80.85	---	0.19	1.00
30	32	5/2/2002	L5	0.27	0.01	0.04	18.88	50.51	10.53	---	0.14	0.96
30	32	6/11/2002	L7	0.56	0.01	0.06	15.15	41.16	25.71	---	0.11	1.17
30	32	7/29/2002	L7	0.57	0.01	0.08	37.45	34.85	58.57	---	0.06	0.83
30	32	9/15/2002	L7	0.67	0.01	0.12	16.91	23.12	61.74	---	0.08	0.53
37	30	7/15/2011	L5	0.46	0.01	0.09	61.50	29.97	85.92	---	0.11	1.02
37	30	7/23/2011	L7	0.60	0.00	0.10	49.89	25.75	164.77	---	0.11	1.40
37	30	8/16/2011	L5	0.19	0.00	0.08	20.57	25.58	108.36	---	0.15	1.45
37	30	9/1/2011	L5	0.17	0.00	0.07	27.28	29.04	127.24	---	0.09	0.86
37	30	9/25/2011	L7	0.50	0.01	0.09	21.65	20.13	27.33	---	0.08	0.57
37	31	7/15/2011	L5	0.18	0.00	0.07	52.40	33.04	89.19	---	0.10	1.12
37	31	7/23/2011	L7	0.53	0.00	0.08	46.82	30.73	109.26	---	0.08	0.81
37	31	8/16/2011	L5	0.19	0.00	0.07	14.42	27.81	75.11	---	0.13	0.64
37	31	9/1/2011	L5	0.28	0.00	0.07	30.68	37.73	70.52	---	0.10	0.88
39	37	1/26/2014	L8	1.15	0.01	0.10	20.04	26.63	42.13	---	0.26	1.27
39	37	2/11/2014	L8	1.01	0.01	0.08	20.82	32.15	20.43	---	0.08	1.05
39	37	3/15/2014	L8	0.73	0.00	0.04	23.46	42.46	48.49	---	0.09	1.87
39	37	3/31/2014	L8	0.59	0.00	0.05	26.29	37.81	25.18	---	0.07	1.52
39	37	4/16/2014	L8	0.29	0.00	0.03	28.37	43.91	65.17	---	0.07	0.98
39	37	5/2/2014	L8	0.21	0.00	0.02	27.07	53.77	76.61	---	0.10	0.75

Supplemental Table 4.5. (continued)

RMSE (Agricultural Lands)												
Path	Row	Date	Satellite	T_s	Albedo	NDVI	Rn	G	H	ET_r	ET_rF	ET_a
39	37	6/19/2014	L8	0.11	0.00	0.01	26.77	71.39	91.83	---	0.14	1.32
39	37	7/21/2014	L8	0.08	0.00	0.01	23.87	64.76	52.76	---	0.09	1.32
39	37	8/6/2014	L8	0.13	0.00	0.02	30.60	68.19	67.85	---	0.14	1.62
39	37	8/22/2014	L8	0.72	0.00	0.04	25.95	63.76	114.64	---	0.07	0.83
39	37	9/23/2014	L8	0.20	0.00	0.03	24.23	56.93	118.48	---	0.20	1.38
39	37	10/9/2014	L8	0.69	0.00	0.06	28.30	46.50	43.46	---	0.12	1.15
39	37	11/10/2014	L8	0.76	0.00	0.09	23.11	31.44	21.74	---	0.10	0.70
40	30	3/19/2016	L7	0.34	0.01	0.01	20.39	49.80	48.02	---	0.16	0.68
40	30	4/20/2016	L7	0.40	0.01	0.02	18.39	31.34	26.54	---	0.09	1.05
40	30	5/30/2016	L8	0.69	0.01	0.01	14.28	45.59	72.36	---	0.12	1.33
40	30	6/7/2016	L7	0.75	0.01	0.02	19.31	54.01	41.17	---	0.07	1.27
40	30	6/23/2016	L7	0.62	0.01	0.02	17.11	55.09	77.38	---	0.10	1.61
40	30	7/1/2016	L8	0.41	0.01	0.02	24.98	41.61	59.72	---	0.10	1.97
40	30	7/9/2016	L7	0.59	0.01	0.02	22.50	52.77	110.26	---	0.08	1.55
40	30	7/25/2016	L7	0.46	0.01	0.02	16.50	49.37	54.92	---	0.07	1.72
40	30	8/2/2016	L8	0.43	0.01	0.01	17.62	66.00	72.68	---	0.11	0.82
40	30	8/10/2016	L7	0.27	0.01	0.01	15.85	50.49	41.46	---	0.13	0.63
40	30	8/18/2016	L8	0.75	0.01	0.02	21.94	60.53	38.78	---	0.08	0.78
40	30	9/11/2016	L7	0.45	0.01	0.01	20.70	52.26	71.32	---	0.13	1.67
40	30	9/19/2016	L8	0.49	0.01	0.01	20.03	33.36	45.32	---	0.08	1.11
40	30	9/27/2016	L7	0.31	0.01	0.02	23.93	50.04	51.78	---	0.11	0.91
40	30	10/21/2016	L8	0.96	0.01	0.01	27.50	39.75	33.83	---	0.10	1.42
45	31	4/30/2004	L5	0.46	0.00	0.07	25.59	35.40	20.30	---	0.15	0.71
45	31	6/1/2004	L5	0.74	0.01	0.08	21.28	29.98	41.15	---	0.09	0.67
45	31	8/4/2004	L5	0.43	0.01	0.07	17.42	30.52	41.31	---	0.09	0.59
45	31	8/20/2004	L5	0.39	0.01	0.07	17.42	14.60	13.75	---	0.05	1.34
45	31	9/21/2004	L5	0.39	0.01	0.08	34.92	26.41	16.91	---	0.08	0.56
45	31	10/7/2004	L5	0.35	0.01	0.10	35.94	28.04	23.01	---	0.10	0.64

Supplemental Table 4.6. RMSE values for different products between EEFlux and METRIC by scene location and date for non-agricultural land uses.

RMSE (Non-Agricultural Lands)												
Path	Row	Date	Satellite	T_s	Albedo	NDVI	Rn	G	H	ET_r	ET_rF	ET_a
29	31	6/28/2002	L5	0.14	0.00	0.08	19.97	38.46	77.67	---	0.28	2.10
29	31	8/15/2002	L5	0.12	0.00	0.08	21.74	25.43	98.31	---	0.23	1.54
29	31	9/8/2002	L7	0.51	0.01	0.09	22.68	24.92	39.06	---	0.16	1.23
29	32	5/3/2002	L7	0.47	0.00	0.05	21.47	40.66	124.27	---	0.36	2.79
29	32	6/28/2002	L5	0.11	0.01	0.07	26.06	39.20	29.61	---	0.19	1.59
29	32	8/15/2002	L5	0.04	0.01	0.06	22.56	34.50	86.03	---	0.25	1.60
29	32	9/8/2002	L7	0.48	0.01	0.08	25.58	26.22	38.67	---	0.14	1.12
30	31	5/2/2002	L5	0.36	0.01	0.06	32.18	58.14	200.45	---	0.74	4.10
30	31	6/11/2002	L7	0.57	0.01	0.06	23.31	45.16	122.26	---	0.32	3.26
30	31	7/29/2002	L7	0.70	0.01	0.05	38.87	44.33	66.50	---	0.15	0.96
30	31	9/15/2002	L7	0.61	0.01	0.09	35.88	35.33	115.57	---	0.50	2.40
30	32	5/2/2002	L5	0.37	0.01	0.05	34.96	55.34	70.59	---	0.37	2.21
30	32	6/11/2002	L7	0.62	0.01	0.06	28.84	47.76	89.12	---	0.25	2.24
30	32	7/29/2002	L7	0.62	0.01	0.04	43.00	45.30	50.66	---	0.11	0.70
30	32	9/15/2002	L7	0.68	0.01	0.08	37.22	36.26	66.89	---	0.32	1.53
37	30	7/15/2011	L5	0.13	0.00	0.05	20.22	47.45	123.81	---	0.28	2.46
37	30	7/23/2011	L7	0.56	0.00	0.08	29.26	27.37	154.83	---	0.26	2.49
37	30	8/16/2011	L5	0.15	0.00	0.07	20.44	32.19	92.28	---	0.18	1.61
37	30	9/1/2011	L5	0.12	0.00	0.06	27.39	27.19	105.08	---	0.14	1.35
37	30	9/25/2011	L7	0.43	0.01	0.06	31.29	11.27	38.09	---	0.08	0.44
37	31	7/15/2011	L5	0.10	0.00	0.04	19.50	38.76	109.43	---	0.25	2.15
37	31	7/23/2011	L7	0.41	0.00	0.04	16.01	16.01	55.65	---	0.10	1.02
37	31	8/16/2011	L5	0.04	0.00	0.02	18.34	16.52	69.39	---	0.15	1.02
37	31	9/1/2011	L5	0.13	0.00	0.03	23.10	32.24	59.86	---	0.10	0.89
39	37	1/26/2014	L8	1.14	0.01	0.04	30.61	16.00	91.47	---	0.18	0.64
39	37	2/11/2014	L8	1.01	0.01	0.03	39.72	26.90	25.29	---	0.09	0.54
39	37	3/15/2014	L8	0.74	0.01	0.02	41.65	29.20	94.04	---	0.07	0.75
39	37	3/31/2014	L8	0.61	0.01	0.01	48.85	29.82	53.82	---	0.06	0.55
39	37	4/16/2014	L8	0.24	0.01	0.01	44.77	31.51	81.66	---	0.12	1.00
39	37	5/2/2014	L8	0.18	0.01	0.01	44.90	34.63	102.69	---	0.12	1.09

Supplemental Table 4.6. (continued)

RMSE (Non-Agricultural Lands)												
Path	Row	Date	Satellite	T_s	Albedo	NDVI	Rn	G	H	ET_r	ET_rF	ET_a
39	37	6/19/2014	L8	0.14	0.01	0.01	36.25	34.84	108.02	---	0.18	1.78
39	37	7/21/2014	L8	0.07	0.01	0.01	32.73	37.41	128.62	---	0.13	1.45
39	37	8/6/2014	L8	0.10	0.01	0.01	43.53	36.48	63.54	---	0.12	1.17
39	37	8/22/2014	L8	0.71	0.01	0.01	38.18	53.69	100.37	---	0.12	0.87
39	37	9/23/2014	L8	0.19	0.01	0.01	48.29	31.98	51.55	---	0.12	0.86
39	37	10/9/2014	L8	0.71	0.01	0.02	41.66	39.28	45.44	---	0.19	0.78
39	37	11/10/2014	L8	0.79	0.01	0.03	51.14	24.56	44.88	---	0.21	0.90
40	30	3/19/2016	L7	0.33	0.01	0.02	23.06	50.60	48.30	---	0.34	0.85
40	30	4/20/2016	L7	0.40	0.01	0.02	17.59	47.40	24.41	---	0.15	0.89
40	30	5/30/2016	L8	0.58	0.00	0.02	14.57	58.33	40.98	---	0.13	0.98
40	30	6/7/2016	L7	0.72	0.01	0.02	16.53	51.40	42.33	---	0.12	1.13
40	30	6/23/2016	L7	0.48	0.01	0.02	13.98	30.40	58.46	---	0.13	1.42
40	30	7/1/2016	L8	0.33	0.01	0.02	18.90	36.76	114.90	---	0.28	2.48
40	30	7/9/2016	L7	0.46	0.01	0.01	16.24	36.66	74.01	---	0.14	1.43
40	30	7/25/2016	L7	0.51	0.01	0.01	17.29	40.44	42.51	---	0.10	0.89
40	30	8/2/2016	L8	0.34	0.01	0.01	19.11	42.02	36.59	---	0.08	0.69
40	30	8/10/2016	L7	0.28	0.01	0.01	20.48	54.61	36.55	---	0.10	0.55
40	30	8/18/2016	L8	0.75	0.01	0.02	28.61	78.90	89.59	---	0.15	1.14
40	30	9/11/2016	L7	0.35	0.01	0.01	21.59	30.14	94.22	---	0.10	0.94
40	30	9/19/2016	L8	0.44	0.01	0.01	20.72	39.40	20.69	---	0.07	0.32
40	30	9/27/2016	L7	0.34	0.01	0.02	25.49	60.99	48.16	---	0.10	0.60
40	30	10/21/2016	L8	0.90	0.01	0.02	25.07	40.68	14.06	---	0.16	0.33
45	31	4/30/2004	L5	0.43	0.00	0.09	29.08	27.42	34.79	---	0.19	0.78
45	31	6/1/2004	L5	0.42	0.00	0.08	23.03	20.82	57.92	---	0.19	1.31
45	31	8/4/2004	L5	0.44	0.00	0.09	31.92	27.85	45.08	---	0.16	0.88
45	31	8/20/2004	L5	0.40	0.01	0.09	37.13	23.71	32.79	---	0.11	0.79
45	31	9/21/2004	L5	0.40	0.00	0.12	54.24	29.63	43.46	---	0.18	0.53
45	31	10/7/2004	L5	0.41	0.01	0.16	58.53	23.13	43.06	---	0.23	0.66

APPENDIX B: SUPPLEMENTAL FIGURES

Supplemental Figures: Chapter 2

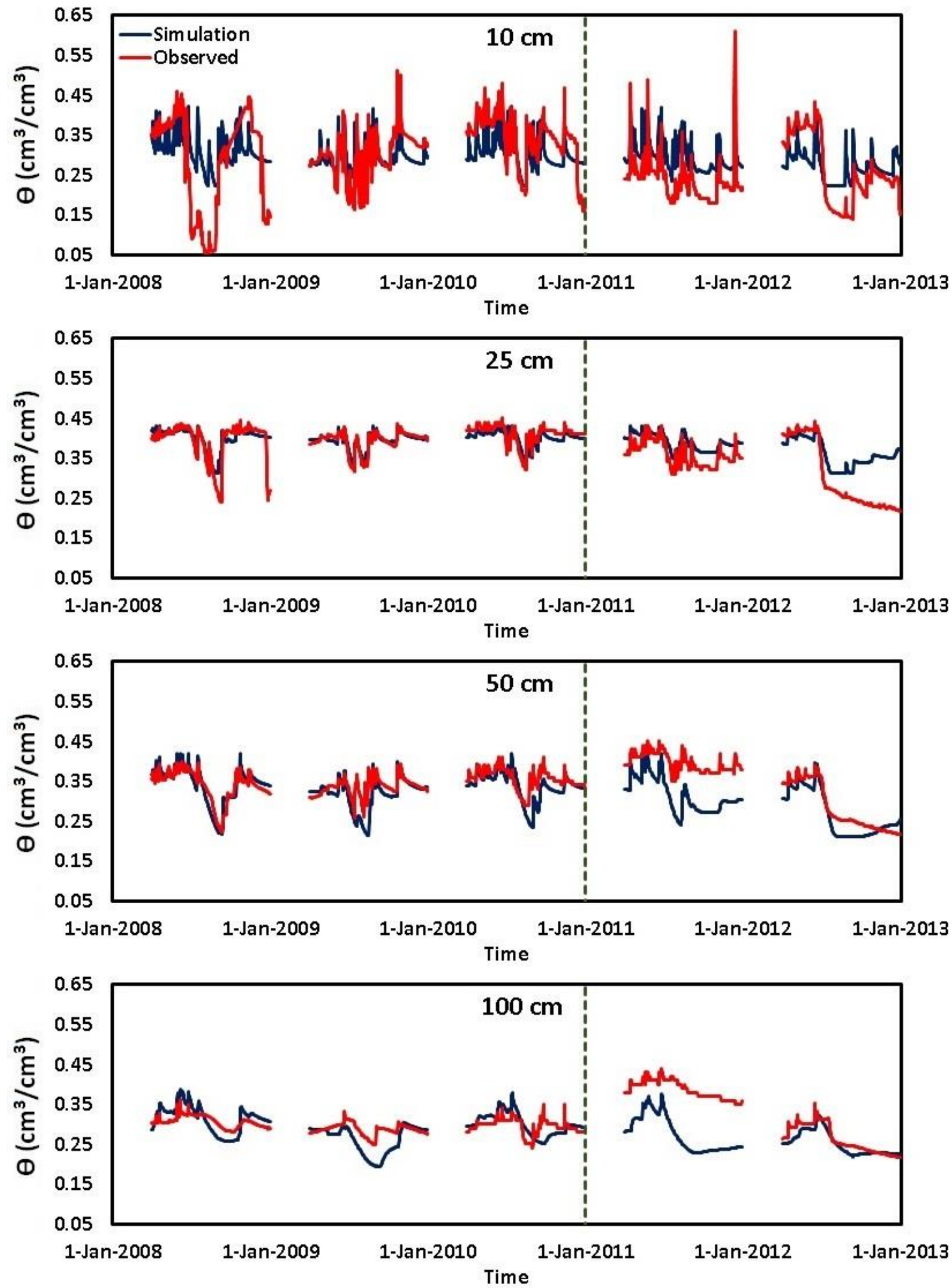

Supplemental Figure 2.1. Daily observed and simulated SWC (θ) during the calibration (2008–2010) and validation (2011–2012) periods at TP 2 location.

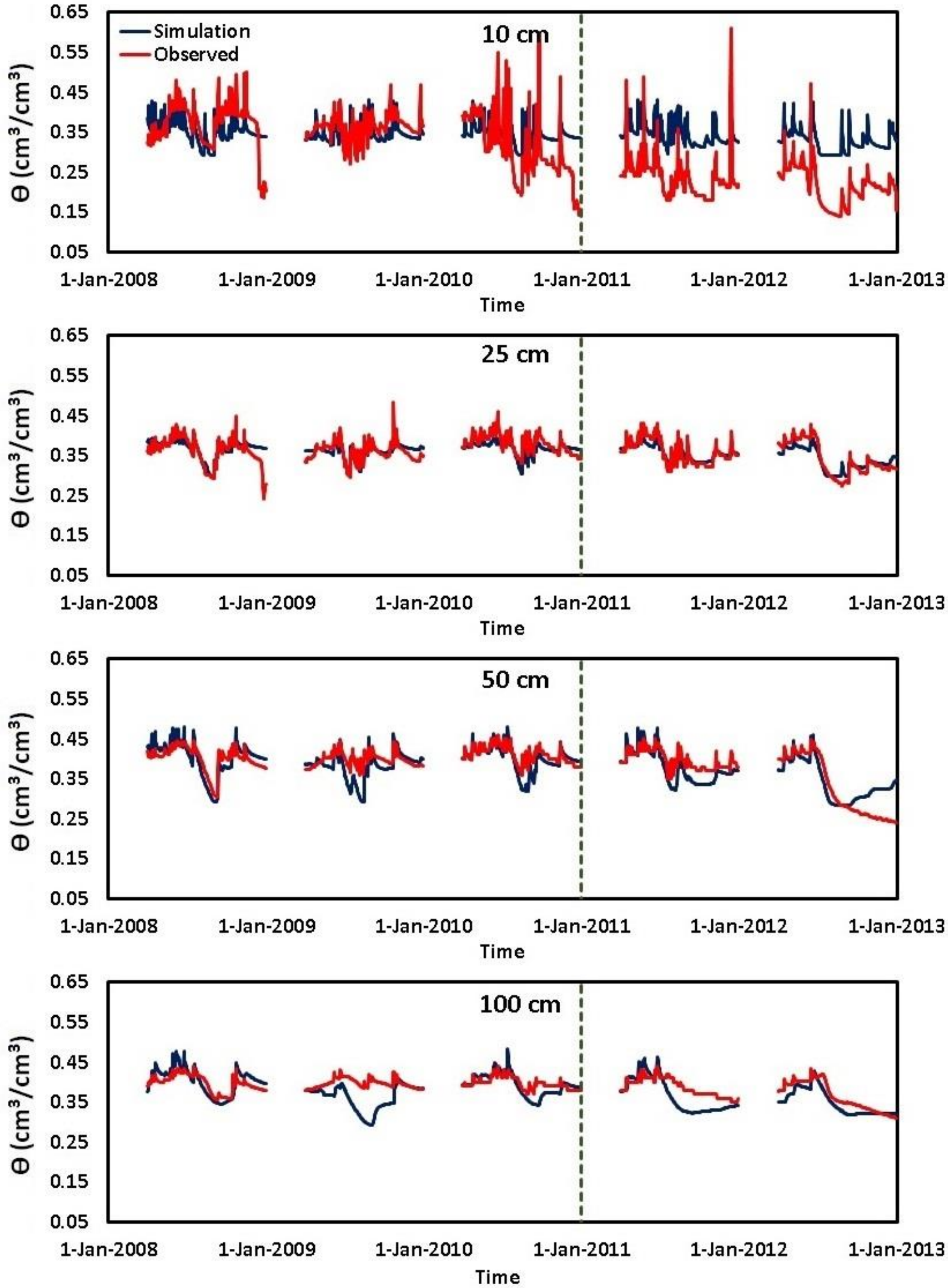

Supplemental Figure 2.2. Daily observed and simulated SWC (θ) during the calibration (2008–2010) and validation (2011–2012) periods at TP 3 location.

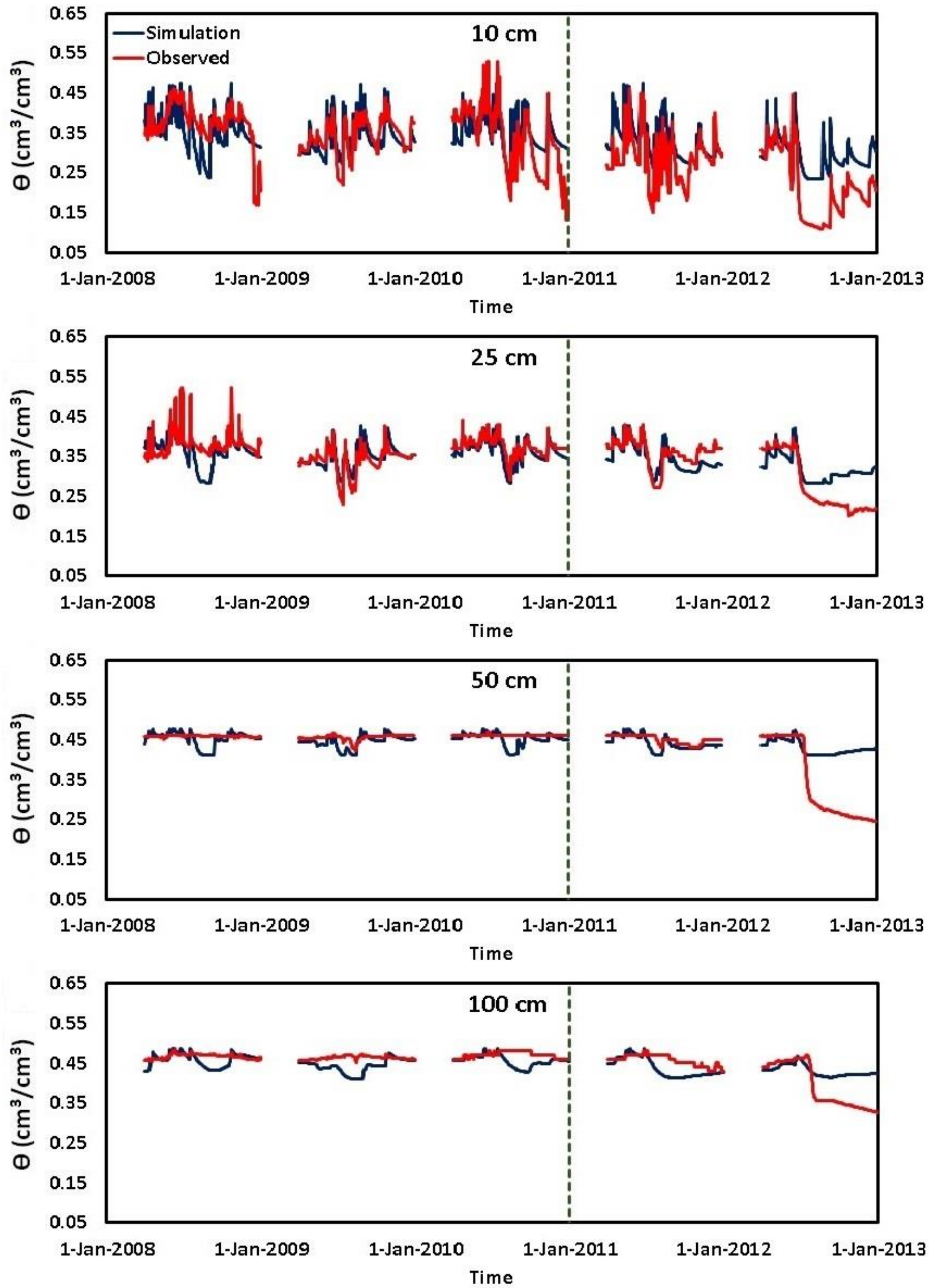

Supplemental Figure 2.3. Daily observed and simulated SWC (θ) during the calibration (2008–2010) and validation (2011–2012) periods at TP 4 location.

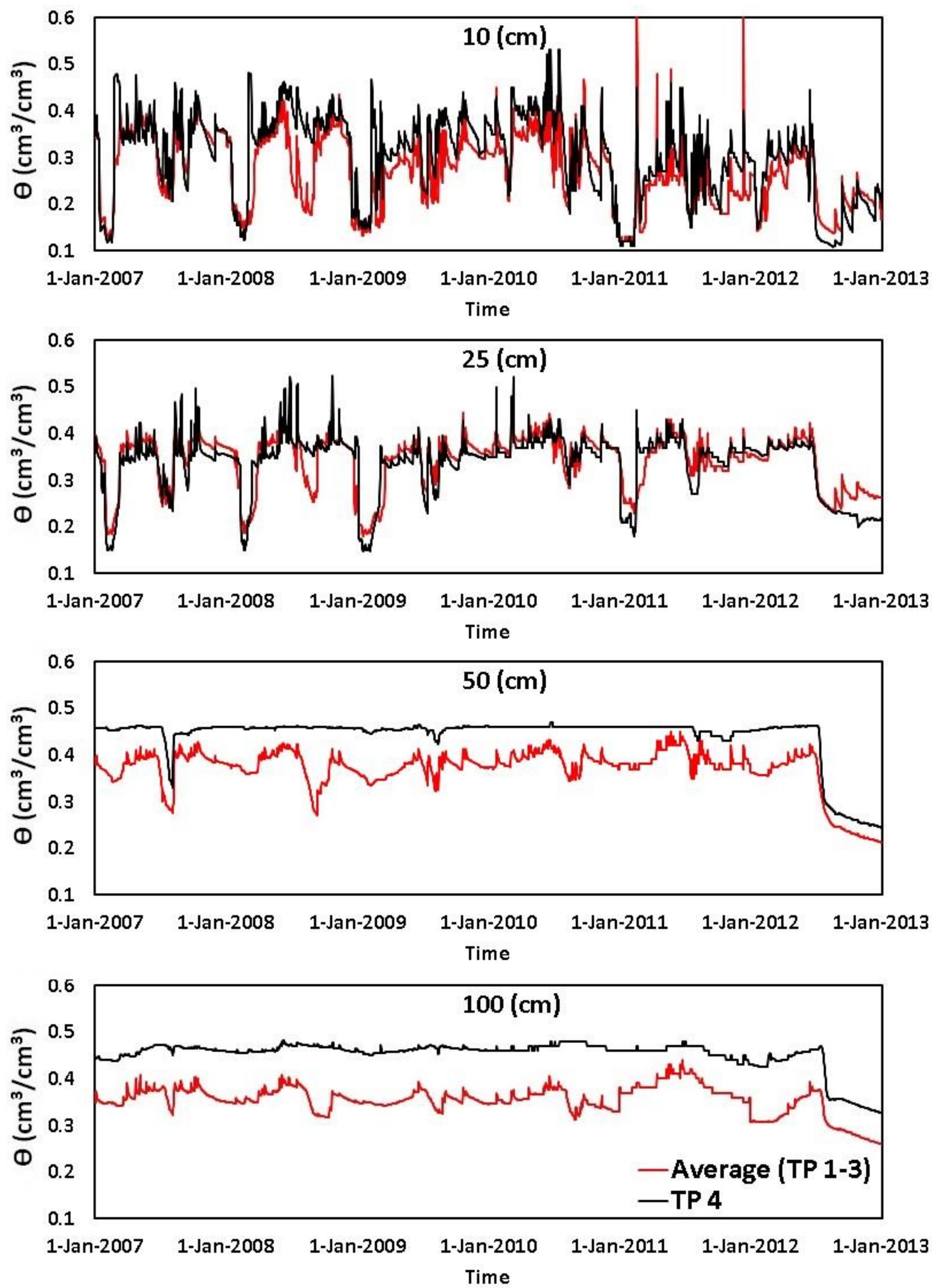

Supplemental Figure 2.4. Daily observed SWC (θ) at TP 4 location versus the average observed SWC (θ) at the other three locations (TP 1-3) during study period.

Supplemental Figures: Chapter 3

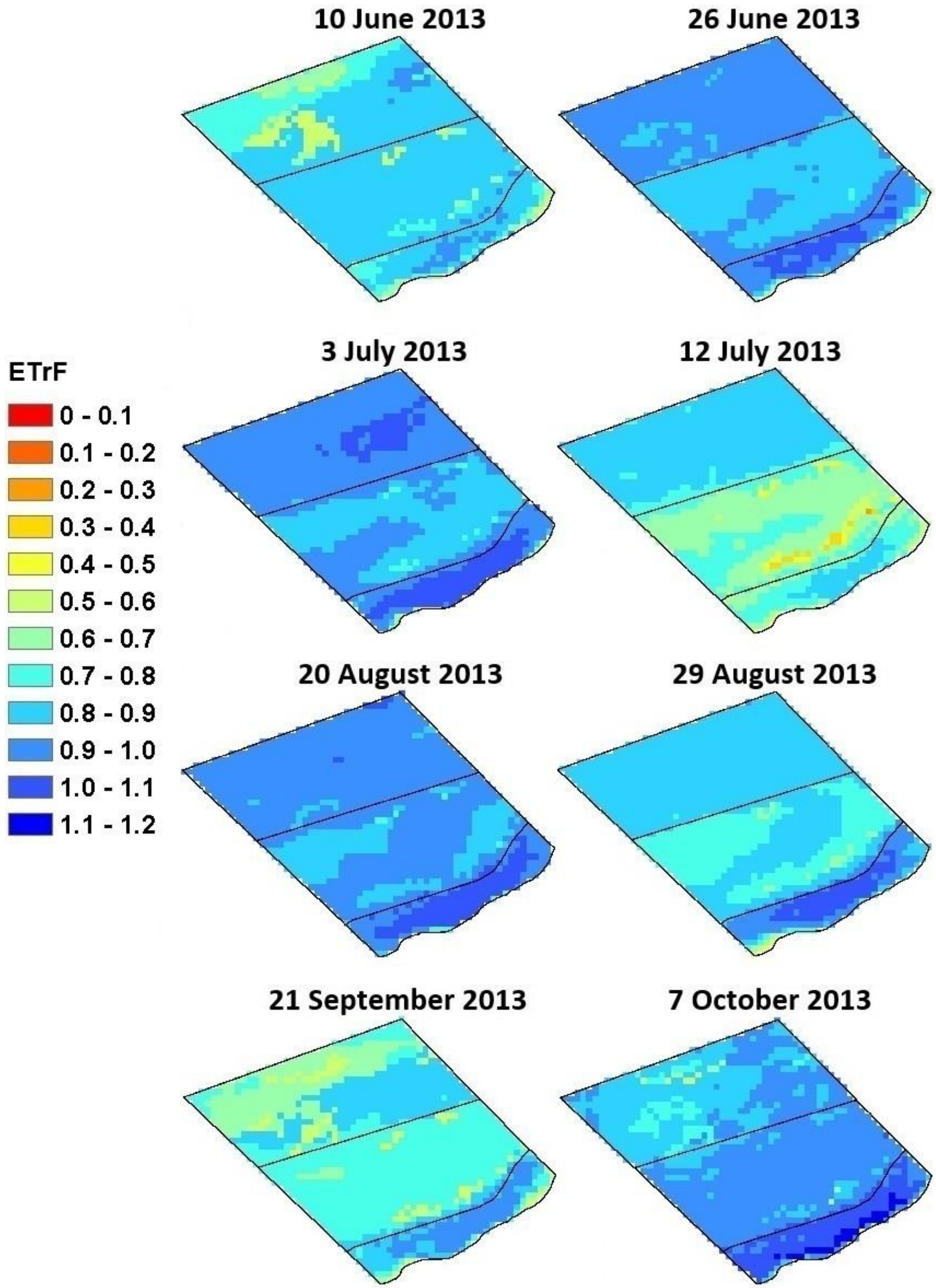

Supplemental Figure 3.1. ET_rF maps of study site (2013).

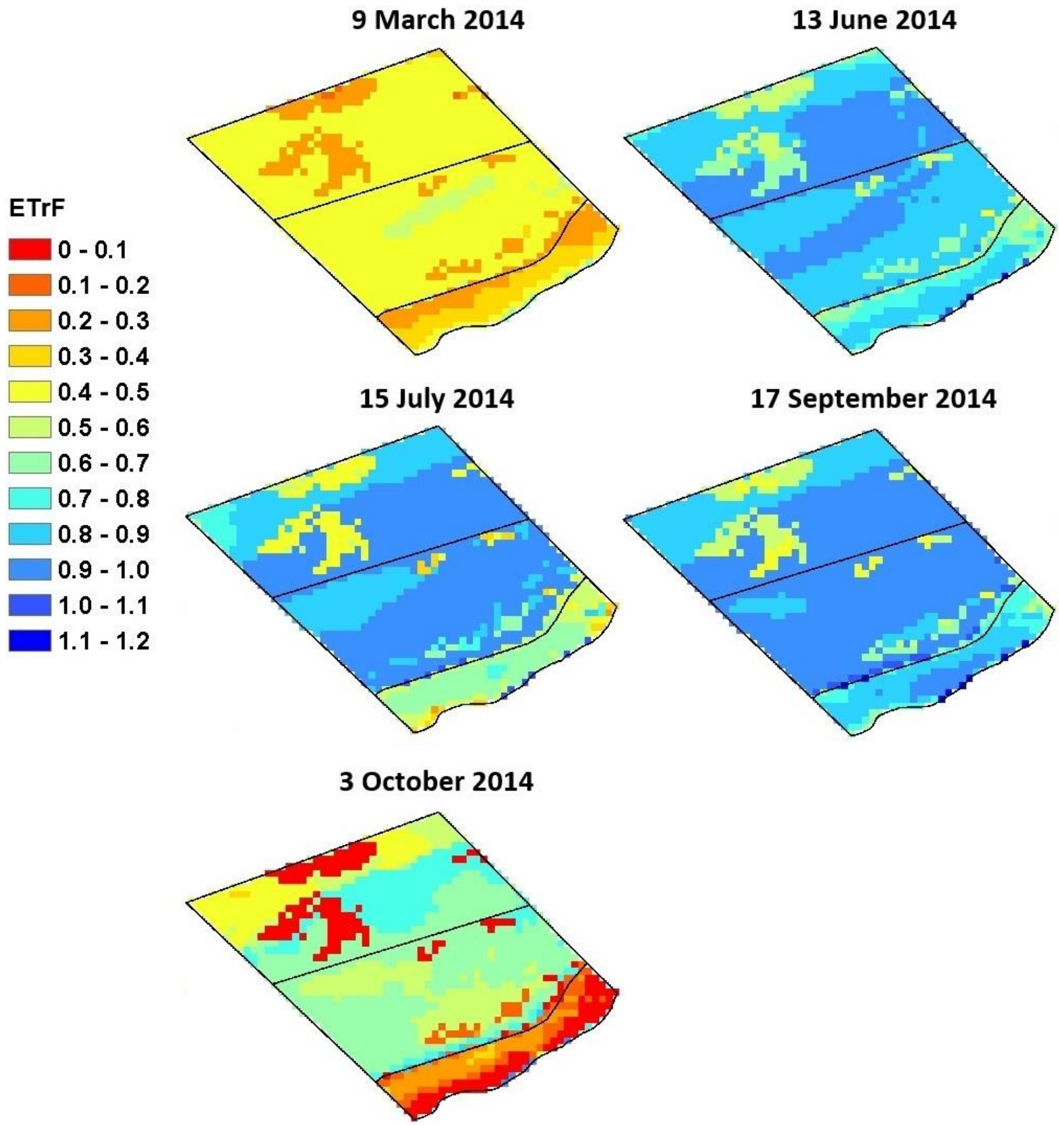

Supplemental Figure 3.2. ET_rF maps of study site (2014).

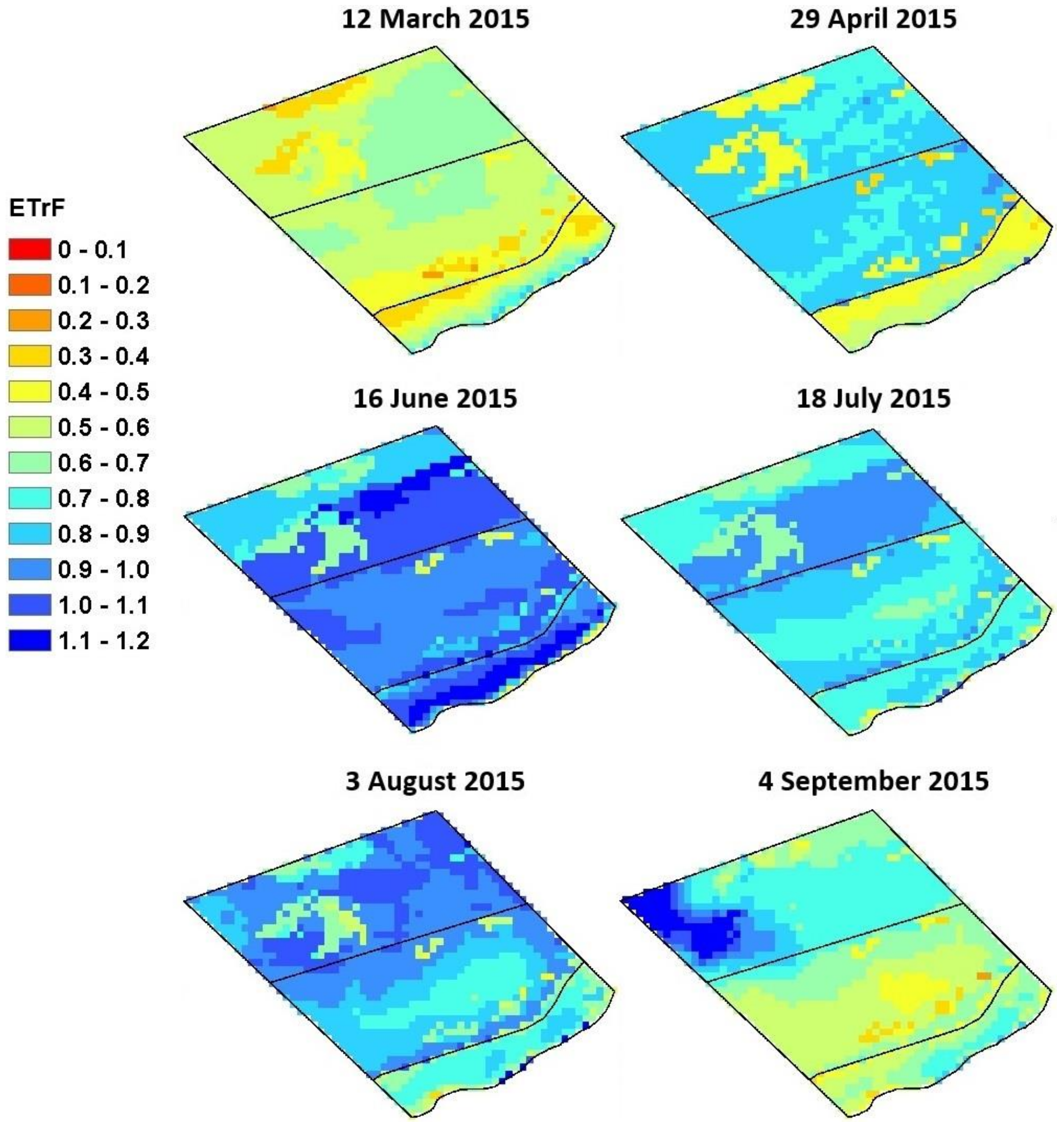

Supplemental Figure 3.3. ET_rF maps of study site (2015).

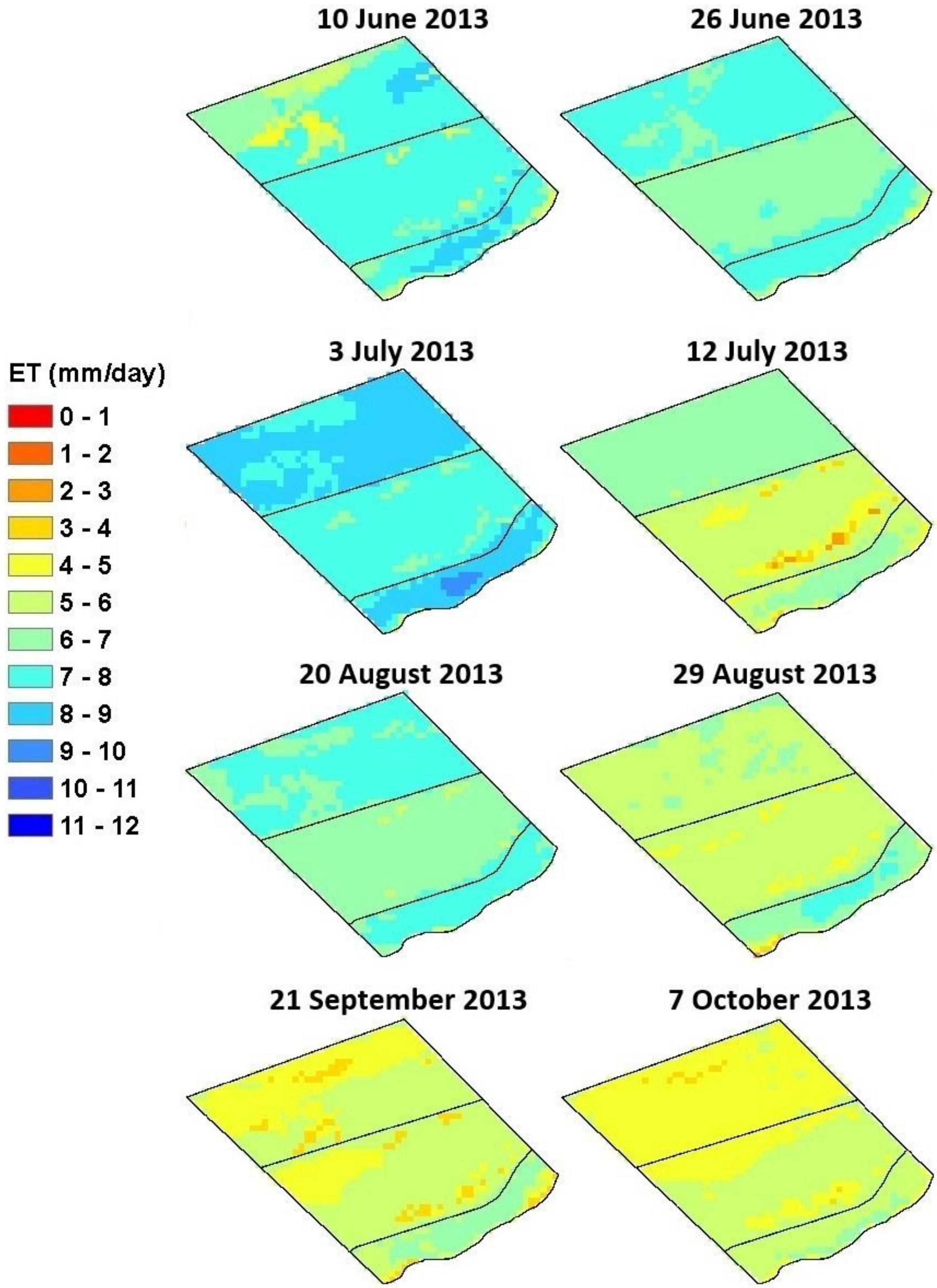

Supplemental Figure 3.4. ET_a maps of study site (2013).

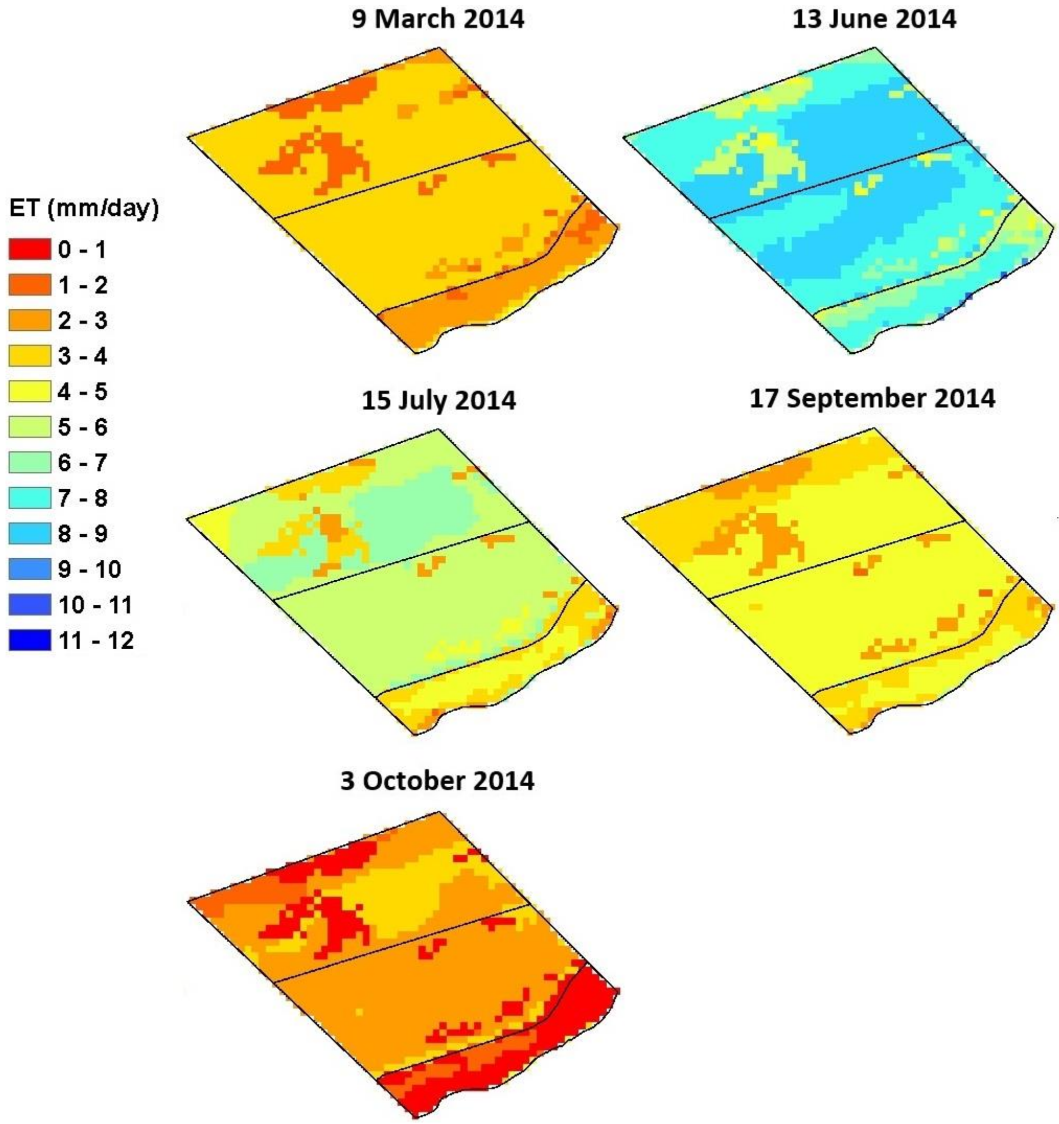

Supplemental Figure 3.5. ET_a maps of study site (2014).

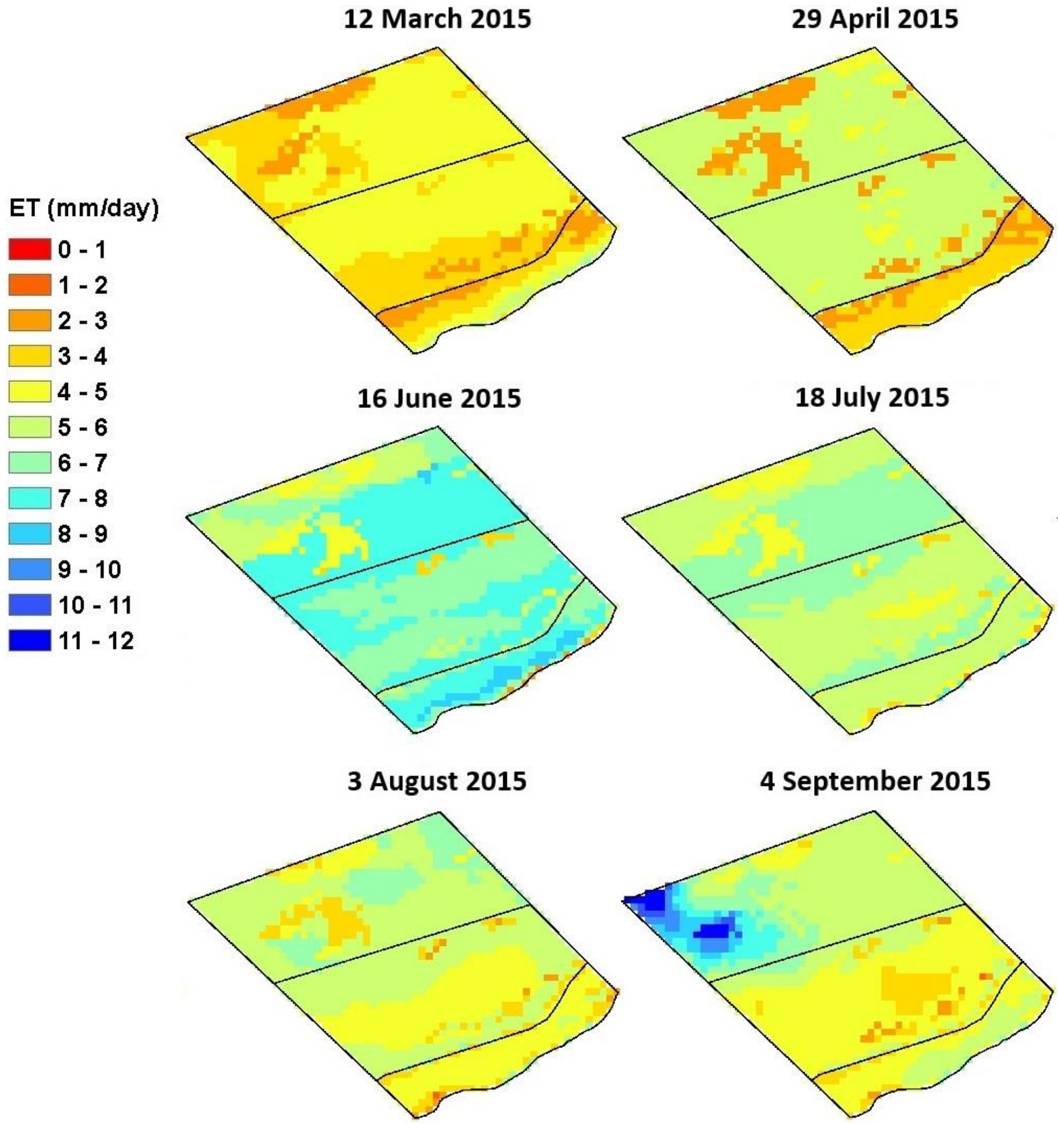

Supplemental Figure 3.6. ET_a maps of study site (2015).

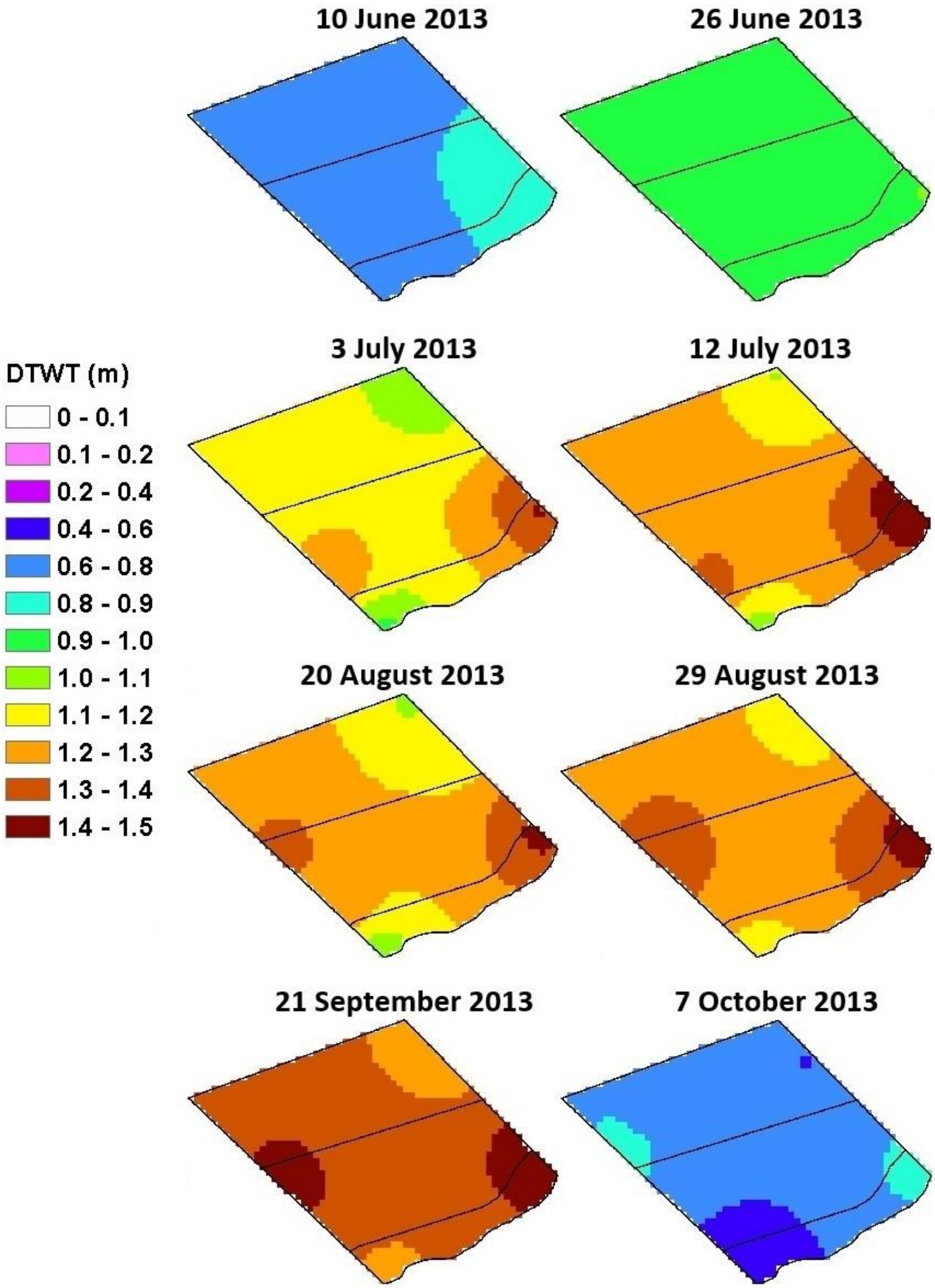

Supplemental Figure 3.7. DTWT maps of study site on (2013).

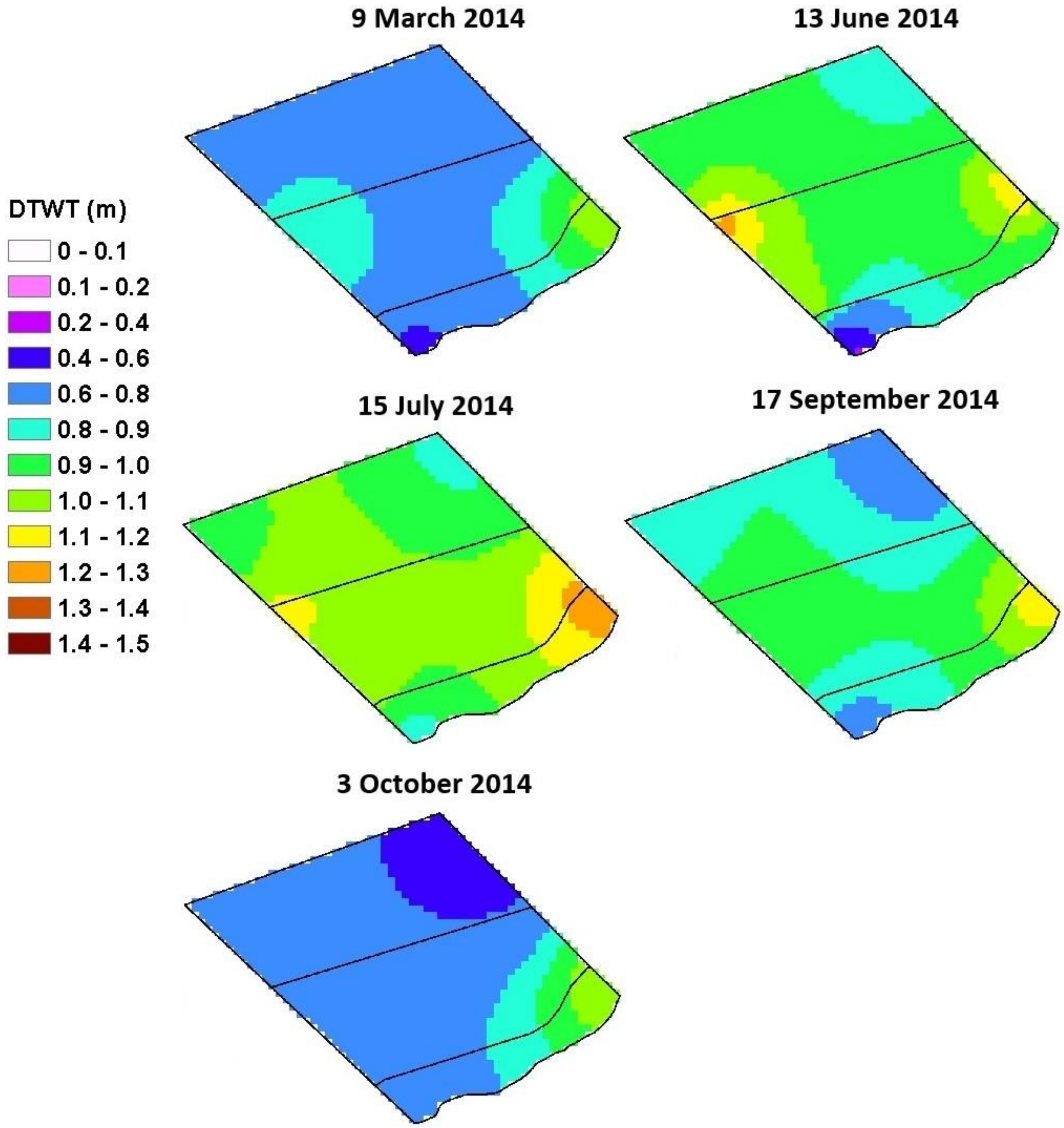

Supplemental Figure 3.8. DTWT maps of study site on (2014).

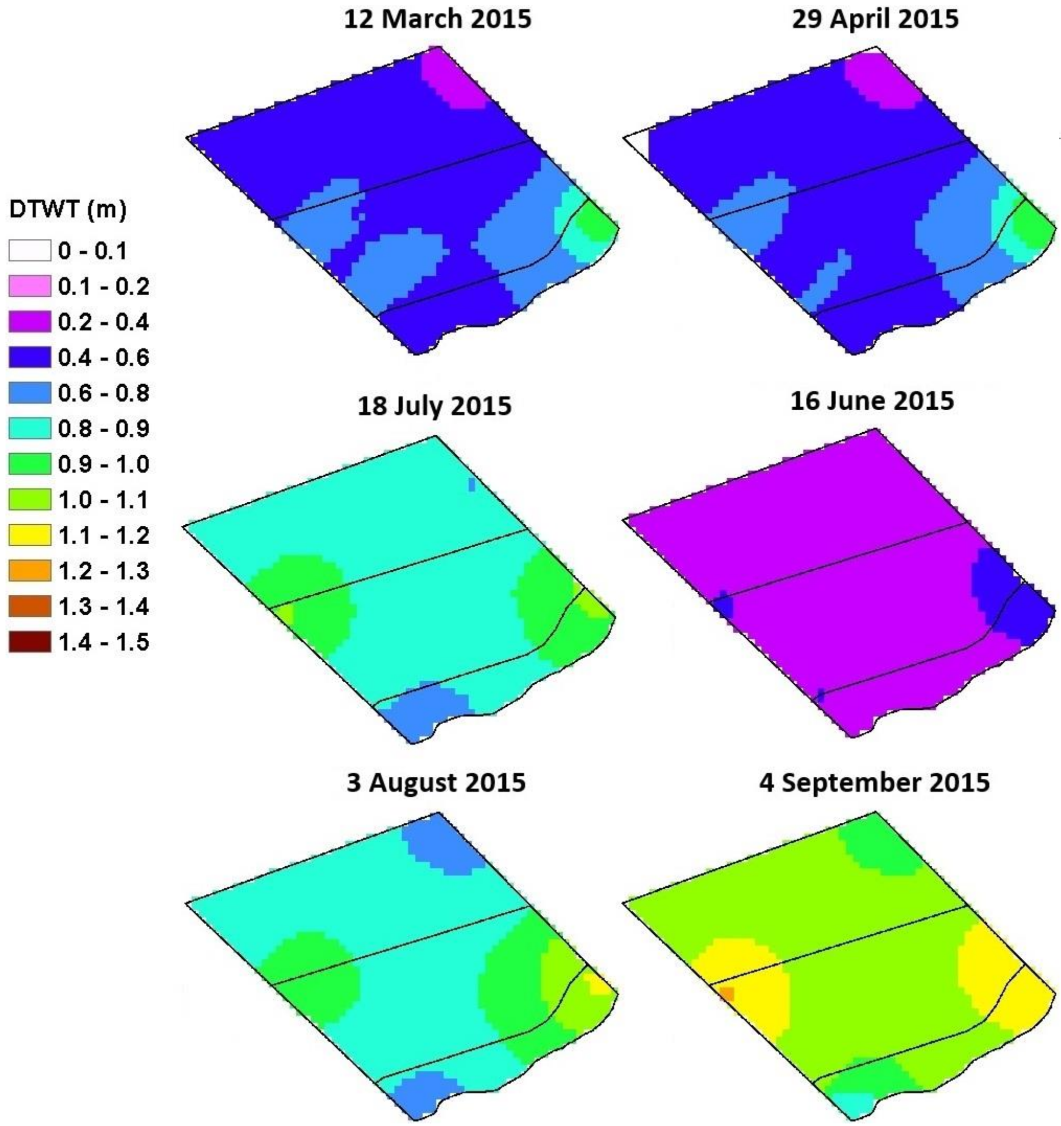

Supplemental Figure 3.9. DTWT maps of study site on (2015).

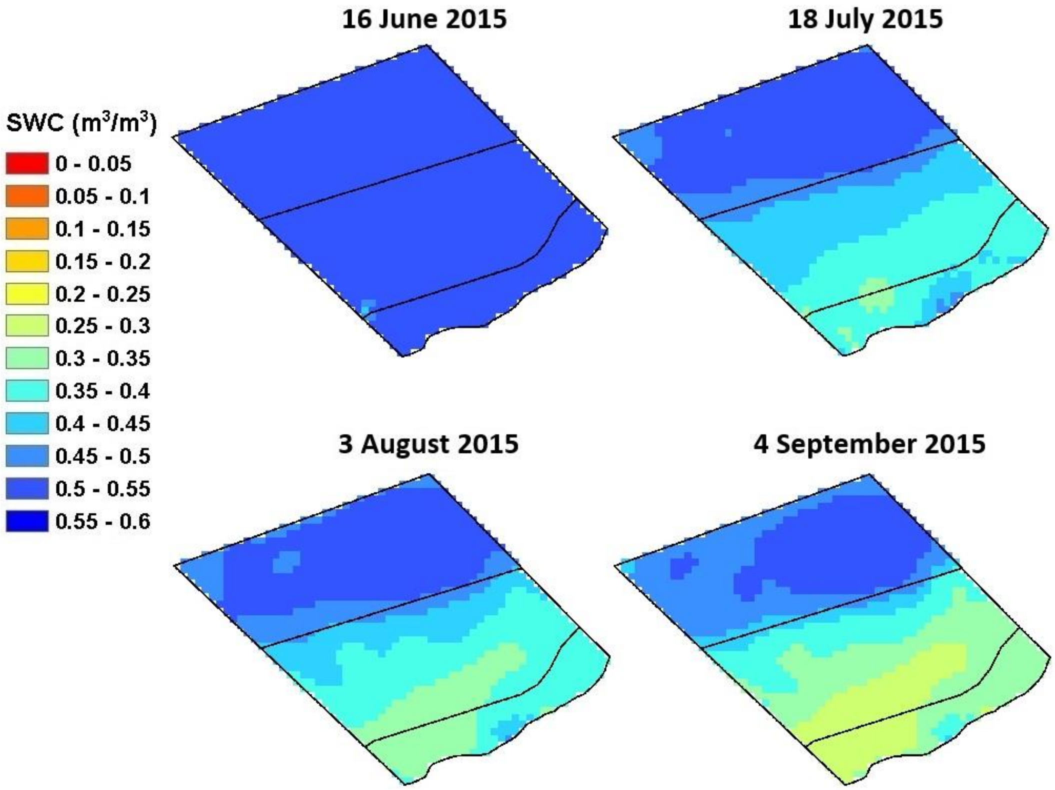

Supplemental Figure 3.10. SWC maps of study site (2015).

Supplemental Figures: Chapter 4

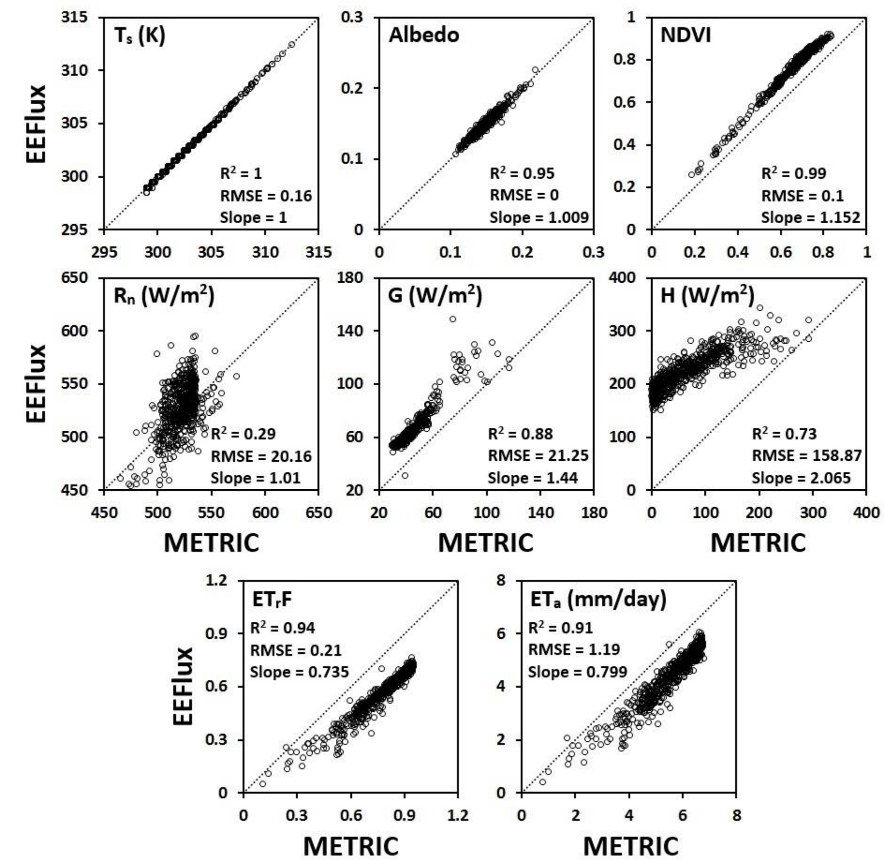

Supplemental Figure 4.1. Comparison between different components from EEFlux and METRIC models for Path 29 Row 31, Landsat 5, 2002/08/15.

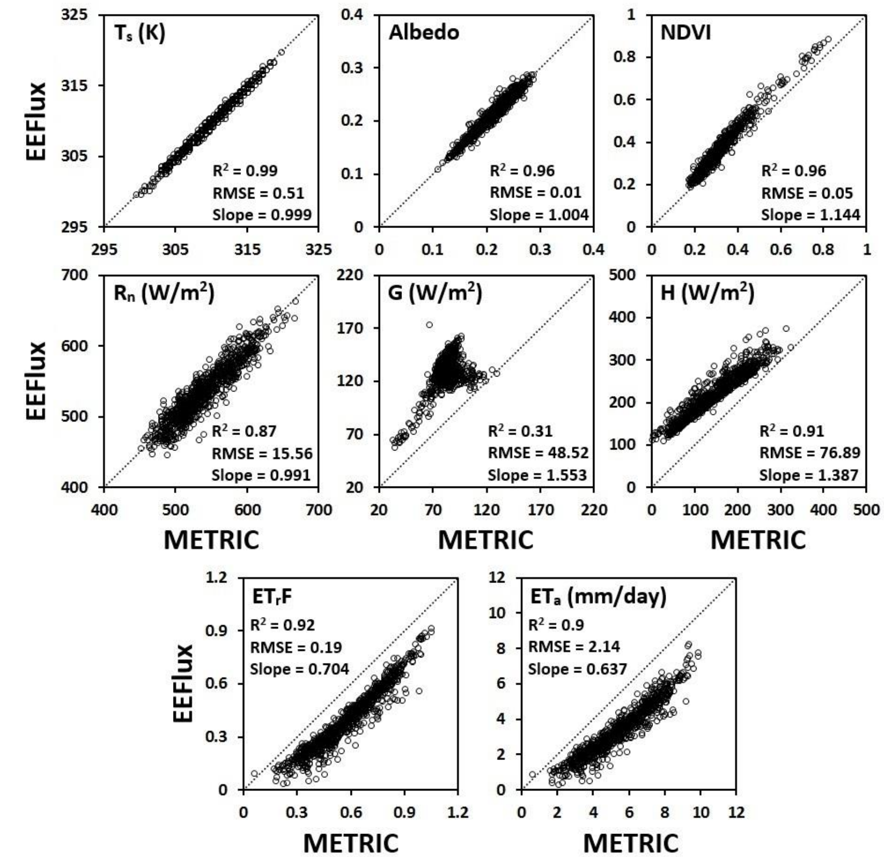

Supplemental Figure 4.2. Comparison between different components from EEFlux and METRIC models for Path 30 Row 31, Landsat 7, 2002/06/11.

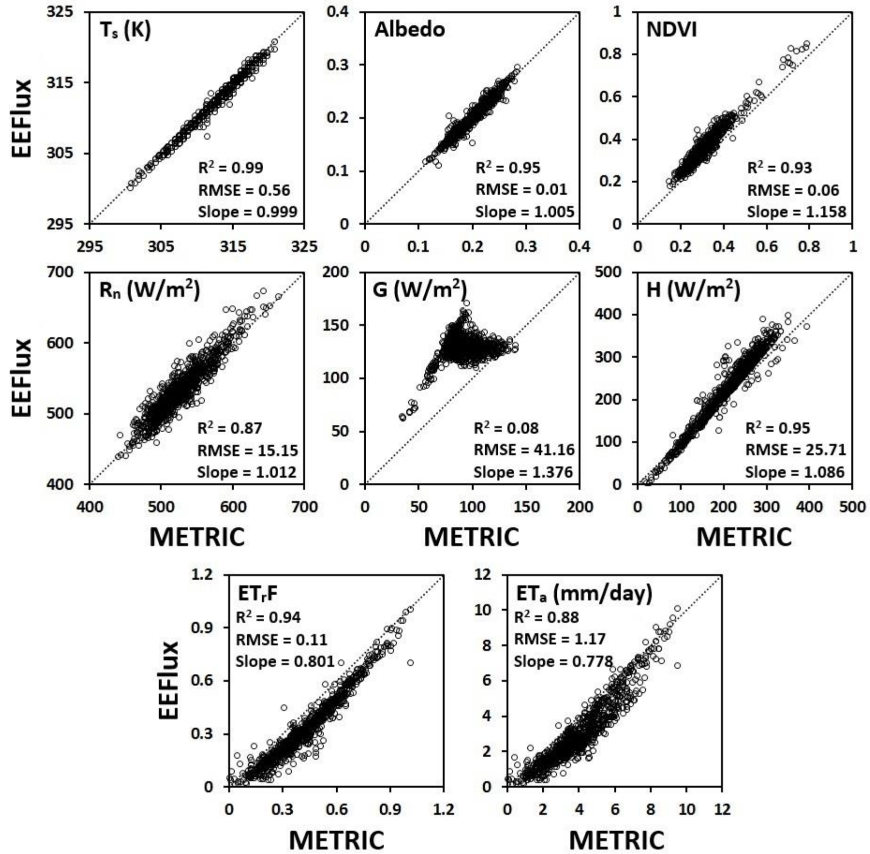

Supplemental Figure 4.3. Comparison between different components from EEFlux and METRIC models for Path 30 Row 32, Landsat 7, 2002/06/11.

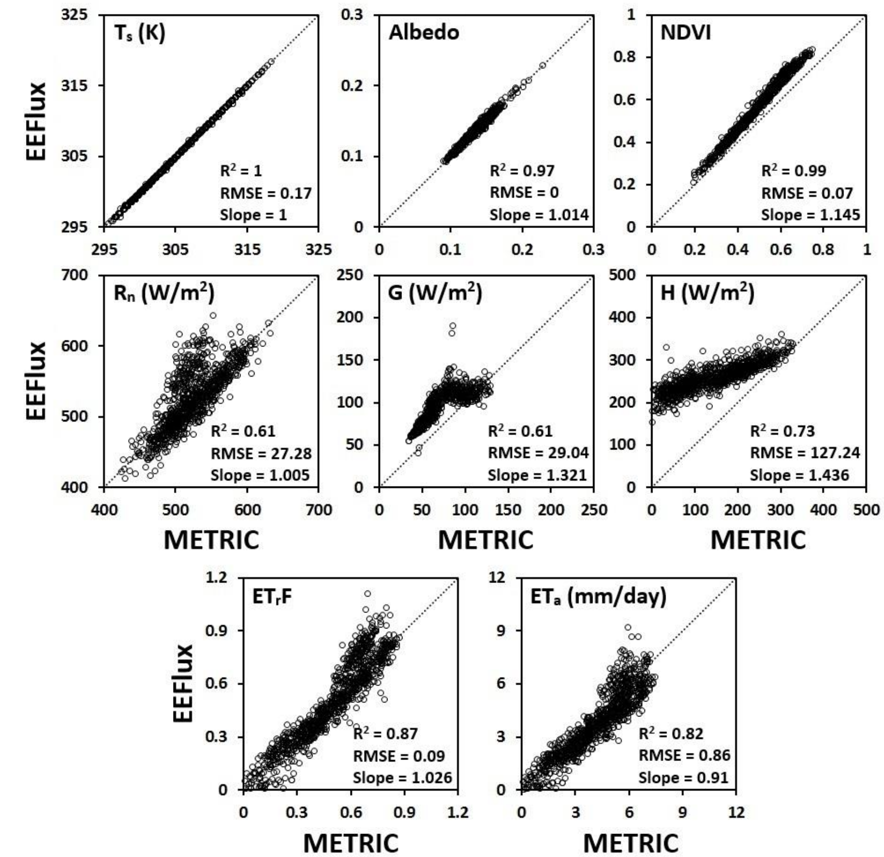

Supplemental Figure 4.4. Comparison between different components from EEFlux and METRIC models for Path 37 Row 30, Landsat 5, 2011/09/01.

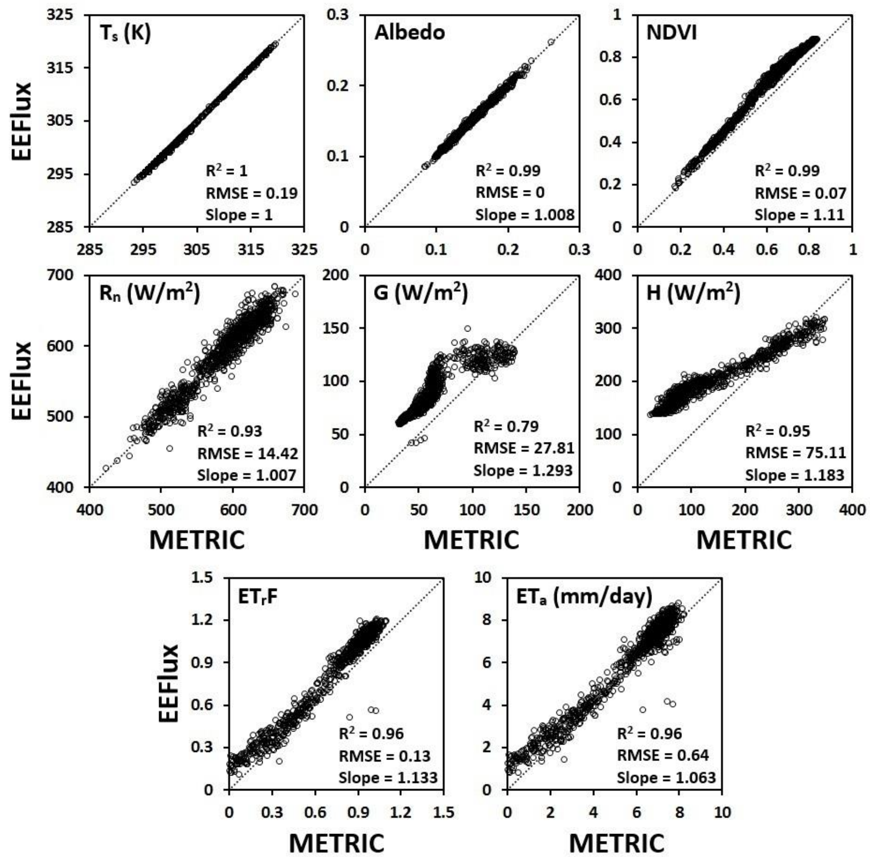

Supplemental Figure 4.5. Comparison between different components from EEFlux and METRIC models for Path 37 Row 31, Landsat 5, 2011/08/16.

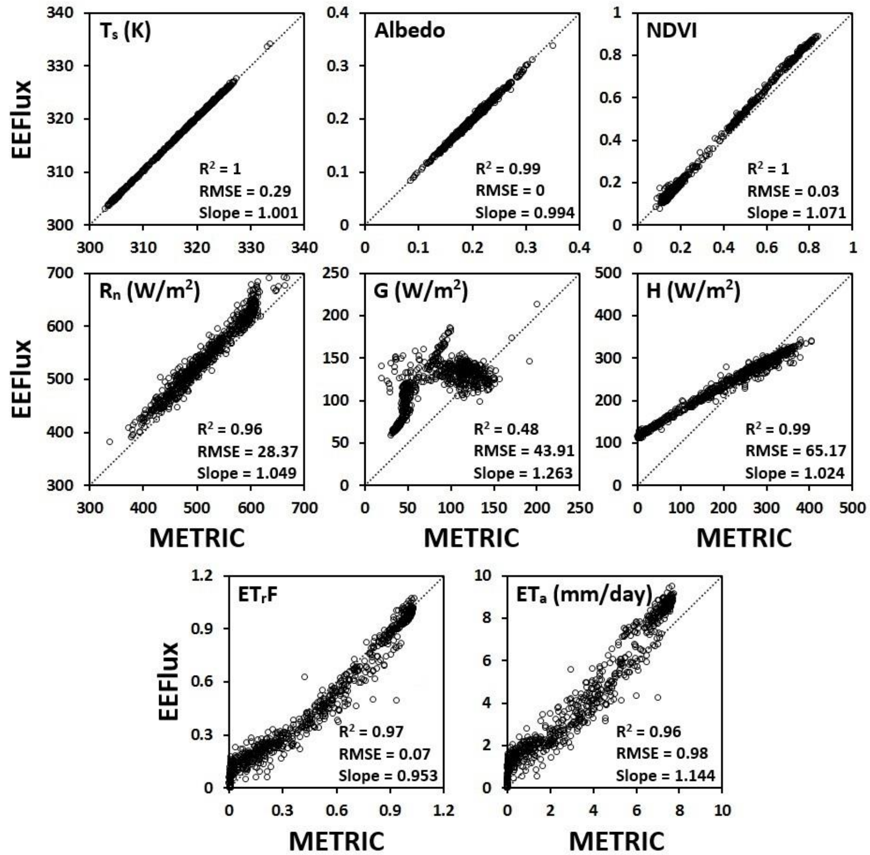

Supplemental Figure 4.6. Comparison between different components from EEFlux and METRIC models for Path 39 Row 37, Landsat 8, 2014/04/16.

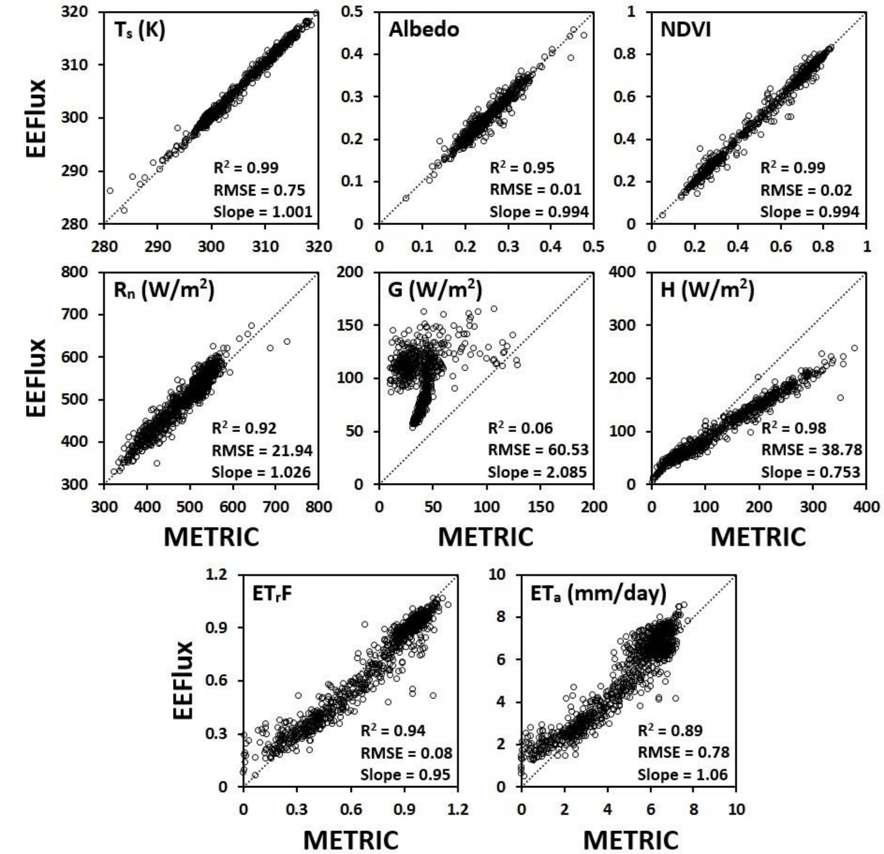

Supplemental Figure 4.7. Comparison between different components from EEFlux and METRIC models for Path 40 Row 30, Landsat 8, 2016/08/18.

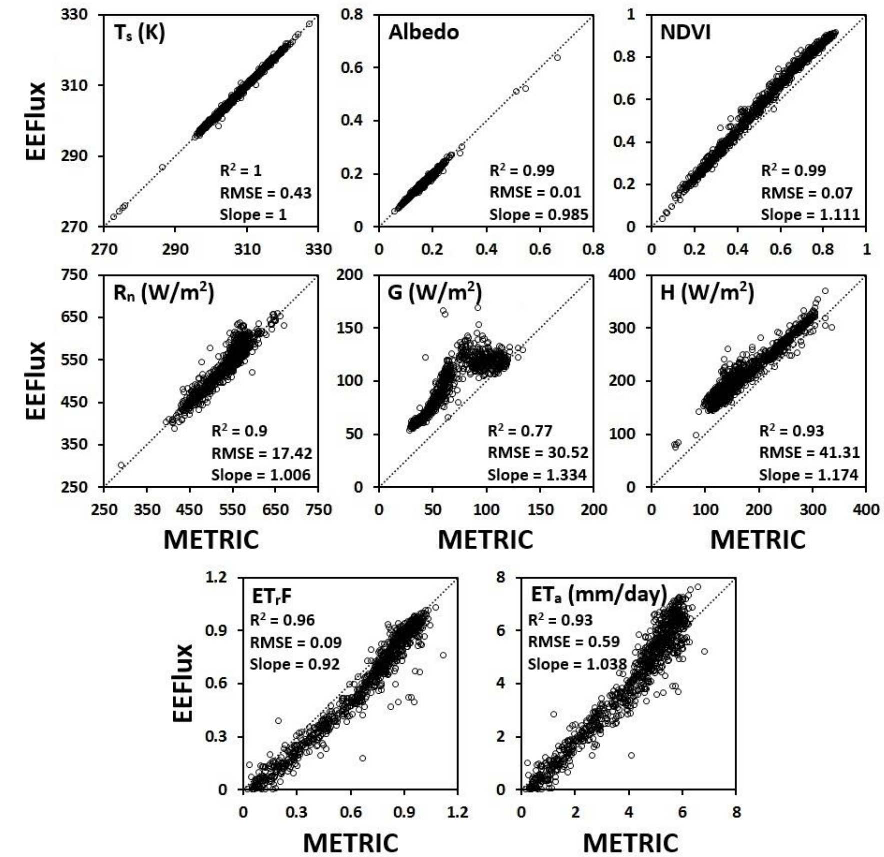

Supplemental Figure 4.8. Comparison between different components from EEFlux and METRIC models for Path 45 Row 31, Landsat 5, 2004/08/04.

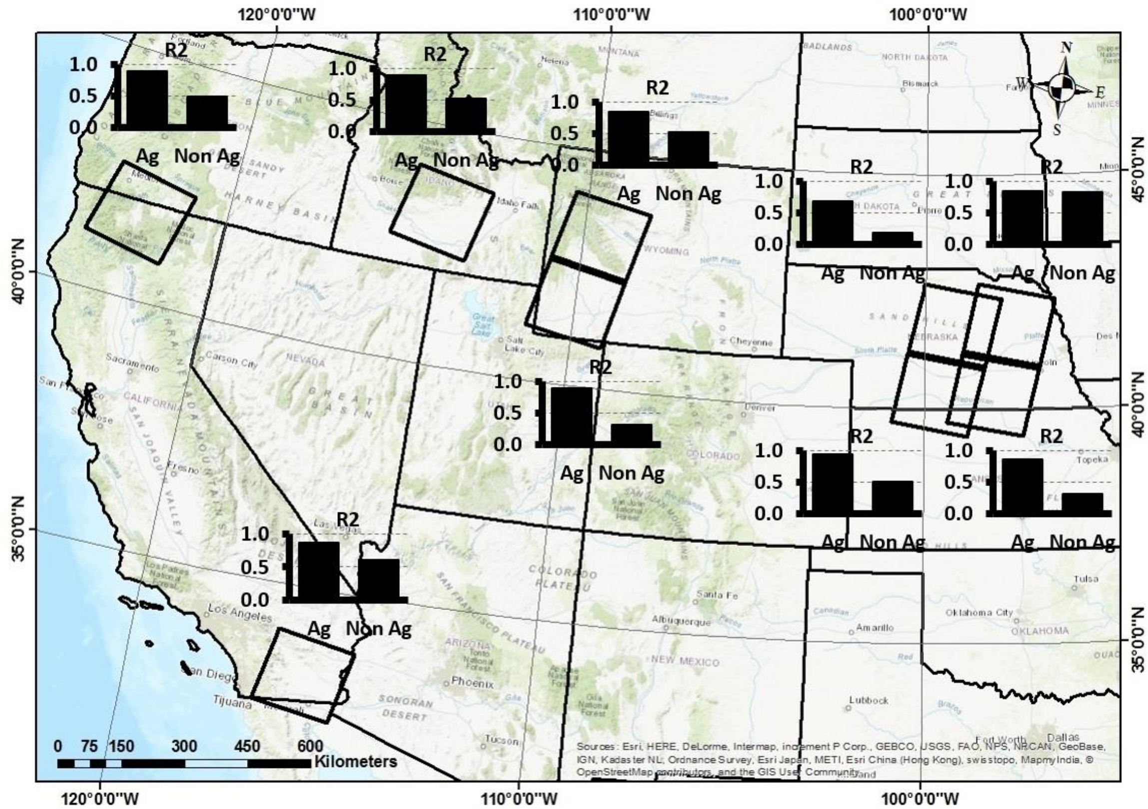

Supplemental Figure 4.9. Average R^2 values for ET_rF from EEFlux vs. METRIC for five locations across the western USA for agricultural and nonagricultural areas.

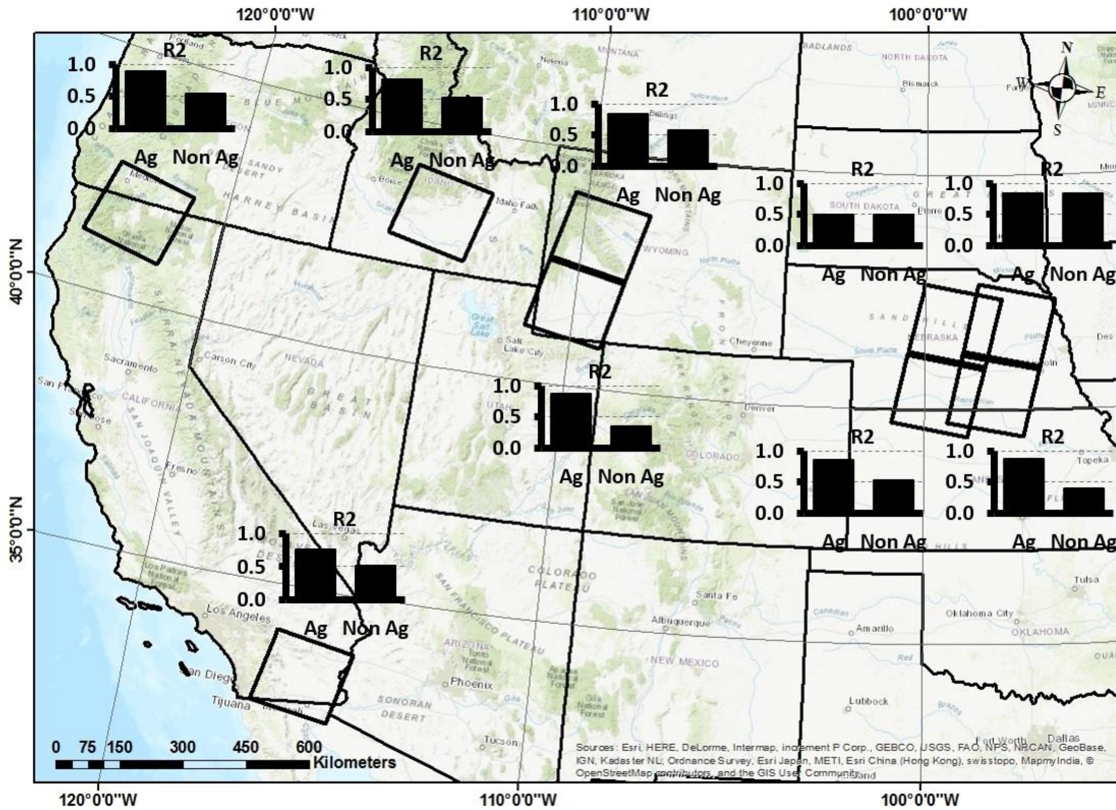

Supplemental Figure 4.10. Average R2 values for ET_rF from EEFlux vs. METRIC for five locations across the western USA for agricultural and nonagricultural areas.